Flux Reconstruction as a Direct Method for Near-Field Computational Aeroacoustics

Patrick C. Mills

A Thesis

In the Department

of

Mechanical, Industrial, and Aerospace Engineering

Presented in Partial Fulfillment of the Requirements

For the Degree of

Master of Applied Sciences (Mechanical Engineering) at

Concordia University

Montreal, Quebec, Canada

March 2021

CONCORDIA UNIVERSITY

School of Graduate Studies

This is to certify that thesis prepared

By: **Patrick C. Mills**

Entitled: **Flux Reconstruction as a Direct Method for Near-Field Computational Aeroacoustics**

and submitted in partial fulfillment of the requirements for the degree of

Master of Applied Science (Mechanical Engineering)

complies with the regulations of the University and meets the accepted standards with respect to originality and quality.

Signed by the final Examining Committee:

_____ Chair

Dr. Hany Gomaa

_____ Internal Examiner

Dr. Hany Gomaa

_____ External Examiner

Dr. Joonhee Lee

_____ Supervisor

Dr. Brian Vermeire

Approved by: _____

Chair of Department or Graduate Program Director, Dr. Martin Pugh

_____ 2021 _____

Dean of Faculty, Dr. Mourad Debbabi

Abstract

Flux Reconstruction as a Direct Method for Near-Field Computational Aeroacoustics

Patrick C. Mills

The noise produced from commercial aviation is detrimental and strictly regulated at an international level. To satisfy stringent forthcoming noise reduction requirements, current industry standard, lower order aeroacoustic methods used to approximate acoustic fields must be replaced with high-order methods that can more accurately compute the acoustic field, providing invaluable insight into noise generation and potential design optimization processes. In this thesis, the accuracy and performance of high order numerical methods, as applied in the scope of computational aeroacoustics, are evaluated. Specifically, the high order flux reconstruction method's ability to directly compute acoustic fields is assessed. The field of computational aeroacoustics is intrinsically dissimilar to the field of computational fluid dynamics and thus contains highly distinctive numerical challenges. Several verification studies are performed, for a range of polynomial orders, each addressing an individual numerical challenge. It is shown that the high order flux reconstruction method sufficiently resolves each of these numerical challenges, with higher order polynomials providing more accurate and efficient results on a per degree of freedom basis. The high order flux reconstruction method's proficiency for direct computation of near-field acoustics is validated by performing simulations of flow over a cylinder and a deep cavity and comparing the results against experimental data. Finally, the performance of the high order flux reconstruction method in industrial applications is assessed by directly computing the acoustic field produced by a NACA0012 airfoil at varying angles of attack.

Acknowledgments

First and foremost, I would like to express my sincerest gratitude to my parents, Suzanne and Neil, for their unconditional love and support throughout my academic career.

Secondly, I would like to thank my siblings, Emily, Bradley, and Cameron, for their continued encouragement during my time at Concordia.

I also wish to thank the friends I made during my time in Montreal, Evan, Tristan, Dillon, and Kevin, for the wonderful memories and countless morning tasties.

I would also like to thank my lab mates, particularly Carlos and Mohsen, for their willingness to offer assistance and advice throughout my time in the lab.

Lastly, I would like to extend a special thank you to Dr. Brian Vermeire, whose knowledge, guidance, and support invaluably aided me throughout my research.

Contents

List of Figures

List of Tables

Nomenclature

English Letters

a	Runge-Kutta Matrix
A	Amplitude
A_c	Characteristic Area
b	Weighted Runge-Kutta Coefficient
b_s*	Implicit Runge-Kutta Error Coefficient
c	Vector of Runge-Kutta Time Stages
c_h	Chord Length
c_p	Specific Heat, Constant Pressure
c_v	Specific Heat, Constant Volume
c_0	Speed of Sound
C_D	Coefficient of Drag
C_L	Coefficient of Lift
C_P	Coefficient of Pressure
d	Diameter
dB	Decibel
D	Dimension
$\bar{D}$	Distance
D_F	Drag Force
e_k, e_t	Specific Kinetic, Thermal Energy
e_0	Vector of Ones
e, E	Specific, Total Internal Energy
E_w	Energy Contained at a Wave-number
$\bar{f}$	Element Face
$\vec{f}$	Flux
f_i	Flux in i^{th} Direction
F	Force
F_b	Body Force

$\hat{F}^n$	Normal Interface Flux Jump
$\mathcal{F}$	Flux Polynomial
$\mathcal{F}_c$	Continuous Flux Polynomial
$\mathcal{F}_e$	Element-wise Flux Polynomial
$\mathcal{F}^R$	Flux Polynomial, Reference Space
g	Correction Function
h	Specific Enthalpy
h_e	Width of Computational Element
I	Identity Matrix
k_w	Wave-number
K	Number of Solution Points
l_t, L_t	Minimum, Maximum Turbulent Length Scales
L	Domain Length
L_c	Characteristic Length
L_F	Lift Force
m	Mass
M_a	Mach Number
$\hat{n}$	Outward Surface Normal
N_{DIM}	Number of Dimensions
N_{DOF}	Number of Degrees of Freedom
N_E	Number of Elements
O	Order of Accuracy
p	Pressure
P_r	Prandtl Number
$P(z)$	Stability Polynomial
$\mathcal{P}$	Polynomial Order
$\vec{q}$	Specific Heat Flux Vector
q, Q	Specific, Total Heat
r	Specific Gas Constant
R	Radius
R_e	Reynolds Number
$\mathcal{R}$	Weighted Residual

s	Number of Runge-Kutta Stages
$\vec{s}$	Filtered Acoustic Source Vector
S	Domain Boundary
S_t	Strouhal Number
$\mathcal{S}$	Entropy
t	Time
t_c	Convective Time
T	Temperature
$\mathcal{T}$	Filtering Matrix
T_{ij}	Lighthill Stress Tensor
$\mathcal{T}$	Filtering Matrix
u	Conserved Variable
U	Numerical Solution
$\mathcal{U}$	Solution Polynomial
$\mathcal{U}_e$	Element-wise Solution Polynomial
V	Velocity Magnitude
$\vec{V}$	Velocity Vector
$\vec{V}_B$	Boundary Velocity
$\vec{V}_c$	Convective Velocity
V_i	Velocity in i^{th} Direction
$\vec{V}_t$	Velocity of Smallest Turbulent Length Scales
w, W	Specific, Total Work
W_d	Width
$\mathcal{W}$	Characteristic Waves
$\vec{x}$	Cartesian Coordinates
$\mathbf{x}$	Cartesian Coordinates, Source Location
$\mathbf{y}$	Cartesian Coordinates, Observer Location
Z	Location in Complex Plane

Greek Letters

α	Angle of Attack
α_a	Advection Velocity

β	Lifting Coefficient
γ	Specific Weight
δ_{ij}	Kronecker Delta
δ^*	Boundary Layer Displacement Thickness
Δt	Time Step
Δx	Grid Spacing
Δx_s	Smallest Grid Spacing for Turbulent Flows
ϵ	Slope Factor
θ_p	Propagation Angle
κ	Thermal Conductivity
λ	Wave Length
μ	Dynamic Viscosity
ν	Kinematic Viscosity
ν_a	Artificial Viscosity
ρ	Density
σ	Normal Stress
$\bar{\bar{\sigma}}$	Cauchy Stress Tensor
τ	Viscous Shear Stress
ϕ	Nodal Basis Function
ψ	Correction Field
Ψ	Correction Field for Elements with Triangular Faces
ω	Frequency
Ω	Domain
Ω_e	Computational Element

Acronyms

APE	Acoustic Perturbation Equations
BC	Boundary Condition
CAA	Computational Aeroacoustics
CFL	Courant-Friedrichs-Lewey Number
CFE	Continuous Finite Element
CFD	Computational Fluid Dynamics

CPU	Central Processing Unit
CS	Control Surface
DES	Detached Eddy Simulation
DFE	Discontinuous Finite Element
DG	Discontinuous Galerkin
DNS	Direct Numerical Simulation
DOF	Degrees of Freedom
FAA	Federal Aviation Administration
FD	Finite Difference
FE	Finite Element
FLOP/s	Floating Point OPerations per Second
FR	Flux Reconstruction
FV	Finite Volume
FWH	Ffowcs-Williams and Hawkings
IATA	International Air Transport Association
ICAO	International Civil Aviation Organization
ILES	Implicit Large Eddy Simulation
LCP	Lifting Collocation Penalty
LEE	Linearized Euler Equations
LES	Large Eddy Simulation
NACA	National Advisory Committee for Aeronautics
NASA	National Aeronautics and Space Administration
NRBC	Non-Reflecting Boundary Condition
NS	Navier-Stokes
PDE	Partial Differential Equation
P-ERK	Paired Explicit Runge-Kutta
PSD	Power Spectral Density
RANS	Reynolds Averaged Navier-Stokes
RK	Runge-Kutta
RMS	Root Mean Squared
SD	Spectral Difference
SG	Staggered Grid

SGS	Sub Grid Scale
SPL	Sound Pressure Level
SV	Spectral Volume
T-S	Tollmien-Schlichting
URANS	Unsteady Reynolds Averaged Navier-Stokes
WHO	World Health Organization

Indicies

i,j	Cartesian Coordinate Plane
k,l,m	Nodal Position in Element
L,R	Left,Right Edge of Element
x,y,z	Cartesian Coordinate System
ξ, η, ζ	Reference Coordinate System

Superscripts

a	Irrational Component
C	Common Interface Flux
INV	Inviscid Flux
G,R	Global, Reference Solution Space
TRI	Triangular Element Face
VIS	Viscous Flux

Subscripts

c	Continuous
B	Boundary Value
e	Element Number
i	Cartesian Direction
J	Flux Jump at Element Interface
∞	Value at Free Stream
-,+	Incoming, Outgoing Direction

Notations

$\vec{\square}$	Vector Quantity
$\square^T$	Transpose
$\hat{\square}$	Normal Vector Component
$\overline{\square}$	Time-Averaged Component
$\tilde{\square}$	Favre Averaged Component
$\square'$	Fluctuation/Acoustic Component
$\lvert\square\rvert$	Magnitude
$\lVert\square\rVert$	Error Norm

Chapter 1

Introduction

This thesis's motivation is introduced, followed by a brief introduction to both acoustics and computational aeroacoustics (CAA). The numerical modeling of turbulence is then addressed, accompanied by a review of current status of CAA and future needs. The advantages of high-order numerical methods and their application towards CAA are presented. The Chapter is concluded with the objectives and outline of thesis.

1.1 Motivation

Historically, the primary focal point of aircraft jet engine design was to maximize thrust by increasing fan pressure ratios [3], subsequently increasing the jet velocity. However, the adoption of jet engines on commercial aircraft was quickly met with community opposition [4], as the high jet velocities proved to be exceedingly loud; therefore, in 1971, aircraft noise from large, commercial aircraft became the first environmental impact of aviation to be regulated at an international level [3]. The design of aircraft engines has since drastically changed to include lower fan pressure ratios and higher bypass ratios [3], resulting in decreased jet velocities and a significant reduction of jet noise [3, 4, 5]. Although modern aircraft engines substantially mitigate jet noise, the number of people subjected to adverse aircraft noise continues to increase each year as the demand for air travel continues to rise. In 2019, the International Air Transport Association (IATA) reported 37.8 million flights, carrying more than 4.4 billion passengers [6], and by 2040, the IATA predicts a 200 percent growth in the yearly number of flights [6]. In addition to the rapidly increasing demand for air travel, the number of people, particularly those living close to airports, is drastically increasing each year. In 2010, the Federal Aviation Administration (FAA) reported roughly 30 million people living in areas exposed to high aircraft noise levels [5]. Assuming no advancements in

aircraft engine technology, the FAA predicts this number could exceed 80 million people by 2040 [5]. The increasing demand for air travel, combined with the rapid population expansion near airports, poses a severe threat to public health, as those living in areas with high noise levels are more susceptible to hypertension, coronary heart disease, cardiovascular disease, and stroke [7, 8, 9, 10, 11, 12].

To minimize the detrimental side effects of aircraft noise, the International Civil Aviation Organization (ICAO) released the Balanced Approach to Aircraft Noise Management [3], containing four distinct noise abatement procedures [4]. Three procedures detail immediate actions to reduce aircraft noise, including land-use and management for airports, noise-reducing aircraft operational procedures, and aircraft operating restrictions [4]. The fourth and most prevalent procedure is the reduction of noise at its source [4], which demands that the "latest available noise reduction technology is incorporated into aircraft design" [4]. To foster innovation and ensure advancements in noise reduction technologies, the ICAO also sets medium and long-term noise reduction goals [3]. For example, the noise reduction goals for a twin-aisle commercial airplane are 19.5 and 26.5 EPNdB[1] by the years 2027 and 2037, respectively [3].

Achieving the noise reduction goals set forth by the ICAO necessitates tremendous advancements in both aircraft engine and body technologies; however, current aircraft testing techniques, such as wind tunnel modeling, are non-conducive to the iterative nature of the design process. Therefore, advanced modeling techniques, particularly computational fluid dynamics (CFD) and CAA, which significantly reduce testing time, must be integrated into the early design phases. As compared to CFD, CAA is still in its infancy as a modeling technique and requires "revolutionary algorithmic improvements to enable future advances in simulation capabilities" [14]. Thus, the motivation of this thesis is to verify, validate, and apply the novel, high-order flux reconstruction (FR) method as a CAA approach, and evaluate its potential in aiding the noise reduction goals set forth by the ICAO.

1.2 Introduction to Acoustics

The current section provides necessary background information for comprehension of the subject matter presented throughout this thesis, including any definitions, nomenclature, or physical phenomena pertinent to acoustics or CAA. The terminology purely related to acoustics is discussed first, followed by the introduction of the terminology relevant to CAA.

[1] Effective Perceived Noise (in Decibels), EPNdB, is a measure of the relative noisiness of an individual aircraft pass-by event [13].

1.2.1 Acoustic Terminology

The World Health Organization (WHO) defines noise as "disagreeable or undesired sound disruptive to hearing" [13]. However, this definition is highly subjective, as individuals perceive sound differently, and noise deemed disruptive to some may be non-disruptive or even pleasant to others. To lend objectivity towards this definition and classification, noise is quantified based on the pitch and sound pressure levels (SPL) of the sound waves.

The pitch is the subjective response to the frequency of sound waves [13]. The range of frequencies detectable by the human ear is generally considered to be between 20 Hz and 20 kHz, with the range most damaging to hearing occurring between 500 Hz and 2 kHz [2]. Sounds composed primarily of individual frequencies are referred to as tonal noises and are typically more disagreeable than sounds containing a wide range of frequencies, referred to as broadband noises [13]. The distinction between tonal and broadband noise is perfectly illustrated by analyzing highway traffic noise, in which the road, engine, and exhaust noises combine to create the broadband noise spectrum, while individual events, such as a car horn, produce identifiable and irritable tonal noises. While individual frequencies typically define tonal noises, a unique classification of tonal noise exists, which contains multiple frequencies located at integer multiples of the original frequency, referred to as the fundamental frequency. These regularly spaced frequencies are denoted as the harmonics of the fundamental frequency, with the highest harmonic determining the pitch [13].

The SPL, defined in equation 1.1, is the subjective response to the fluctuating pressure amplitude of sound waves [13]

$$\text{SPL (dB)} = 20log\left(\frac{p'_{rms}}{p_{ref}}\right), \tag{1.1}$$

where p'_{rms} is the root mean squared (RMS) sound pressure and p_{ref} is 20 μPa, which is the smallest pressure detectable by healthy human ears [2]. The range of pressure amplitudes detectable by the human ear is exceedingly large, and therefore a weighted logarithmic scale, known as the decibel, dB, scale, is applied to represent the extensive range of SPL in a more manageable fashion. Table 1.1 depicts the decibel scale range and contains a plethora of acoustic sources and their corresponding level of perception to the human ear.

Before introducing the necessary terminology for CAA, several physical phenomena pertinent to the propagation of acoustic waves require definition. Diffraction is defined as the bending of acoustic waves around the corners of an obstacle or through an opening [15] and is particularly relevant in the vicinity of sharp trailing edges or airfoil slats. Reflection is the bouncing of a sound wave off a surface [15] and

SPL (dB)	Source (distance from source)	Human Perception
180+	Rocket launch (50m)	
160-168	Shotgun blast (<1m)	Hearing loss
146-162	Firecracker (3m)	
135-140	Air raid siren (30m)	
115-130	Live rock concert (5m)	Threshold of pain
112-125	Snowmobile (<1m)	
109-120	Jack hammer (<1m)	
102-115	Chainsaw (<1m)	Very loud
93-114	Subway train (5m)	
98-112	Hand-held drill (<1m)	
98-110	Bulldozer (5m)	Loud
82-100	Heavy traffic (5m)	
72-93	Restaurant (<1m)	
71-91	Electric mixer (<1m)	Moderate
65-84	Dishwasher (<1m)	
62-70	Normal Conversation (<1m)	
29-40	Soft whisper (<1m)	Quiet
7-12	Normal breathing (<1m)	
0	Human threshold of hearing	

Table 1.1. Sound pressure level scale of human hearing [2]

dominates wall-bounded flows, including air ducts and exhaust pipes. Scattering is the process in which acoustic waves are deviated from a straight trajectory by localized non-uniformities [15], including but not limited to geometrical non-uniformities, such as trailing edges and steps, and flow non-uniformities, including vortices and shocks.

The following subsection details the numerical computation of sound and introduces the terminology relevant to CAA.

1.2.2 Computational Aeroacoustics Terminology

Acoustic waves are mechanical, longitudinal waves resulting from a pressure fluctuation traveling through a medium [16]. The fluctuation pressure, or more appropriately, the acoustic pressure, is defined as the difference between the instantaneous and time-averaged pressures

$$p'(x,t) \;=\; p(x,t) \;-\; \overline{p(x)}, \tag{1.2}$$

where p denotes pressure, $p(x,t)$ is the instantaneous pressure and the acoustic and time-averaged components of the pressure are denoted by the prime superscript and the overbar, respectively. CAA methods that calculate the acoustic pressure by directly applying Equation 1.2 are aptly referred to as direct methods. Direct CAA methods provide the most accurate solutions, since the governing

equations are themselves used in the calculation of the acoustic field; however, direct CAA methods are very computationally expensive and require extremely accurate numerical methods. Therefore, hybrid CAA methods, which compute the CFD variables in the near-field and apply a mathematical model to approximate the CAA variables in the far-field, are often applied to reduce computational burden. Note, in CAA, the near-field is typically defined as the region enclosed by a radius of two or three times the largest length scale, in which the effects of diffraction, reflection, and scattering are most dominant [13]. The far-field is then defined as the region beyond the near-field, extending to the boundaries of the computational domain [13]. The mathematical model employed by traditional hybrid methods approximates the acoustic pressure at the edge of the near-field as a combination of acoustic sources, specifically, monopoles, dipoles, and quadrupoles.

Acoustic monopoles are created by the repeated addition and removal of mass from a system and are analytically equivalent to a pulsating sphere [13]. As shown in Figure 1.1*a*, the acoustic pressure originates at the center of the monopole and propagates radially in all directions, establishing monopoles as highly efficient radiators of sound, with the acoustic intensity scaling proportionally to $M_a{}^4$ in the far-field [17, 18], where M_a is the Mach number. The radially symmetric propagation of the acoustic waves is further demonstrated by the directivity plot in Figure 1.1*b*, which portrays the angular distribution of acoustic pressure [13]. Monopoles are characterized by an individual frequency, namely, the frequency at which mass is added and removed from the system, and therefore act as highly tonal noise sources. Although the existence of exact, individual acoustic monopoles is exceedingly rare, several flow configurations, including turbulent combustion and the sound radiated from an exhaust pipe are well modeled by a linear combination of monopoles [15].

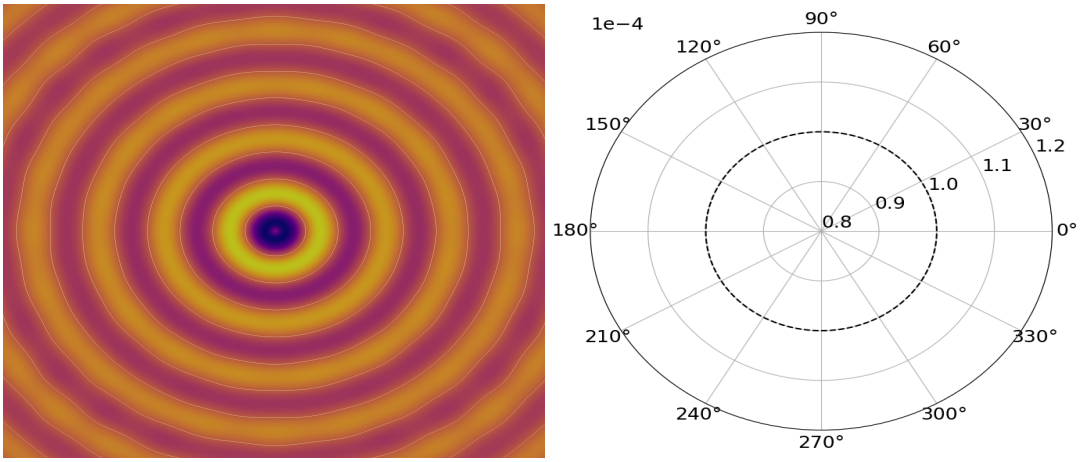

(a) Acoustic pressure contour

(b) RMS p' directivity

Figure 1.1. Acoustic monopole radiation characteristics

Acoustic dipoles are created by applying a fluctuating force to a fluid and behave equivalently to two monopoles pulsating in complete phase opposition [13], as shown in Figure 1.2*a*. As compared to monopoles, the acoustic pressure generated by dipoles is not radiated equally in all directions, epitomized by the characteristic 'figure-8' directivity contour in Figure 1.2*b*. Accordingly, dipoles are less effective radiators of sound, with the acoustic intensity scaling by $M_a{}^6$ in the far-field [18]; however, Curle [19] demonstrated that the presence of solid boundaries, particularly those with sharp edges, amplify the acoustic pressure radiated by dipoles, resulting in the SPL proportional to $M_a{}^5$ in the far-field. Depending on the orientation of the dipole, the acoustic pressure may be perceived as either tonal or broadband. Dipoles are the most common acoustic source and are most prevalent in configurations containing trailing edges and rotating fan blades [15].

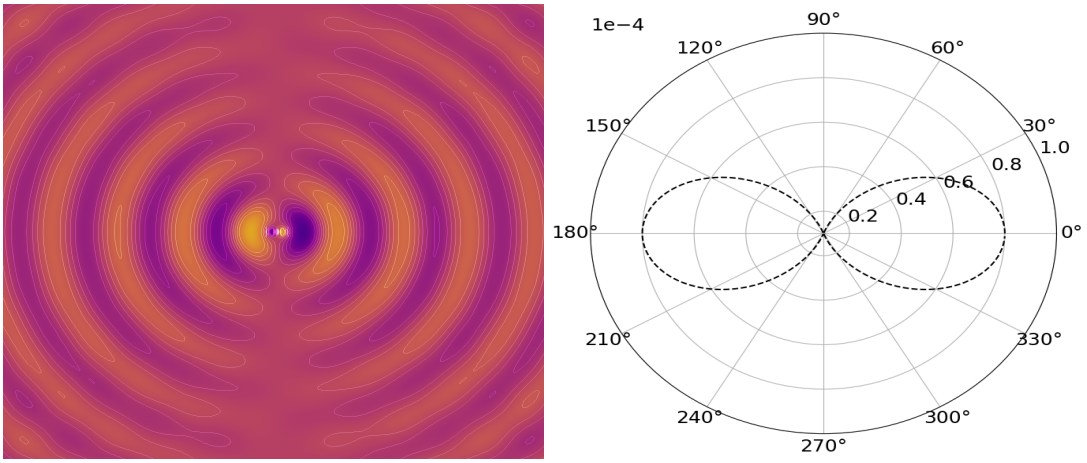

(a) Acoustic pressure contour

(b) RMS p' directivity

Figure 1.2. Acoustic dipole radiation characteristics

Acoustic quadrupoles are generated by fluctuating stresses acting on a fluid [13]. Quadrupoles are mathematically identical to two dipoles pulsating in opposition, as shown in Figure 1.3*a*. The alignment of the two dipoles creates a highly directional acoustic field, represented by the distinctive '4 leaf clover' directivity contour seen in Figure 1.3*b*. Acoustic quadrupoles are the least effective radiators of sound, with the acoustic intensity scaling proportional to $M_a{}^8$ in the far-field [20]. Quadrupoles are created by turbulent, vortical structures radiating in free space [13] and are intrinsically broadband in nature.

Although direct and hybrid CAA methods are inherently dissimilar, both require highly accurate CFD results, particularly in the near-field, to correctly calculate the SPL and acoustic directivity in the far-field. The necessity of high order numerical methods for CAA is a prevailing theme throughout this thesis and is discussed in further detail in subsequent sections.

The following section provides a brief review on the current state of CAA, addressing the proficiencies

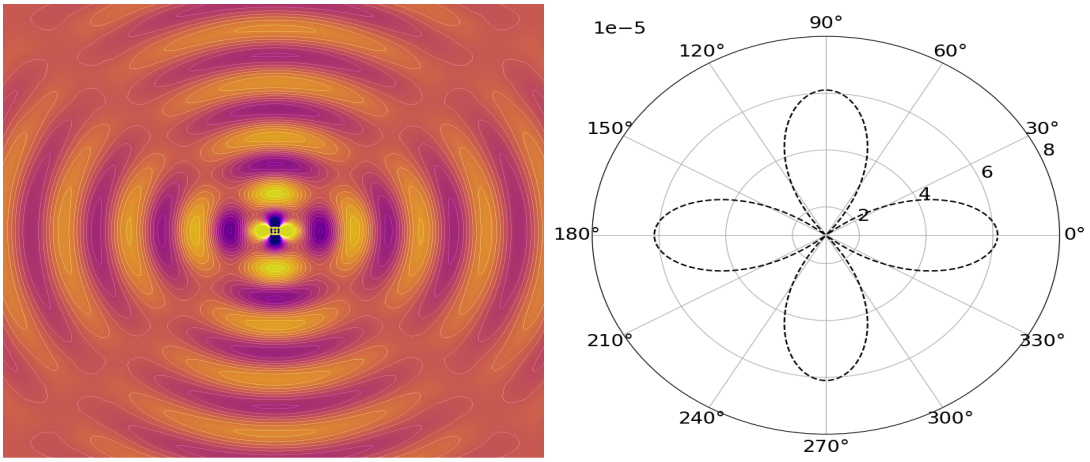

(a) Acoustic pressure contour

(b) RMS p' directivity

Figure 1.3. Acoustic quadrupole radiation characteristics

as well as future needs.

1.3 Current State of Computational Aeroacoustics

Aided by advancements in computing power in recent decades, the field of CFD has undergone considerable development, resulting in powerful and robust numerical methods that accurately and efficiently compute time-dependent aerodynamic solutions [21]. The tremendous success achieved in the field of CFD seemingly bodes well for the field of CAA, as both hybrid and direct CAA methods necessitate highly accurate near-field CFD results; however, early applications of CFD towards CAA applications yielded highly erroneous results [21, 22, 23]. Subsequently, the field of CAA has undergone separate development from that of CFD.

The bifurcation of the field of CAA from CFD occurred in the mid-1980s [24], at which time the prevailing numerical methods were the classic finite volume (FV) and finite difference (FD) methods. The enhanced grid resolution required to resolve the small length scales of acoustic waves adequately proved exceedingly expensive for the low order schemes; therefore, direct CAA methods were deemed too computationally expensive for practical applications [21, 25, 26]. Accordingly, hybrid methods received significant attention and quickly became the primary method of CAA. The maturation of hybrid methods has introduced several prominent CAA features, most notably developing high-order numerical methods well suited to compute acoustic propagation over large distances [21]. Additionally, the continued development of hybrid methods has drastically aided the evolution of highly specialized acoustic non-reflecting boundary conditions (NRBC), which maintain the accuracy of the simulation by eliminating any spurious, non-physical reflections at the boundaries of the computational domain

[21, 22, 23, 25]. Hybrid methods provide a fast and relatively inexpensive means of calculating the far-field acoustics; however, "aerodynamic noise generation is a complicated process and cannot be fully described solely by an acoustically equivalent source term " [23]. Therefore, to gain deeper insight into the acoustic generation and propagation processes, more accurate CAA methods must be considered, including the transition to direct CAA methods.

Despite the advances in high order numerical schemes, the direct computation of sound is still widely considered implausible with conventional FD and FV methods [21, 22, 23, 25], as the computational requirements remain impractically large, owing to their inefficient operation on modern hardware [27]. The advent of high order numerical methods that operate extremely efficiently on modern hardware, including the FR method [27], has been shown to enhance the feasibility of high fidelity CFD simulations; however, the exploration of these techniques for direct CAA applications is a new field of research [25]. As direct methods become increasingly prevalent, further research must be devoted to developing boundary conditions (BC) that allow the smooth passage of both aerodynamic and aeroacoustic flow features without generating spurious reflections [22, 23, 25]. Additionally, more advanced turbulence models must be adapted which accurately resolve the flow while minimizing computational expense [22, 23, 25]. Lastly, the direct computation of sound beyond the near-field necessitates some variation of reduced order modeling [22, 25], as the computational expense rapidly increases with increasing distance from the acoustic source. Note, the focus of this thesis is the application of the FR method as a direct near-field CAA method, and therefore reduced-order modeling techniques are not addressed.

The following section details the numerical modeling of turbulence and examines three prevalent turbulence approaches.

1.4 Numerical Modeling of Turbulence

Turbulence is defined as the three-dimensional, rotational, chaotic, diffusive, and dissipative motion of a fluid [28, 29], and emerges in a wide range of engineering applications, particularly aeroacoustics, as the broadband noise content is directly correlated to the turbulence intensity [30].

A characteristic feature of turbulence is the substantial disparity in length scales, ranging from the large, coherent, highly-energetic eddies down to the diminutive turbulent fluctuations. The turbulence intensity and spectrum of length scales is strongly dictated by the Reynolds number, R_e, which acts as the

ratio of inertial to viscous forces present in the flow

$$R_e = \frac{\rho V_\infty L_c}{\mu}, \tag{1.3}$$

where ρ, V_∞, and μ are the fluid density, magnitude of the free-stream velocity, and dynamic viscosity, respectively, and L_c is the characteristic length. The relationship between the smallest and largest length scales, l_t and L_t, respectively, is a function of the Reynolds number and is given by the Kolmogorov micro-scale [28, 31]

$$\Delta x_s \approx l_t = \left(\frac{V_t L_t}{\mu}\right)^{\frac{3}{4}} L_t = R_e^{-\frac{3}{4}} L_t, \tag{1.4}$$

where V_t is the velocity magnitude of the smallest length scales and Δx_s is the numerical grid spacing required to resolve the smallest length scales. The fidelity of a turbulence simulation is dictated by the range of length scales numerically resolved by the applied turbulence approach. High-fidelity approaches, including direct numerical simulations (DNS) strictly adhere to the physical laws governing fluid motion by numerically resolving the entire range of length scales present, whereas low-fidelity approaches, such as the Reynolds averaged Navier-Stokes (RANS) equations, approximate the physics of the flow and require mathematical models to resolve all unsteady length scales. Although DNS provides the highest levels of fidelity, its application is limited, as numerically resolving the entire spectrum of length scales poses a daunting computational challenge. The required number of degrees of freedom, N_{DOF}, to resolve the smallest length scales increases exponentially with increasing Reynolds numbers [31]

$$N_{DOF} = \left(\frac{L}{\Delta x_s}\right)^3 \approx \left(\frac{L}{L_t}\right) R_e{}^{\frac{9}{4}}, \tag{1.5}$$

where L is the edge length of a uniform cubic domain. To alleviate the massive computational burden of DNS, medium-fidelity turbulence approaches, including large eddy simulations (LES) can be used, which numerically resolve the larger length scales and require a model to resolve the smaller length scales [28, 31], as shown in Figure 1.4, which plots the wavenumber, k_w, against the energy contained at each wavenumber, E_w, and details the resolution limits of RANS, LES, and DNS.

The following subsections provide further detail regarding the turbulence approaches introduced above, detailing any necessary mathematical derivations and addressing their relevancy towards CAA.

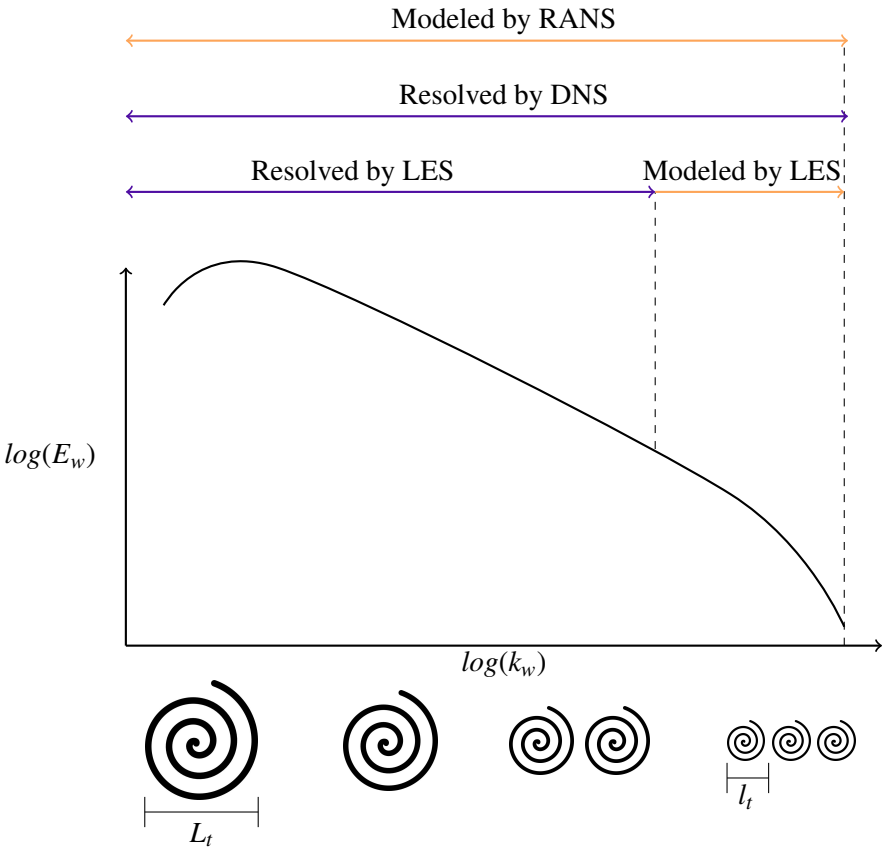

Figure 1.4. Turbulent energy spectrum

1.4.1 Reynolds Averaged Navier-Stokes

The least computationally expensive approach to numerically model turbulence is the RANS equations [28, 31, 32]. The RANS method utilizes Reynolds decomposition, in which an instantaneous variable is decomposed into its subsequent time-averaged and fluctuating components

$$\vec{V}(x,t) = \overline{\vec{V}(x)} + \vec{V}(x,t)', \tag{1.6}$$

where the over-bar and prime superscript denote the time-averaged and fluctuating components, respectively, to yield a time-averaged variation of the Navier-Stokes (NS) equations [28]. The Reynolds decomposition of the incompressible conservation of momentum equation is

$$\rho\overline{\frac{D\left(V_j\right)}{Dt}} = \frac{\partial}{\partial x_i}\left[\overline{p}\delta_{ij} - \rho\overline{V_i{}'V_j{}'} + \mu\left(\frac{\partial\overline{V}_i}{\partial x_j} + \frac{\partial\overline{V}_j}{\partial x_i}\right)\right], \tag{1.7}$$

where δ_{ij} is the Kronecker delta and the $\rho\overline{V_i{}'V_j{}'}$ term, often referred to as the Reynolds stresses, accounts for the turbulent fluctuations in the momentum of the fluid [28, 31]. The non-linearity of the Reynolds

stresses necessitates the use of eddy-viscosity models to close the RANS system of equations [28].

Although extensive research has been devoted towards developing more accurate and highly specialized eddy-viscosity models [29], the time-averaging employed by the RANS equations neglects the unsteady nature of the flow, rendering the RANS equations largely inept at predicting transitional or separated flows [28, 31]. Furthermore, aeroacoustics is fundamentally a time-dependent process; therefore, removing the unsteady effects of the flow expunges the acoustic field. The modeling inaccuracies and inherent time-averaging of the RANS equations invalidate its application in direct CAA.

1.4.2 Large Eddy Simulation

The methodology behind LES is to numerically resolve the large, energetic eddies and mathematically model the effects of the smaller eddies and fluctuations [28, 31]. A low-pass spatial and temporal filtering operator is applied to remove the small-scale information from the solution, after which the effects of the removed information are modeled using a sub grid scale (SGS) model [28]. The SGS model typically adds artificial viscosity to the numerical simulation by appending an auxiliary stress tensor, which mimics the dissipative nature of the small scale eddies, to the conservation of momentum equation [28].

By numerically resolving the interactions between the large scale eddies, LES provides a more accurate solution than RANS. Additionally, by selectively removing the small scale information from the system, which requires the most computing power to resolve [31], LES reduces the computational cost compared to DNS. The application of LES towards CAA has shown promise [22, 25, 29, 30]; however, the effects of removing certain length scales on the acoustic generation process is still unknown [22, 23, 32], including the inability to capture the highest frequencies, typically generated by the filtered length scales, and the subsequent impact on the broadband noise spectrum.

1.4.3 Direct Numerical Simulation

DNS provides the most accurate yet most computationally expensive approach to modeling turbulence, as the entire range of turbulent length scales is numerically resolved. The absence of a mathematical model in DNS provides tremendous physical insight towards the mechanisms and processes responsible for acoustic generation, thus lending potential for optimization and ultimately satisfying the ICAO's noise reduction goals. Therefore, to thoroughly and meticulously validate the FR method as a suitable approach to CAA, DNS is exclusively applied as the turbulence approach throughout this report.

Before proceeding to the following section, several important conclusions must be made regarding the current state of turbulence modeling. Currently, the application of DNS is limited to turbulent flows

with low to moderate Reynolds numbers [23, 25]; however, the advent of high order numerical methods that provide geometric flexibility and operate efficiently on modern hardware, including the FR method, enables simulations with increased Reynolds numbers. Secondly, the turbulence approaches detailed above were chosen to illustrate the difference between low, medium, and high-fidelity approaches and do not represent all available turbulence approaches. A plethora of low and medium-fidelity approaches have been established, including but not limited to the unsteady Reynolds averaged Navier-Stokes (URANS) equations, implicit large eddy simulations (ILES), and detached eddy simulations (DES) [22]. Although very successful in CFD applications, low and medium-fidelity turbulence approaches can only capture the acoustics generated by the numerically resolved flow features, and as such, have not extensively been applied toward CAA. As the field of CAA continues to progress, the necessity of high-fidelity turbulence models that do not employ time-averaging significantly increases.

The advantages of high order numerical methods are addressed in the following section.

1.5 Advantages of High-Order Numerical Methods

The dissipative nature of traditional, low-order FD and FV codes necessitate an impractically large number of degrees of freedom (DOF) to sufficiently resolve the small length scales characteristic of CAA. These excessive grid resolutions yield exceedingly large computational problems that cannot be solved on even the largest parallel computer architectures [33]. These computational restrictions, coupled with the stringent demand for highly accurate computational aeroacoustic solutions, have promoted the development of high-order numerical methods. Ekaterinaris [33] compares the error convergence rate of a second-order scheme to that of a high-order scheme to demonstrate the advantage of high-order numerical methods. The second-order scheme yields an error proportional to Δx^2, where Δx is the numerical grid spacing. The high-order scheme of order n, such that $n \geq 3$, produces an error proportional to Δx^n; therefore, as the grid spacing is refined, the error produced by the high-order scheme decreases faster than the low-order scheme. This enables high-order schemes to produce more accurate solutions with fewer total DOF than low-order schemes. The proficiency of high-order methods is further exemplified by Vermeire *et al.* [34], who provide a detailed comparison on the accuracy and efficiency of high-order solutions against industry-standard low-order solutions. Vermeire *et al.* demonstrate that high-order solutions are considerably cheaper and far more accurate than corresponding low-order solutions. The extension to high-order methods, coupled with the tremendous increase in computing power over recent decades [27], enables larger, more complex simulations to be performed with increased accuracy and

reduced computational cost.

1.6 Thesis Objectives

This thesis contains two primary objectives. The first objective is to demonstrate the superiority of high-order numerical methods in CAA, particularly those that operate efficiently on modern hardware and provide geometric flexibility, by comparing the accuracy, required number of DOF, and run times for multiple polynomial degrees across a suite of verification test cases. The second objective is to establish the FR method as an accurate and efficient approach to direct CAA by performing several validation studies, including the flow over a cylinder, turbulent flow over a cavity, and numerical experiments of a National Advisory Committee for Aeronautics (NACA) 0012 airfoil at varying angles of attack.

1.7 Thesis Outline

Chapter 1 provides a brief introduction to the field of CAA, addressing its current-state and the necessity for higher-order solutions, followed by a summary of the necessary and relevant acoustic terminology and features.

Chapter 2 derives the governing equations of fluid dynamics and assesses their pertinence towards CAA.

Chapter 3 introduces an array of numerical methods available to spatially discretize the governing equations of fluid dynamics and details the suitability of each as applied to CAA. The FR method is introduced as the primary focus of this report, with the complete numerical derivation presented, followed by a review of its performance on modern hardware systems.

Chapter 4 details the temporal discretization schemes implemented throughout this report and summarizes the advantages and shortcomings of each.

Chapter 5 administers an in-depth analysis of the prevailing numerical methods applied in CAA, followed by an examination of the computational challenges inherent to the field of CAA.

Chapter 6 verifies the FR method's ability to sufficiently resolve each of the computational obstacles fundamental to CAA. Additionally, the proficiency and necessity of high-order solutions are addressed by comparing the solutions of several polynomial orders.

Chapter 7 assesses the aptitude of the FR method applied as a direct CAA approach via numerical simulation of the flow over a cylinder and a deep cavity.

Chapter 8 demonstrates the proclivity of the FR method towards industrial application by simulating a NACA0012 airfoil in two and three dimensions at varying angles of attack.

Chapter 9 finalizes the report by detailing the conclusions and recommendations for future work.

Chapter 2

Governing Equations

The well-known conservation laws, which dictate fluid motion and together comprise the NS equations, are first derived in this Chapter, followed by their application and relevancy towards CAA. The Chapter concludes with the complete derivation of the NS equations, which serve as the governing equations of fluid motion in this study.

2.1 General Conservation Law

Consider a fixed domain, Ω, with closed boundaries, S. Neglecting any source terms, a general conservation law may be written in integral form as

$$\frac{d}{dt}\int_{\Omega} u dx + \int_{S} \vec{f}(u) \cdot \hat{n} dS = 0, \tag{2.1}$$

where $u = u(x,t)$ is a conserved variable, $\vec{f}(u)$ is the flux of the conserved variable across S, with the arrow denoting a vector quantity, $\hat{n}$ is the outward surface normal, and x and t denote space and time, respectively. By applying Gauss's theorem, which relates the flux of u through a closed surface to the divergence of the field inside the fixed domain,

$$\int_{\Omega} (\nabla \cdot u) d\Omega = \int_{S} (u \cdot \hat{n}) dS\,. \tag{2.2}$$

Equation 2.1 may then be re-written in the form

$$\frac{d}{dt}\int_{\Omega} u dx + \int_{\Omega} \nabla \cdot \vec{f}(u) d\Omega = 0, \tag{2.3a}$$

$$\int_{\Omega} \left(\frac{\partial u}{\partial t} + \nabla \cdot \vec{f}(u) \right) = 0. \tag{2.3b}$$

Since no restrictions have been placed on the size of Ω, Equation 2.3b must hold for any domain size; therefore,

$$\frac{\partial u}{\partial t} + \nabla \cdot \vec{f}(u) = 0 \tag{2.4}$$

is the general conservation law in differential form. Note that all simulations presented in this report were computed using the differential form, and therefore only the differential form of the governing equations will be presented.

2.2 Conservation of Mass

The law of conservation of mass states that mass can neither be created nor destroyed. If the density of the fluid is integrated over Ω, we obtain the mass, m, of the fluid; therefore, ρ is taken as the conserved variable in Equation 2.1. By multiplying the density by the velocity, and integrating over S, we obtain the flux of mass across S; thus, $\rho\vec{V}$ is taken to be the flux variable in Equation 2.1. The general conservation law may be re-cast in the following form

$$\frac{d}{dt}\int_{\Omega} \rho dx + \int_{S} \rho \vec{V} \cdot \hat{n} dS = 0. \tag{2.5}$$

Following the steps from the previous section, conservation of mass may be written in differential form as

$$\frac{\partial \rho}{\partial t} + \nabla \cdot (\rho \vec{V}) = 0. \tag{2.6}$$

2.3 Conservation of Momentum

Newton's second law states that the sum of forces, F, acting on a system is equivalent to the time rate of change of the system's momentum

$$\sum F = \frac{d}{dt}(m\vec{V}). \tag{2.7}$$

In deriving the conservation of mass, we determined density to be the conserved variable. Since momentum is the product of mass and velocity, it follows that $\rho\vec{V}$ serves as the conserved variable in Equation 2.1 while $\rho\vec{V} \otimes \vec{V}$ acts as the flux. Therefore the conservation of momentum may be written in differential form as

$$\frac{\partial\left(\rho\vec{V}\right)}{\partial t} + \nabla \cdot \left(\rho\vec{V} \otimes \vec{V}\right) = \sum_{\Omega} F. \tag{2.8}$$

The Cauchy momentum equation defines the sum of forces acting on Ω as

$$\sum_{\Omega} F = \nabla \cdot \bar{\bar{\sigma}} + \vec{F_b}, \tag{2.9}$$

where $\vec{F_b}$ is the sum of body forces acting on the fluid and $\bar{\bar{\sigma}}$ is the Cauchy stress tensor, defined as

$$\bar{\bar{\sigma}} = \begin{bmatrix} \sigma_{xx} & \tau_{xy} & \tau_{xz} \\ \tau_{yx} & \sigma_{yy} & \tau_{yz} \\ \tau_{zx} & \tau_{zy} & \sigma_{zz} \end{bmatrix}, \tag{2.10}$$

where σ_{ij} is the normal stress acting in the ij plane and τ_{ij} is the shear or viscous stress acting in the ij plane. The (mechanical) pressure,

$$p = -\frac{1}{3}\left(\sigma_{xx} + \sigma_{yy} + \sigma_{zz}\right), \tag{2.11}$$

which is equivalent to the negative mean normal stress, can be factored out of Equation 2.10, which then may be written more compactly as

$$\sigma_{ij} = -pI + \bar{\tau}, \tag{2.12}$$

with I being the identity matrix and $\bar{\tau}$, which includes all off diagonal entries of Equation 2.10, defined as

$$\bar{\tau} = \mu\left[\nabla\vec{V} + \left(\nabla\vec{V}^T\right)\right] - \frac{2\mu}{3}\left(\nabla \cdot \vec{V}\right)I. \tag{2.13}$$

With all forces acting on the fluid defined, the conservation of momentum equation may be written in differential form as

$$\frac{\partial\left(\rho\vec{V}\right)}{\partial t} + \nabla \cdot \left(\rho\vec{V} \otimes \vec{V} - \sigma_{ij}\right) = \vec{F_b}. \tag{2.14}$$

2.4 Conservation of Energy

Similar to the law of conservation of mass, the law of conservation of energy states that energy can neither be created nor destroyed. The first law of thermodynamics, which is an adaptation of the law of conservation of energy for thermodynamic processes, states that the change in internal energy of a closed system is equal to the amount of heat added to the system less the thermodynamic work done by the system, as seen below

$$\Delta E = Q - W, \tag{2.15}$$

where ΔE is the change in internal energy, Q is the net heat added to the system, and W is the net work done by the system. In thermodynamics, it is common to work with specific variables, which do not depend on the mass of the system. Thus dividing Equation 2.15 by the mass

$$\Delta e = q - w, \tag{2.16}$$

where e, q, and w are the specific values of internal energy, heat, and work, respectively, we obtain the specific form of the first law of thermodynamics. The specific internal energy is comprised of

$$e = e_t + e_k, \tag{2.17}$$

where e_t is the specific thermal energy and e_k is the specific kinetic energy within the closed system. Following the law of conservation of energy, the specific energy acts as the conserved variable in Equation 2.4. The flux value is not as straight forward to calculate. As before, the flux vector is the product of the conserved variable and the velocity. Additionally, the stress tensor defined in Equation 2.10 convects energy from the domain, and therefore $\bar{\bar{\sigma}}\vec{V}$ is also a flux vector. Lastly, according to Fourier's law of thermal conduction, the heat flux vector, $\vec{q}$, is defined as

$$\vec{q} = -\kappa \nabla T, \tag{2.18}$$

where κ is thermal conductivity of the fluid and T is the temperature. With the conservative and flux values known, the conservation of energy equation can be written in differential form as

$$\frac{\partial e}{\partial t} + \nabla \left(e\vec{V} - \bar{\bar{\sigma}}\vec{V} + \vec{q} \right) = \vec{f}\vec{V}. \tag{2.19}$$

With the pressure and temperature unknown, the ideal gas law

$$p = \rho r T, \tag{2.20}$$

where r is the specific gas constant, equates the two variables.

2.5 Advection Equation

The linear advection equation describes the transport of any passive scalar value with advection velocity, α_a,

$$\frac{\partial u}{\partial t} + \alpha_a \nabla \cdot (u) = 0. \tag{2.21}$$

As seen in Figure 2.1, the value of the scalar quantity, u, does not change in amplitude but merely advects through the domain.

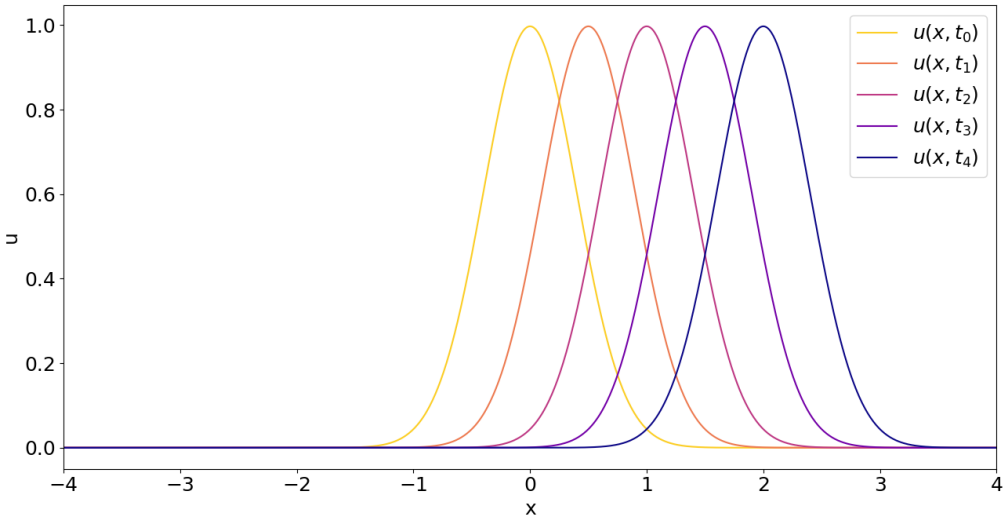

Figure 2.1. 1D advection equation

The linear advection equation is obtained by applying the conservation of mass equation while neglecting the conservation of momentum and energy equations. Advection is the primary method of acoustic propagation, and therefore an intensive study was performed on the ability of the FR method to accurately advect waves of different wavenumbers and advection speeds, of which the results are presented in the verification section.

2.6 Burgers Equation

Burger's equation depicts the conservation of momentum equation in a constant density and temperature fluid, while neglecting the conservation of mass and energy equations

$$\frac{\partial \vec{V}}{\partial t} + \frac{1}{2}\nabla \cdot \left(\vec{V} \otimes \vec{V}\right) = 0. \tag{2.22}$$

The $\nabla \cdot \left(\vec{V} \otimes \vec{V}\right)$ term in Equation 2.22 indicates that fluid is not advected through the domain at a constant speed, as seen in the linear advection equation, but rather at a speed relative to the local velocity of the fluid, which is liable to create shocks, as seen in Figure 2.2, in which the artificial dissipation shock capturing method of Persson and Peraire [35] was applied to mitigate the Gibbs-type oscillations in the vicinity of the shock.

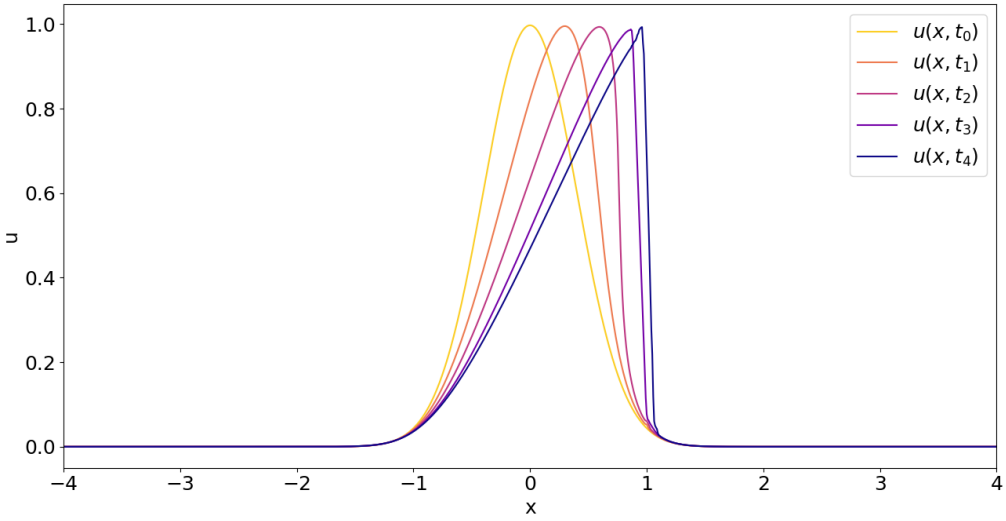

Figure 2.2. 1D Burger's equation

At subsonic speeds ($M_a \lesssim 0.7$), acoustic propagation via Burger's equation is exceedingly rare; however, at transonic speeds ($0.7 \lesssim M_a < 1.0$) and above, Burger's equation is analogous to acoustic propagation in the form of sonic booms.

2.7 Diffusion Equation

The linear diffusion equation is an adaptation of the conservation of energy equation, which characterizes the transition of high concentrations of energy to an equilibrative state while assuming zero flow velocity and neglecting the conservation of mass and momentum equations, as seen below

$$\frac{\partial\left(c_p T\right)}{\partial t} + \nabla \cdot (-\kappa \nabla T) = 0, \tag{2.23}$$

where c_p is the specific heat at constant pressure. Figure 2.3 depicts the 1D diffusion equation. In the field of CAA, diffusion plays no role in acoustic propagation, but serves as an acoustic generation mechanism, particularly aiding in the viscous breakdown of turbulent eddies.

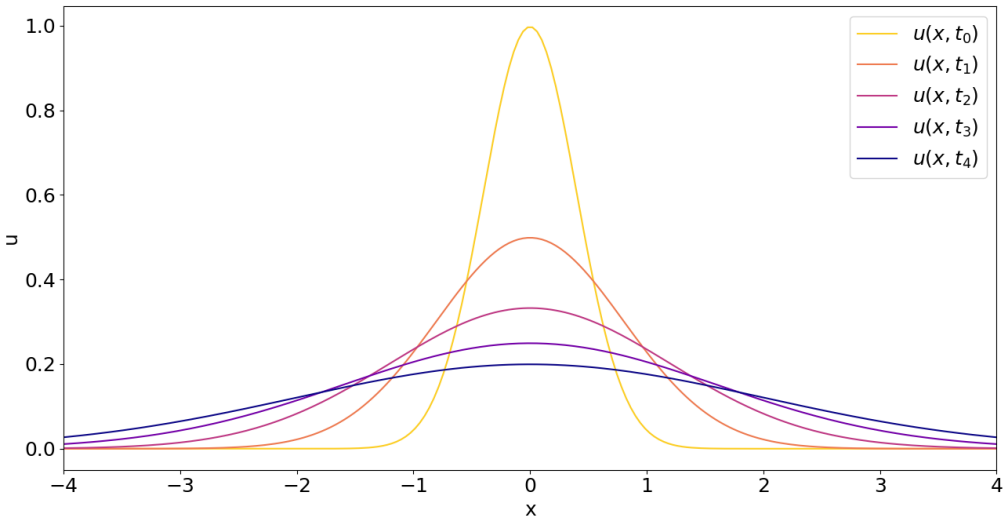

Figure 2.3. 1D diffusion equation

2.8 Euler and Navier-Stokes Equations

The Euler equations, which govern inviscid, compressible fluid flows, are obtained by combining the conservation of mass, momentum, and energy equations while neglecting the viscous flux terms in the conservation of momentum equation as well as thermally conductive flux terms in the conservation of energy equation. The Euler equations are written compactly as

$$\frac{\partial \vec{u}}{\partial t} + \nabla \cdot \vec{f}^{\,INV} = 0, \tag{2.24}$$

where the superscript INV denotes the vector of inviscid fluxes. The three-dimensional expansion of the Euler equations can be seen as

$$\begin{aligned} \vec{u} &= \begin{Bmatrix} \rho \\ \rho V_x \\ \rho V_y \\ \rho V_z \\ E \end{Bmatrix}, \\ \vec{f}^{\,INV} &= \begin{Bmatrix} \rho V_x & \rho V_y & \rho V_z \\ \rho V_x^2 + p & \rho V_y V_x & \rho V_z V_x \\ \rho V_x V_y & \rho V_y^2 + p & \rho V_z V_y \\ \rho V_x V_z & \rho V_y V_z & \rho V_z^2 + p \\ V_x (E + p) & V_y (E + p) & V_z (E + p) \end{Bmatrix}, \end{aligned} \tag{2.25}$$

where $\vec{x} = [x, y, z]^T$ denotes the spatial coordinate and the ideal gas law relates the pressure to the total energy per unit volume as

$$E = \frac{p}{\gamma - 1} + \frac{1}{2}\rho \vec{V} \cdot \vec{V}, \quad \vec{V} = \left[V_x, V_y, V_z\right]^T, \tag{2.26}$$

and the specific weight, γ, is defined by the ratio of the specific heat at constant pressure to the specific heat at constant volume, c_v,

$$\gamma = \frac{c_p}{c_v}. \tag{2.27}$$

The NS equations are an extension of the Euler equations to include the effects of viscosity and thermal conductivity [27]. All viscous and thermally conductive flux terms in the conservation laws are combined into a separate flux vector, f^{VIS}. The NS equations can then be written compactly as

$$\frac{\partial \vec{u}}{\partial t} + \nabla \cdot \left(\vec{f}^{\,INV} - \vec{f}^{\,VIS} \right) = 0. \tag{2.28}$$

The three dimensional expansion of the viscous flux vector is given by

$$\vec{f}^{\,VIS} = \begin{Bmatrix} 0 & 0 & 0 \\ \tau_{xx} & \tau_{yx} & \tau_{zx} \\ \tau_{xy} & \tau_{yy} & \tau_{zy} \\ \tau_{xz} & \tau_{yz} & \tau_{zz} \\ V_x\tau_{xx} + \frac{\mu c_p}{P_r}\partial_x T & V_y\tau_{yy} + \frac{\mu c_p}{P_r}\partial_y T & V_z\tau_{zz} + \frac{\mu c_p}{P_r}\partial_z T \end{Bmatrix}, \tag{2.29}$$

where P_r is the Prandtl number, defined as the ratio of momentum diffusivity to thermal diffusivity,

$$P_r = \frac{c_p \mu}{\kappa}, \tag{2.30}$$

and the ideal gas law describes the relationship between temperature and pressure as

$$T = \frac{p}{c_v (\gamma - 1)\rho}. \tag{2.31}$$

The following Chapter details the numerical discretization of the spatial derivative in Equation 2.4. Several numerical methods are presented with their advantages and disadvantages discussed. Finally, the FR method is introduced with a complete numerical derivation, followed by an assessment of the operation and performance of the FR method on modern hardware.

Chapter 3

Spatial Discretization

The general conservation law in Equation 2.4 incorporates both a temporal term, $\frac{\partial}{\partial t}$, and a spatial term, $\frac{\partial}{\partial x}$. The following sections illustrate standard methods of discretizing the spatially dependent term and the advantages and disadvantages of each method.

3.1 Finite Volume Method

As shown in Figure 3.1, the FV method represents a continuous partial differential equation (PDE) using a discrete number of volumes, each assuming a constant value.

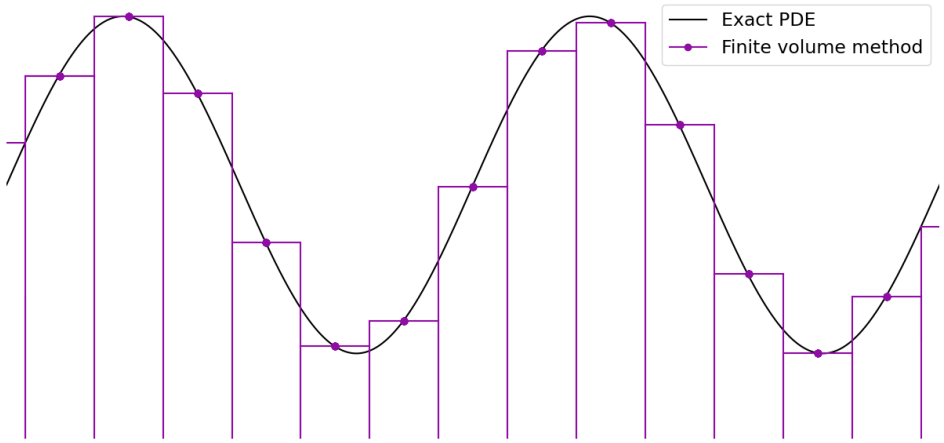

Figure 3.1. Finite volume method

The FV method solves the conservation laws in integral form, ensuring conservation and facilitating the treatment of solution discontinuities, particularly shocks. As no additional treatment is required near

solid boundaries, the FV method is applicable to a wide range of geometries. On the other hand, extension to higher-orders of accuracy can only be achieved by increasing the number of volumes, which greatly increases computational cost.

3.2 Finite Difference Method

The FD method approximates a continuous PDE using a discrete number of points, as shown in Figure 3.2.

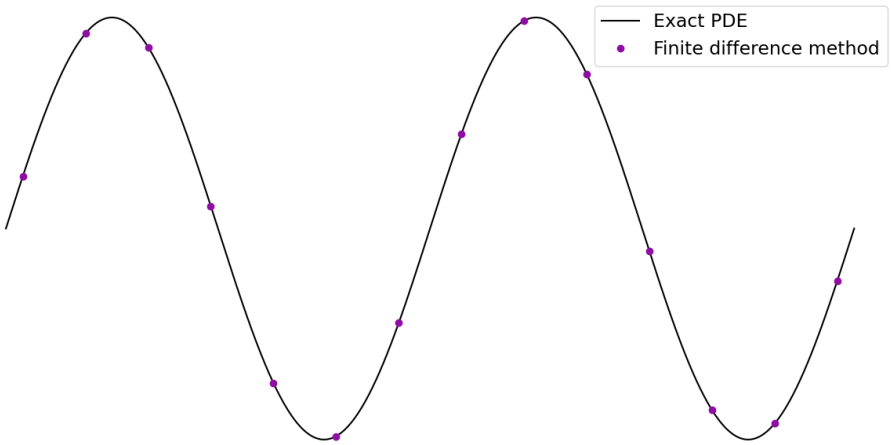

Figure 3.2. Finite difference method

The FD method is the simplest method to implement, and extension to high orders of accuracy is relatively simple; however, the FD method solves the conservation equations in the divergence form and therefore is generally not conservative. Additionally, the presence of solid boundaries requires special treatment and must be formulated on regular curvilinear grids, which makes the FD method generally not applicable for domains with complex geometries.

3.3 Finite Element Method

The finite element (FE) method approximates the exact PDE using a discrete number of volumes or elements, each consisting of a discrete number of solution points. A set of basis functions are applied at each point within the element to construct a continuous polynomial spanning the entire element. FE methods combine the geometric flexibility of the FV method with the high order capabilities of the FD

method.

3.3.1 Continuous Finite Element Method

The continuous finite element (CFE) method uses a set of global basis function at each solution point to create an approximate solution polynomial within each element. The use of global basis functions imposes the restriction that the solutions at element interfaces be identical, thus creating a continuous polynomial.

3.3.2 Discontinuous Finite Element Method

The discontinuous finite element (DFE) method uses a set of local basis functions, allowing for discontinuities at element interfaces while ensuring a continuous polynomial within each element. The choice of basis functions used dictates the numerical behavior of the method, for example, the usage of the well-known Lagrange polynomials results in the formulation of the discontinuous Galerkin (DG) method. The DG method has emerged as an attractive numerical method for CFD as it offers geometric flexibility and arbitrarily high orders of accuracy [36]. The native form of the DG method solves the conservation laws in integral form; however, applying integration by parts transforms the DG method to its differential form, thus recovering a strong form of the solution. Figure 3.3 illustrates the differences between the CFE and DFE methods.

For both the CFE and DFE methods, extension to higher-orders is achieved by increasing the number of solution points within each element. Since the CFE method uses a set of global basis functions to construct the solution polynomial, a matrix containing all solution points must be constructed to advance the solution in time, which quickly becomes memory intensive. Conversely, by using a set of local basis functions, the DFE method requires only the solution points within an element and its immediate neighbors to temporally advance the solution. While this does reduce the memory usage, an additional calculation is required at each element interface to determine the value of the flux.

3.4 Spectral Methods

Spectral methods can be seen as a combination of the FE method with either the FV or FD methods. The domain is discretized in a similar fashion to the FE method and then either the FD or FV method is applied locally within each element. A feature unique to the spectral methods is that the solution and solution flux are computed using a separate set of points, the effects of which are discussed below.

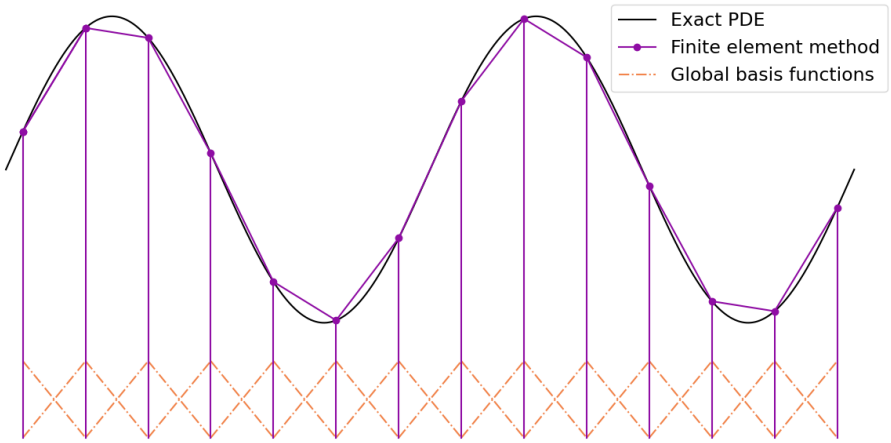

(a) Continuous finite element method

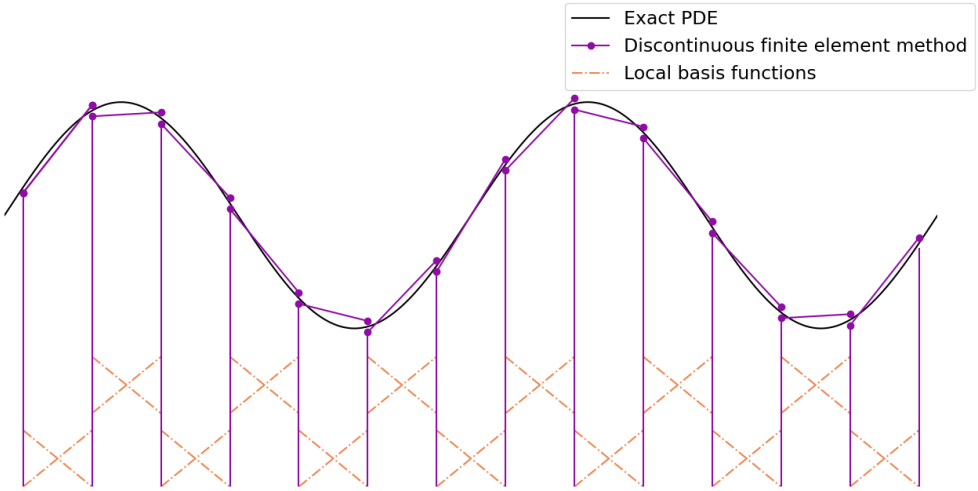

(b) Discontinuous finite element method

Figure 3.3. Finite element methods

3.4.1 Spectral Volume Methods

The spectral volume (SV) method couples the geometric flexibility of the FV method with the high order capabilities of the FE method [37]. The domain is again discretized using a discrete number of elements, each of which is further discretized by a set of control volumes. The classic FV method is applied within each element to approximate the solution. The SV method introduces two separate sets of points to calculate the solution and solution flux, promoting accelerated convergence. Furthermore, the SV method is particularly adept at capturing shocks [37], as the entire shock can be resolved within a single control

volume inside a single element. The SV method can be efficiently implemented on structured grids; however, the formation of control volumes inside an arbitrarily shaped element is not a trivial process and requires specialized treatment [37, 38]. For the same reason, the extension to higher-orders of accuracy, especially for 3D elements, is severely limited [38].

3.4.2 Spectral Difference Method

The spectral difference (SD) method, which recovers the well known staggered grid (SG) method in 1D, was established as an alternative to the SV method in an attempt to remove the high order obstacles experienced by the SV method [38]. Similar to the SV method, the SD method discretizes the domain into a discrete number of elements. The elements each contain a discrete number of points, along which the classic FD method is applied. The solution points are chosen to lie completely within the element while the flux points extend to the element interfaces. The separation of the flux and solution points allows the SD method to achieve very high error convergence rates and high orders of accuracy; however, the additional set of points is more difficult to implement and is more computationally demanding. Spectral methods exploit both the high order capabilities of the FE method and the intrinsic properties of the classical FD and FV methods. As such, they are applicable to a wide range of CFD problems. Additionally, the separation of the flux and solution points promotes a highly stable solution [36, 37]. There are, however, two distinct shortcomings of the SD method. The first being the drastic increase in computation associated with the two sets of points. The second being that the SD method requires a significantly larger number of DOF than the DG method to reach the same level of accuracy.

3.5 Flux Reconstruction

The FR method, proposed by Huynh [36] in 2007, acts as a unifying framework for high-order methods, capable of recovering a multitude of numerical schemes, including the DG, SV, and SD methods [36, 39]. The FR method ensures a conservative scheme in addition to recovering the strong form of the solution.

The following section details the formulation of the FR method in 1D and illustrates the recovery procedure for individual numerical methods. Note that the DG method is the spatial discretization method used throughout this report and thus, only the procedure which recovers the DG method is articulated. The extension of the FR method to higher dimensions, including the formulations for all element types, is then provided, followed by a brief analysis of the implementation and efficiency of the FR method on modern hardware systems.

3.5.1 Flux Reconstruction Formulation in 1D

Consider the one dimensional conservation law of the form

$$\frac{\partial u}{\partial t} + \frac{\partial \vec{f}}{\partial x} = 0, \tag{3.1}$$

where u represents the conserved, time-dependent solution, and $\vec{f}$ is the solution flux. The FR procedure starts by discretizing the domain, Ω, into N_E non-overlapping elements, Ω_e, each containing K solution points, such that

$$\Omega = \{\Omega_e \dots \Omega_E\}, \quad E \neq \oslash, \quad \Omega_e \in [x_{e,L}, x_{e,R}], \tag{3.2}$$

as seen in Figure 3.4. For the sake of clarity, it is worth noting the first subscript denotes the element

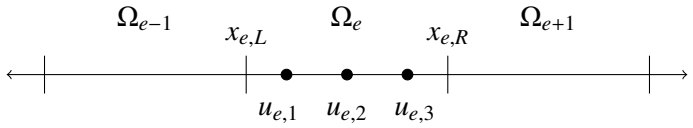

Figure 3.4. Third order one dimensional computational element

index while the second subscript refers to the nodal position within the element. Within each element, the exact solution is approximated by constructing a continuous solution polynomial, $\mathcal{U}_e^G(x,t)$, of degree $\mathcal{P} = K$-1. The solution polynomials within each element are combined to form a global piecewise polynomial approximation of the solution, $\mathcal{U}^G(x,t)$, such that

$$u(x,t) \approx \mathcal{U}^G(x,t) = \bigoplus_{e=1}^{N_E} \mathcal{U}_e^G(x,t), \tag{3.3}$$

where the continuous, element-wise solution polynomial is constructed as

$$\mathcal{U}_e^G(x,t) = \sum_{k=1}^{K} u(x_{e,k},t)\,\phi_k(x_k), \tag{3.4}$$

where $\phi_{e,k}(x_k)$ is the k^{th} order nodal basis function. The well known Lagrange polynomials are commonly used as the nodal basis functions, owing to their unique property of assuming a value of 1 at $x_{e,k}$ and a value of 0 for all other solution points. Among FE methods, it is common practice to linearly map each global element, Ω_e to a reference element, ξ, such that $\xi \in [-1,1]$. The mapping functions, which transform the global element to the reference element and vice-versa, are given as

$$\xi(x) = 2\left(\frac{x - x_{e,L}}{x_{e,R} - x_{e,L}}\right) - 1 \quad and \quad x(\xi) = \frac{1}{2}\left(x_{e,L} + x_{e,R} + \xi h_e\right), \tag{3.5}$$

respectively, where h_e is the width of the element in the global space. The mapping metric, which evaluates the performance of the mapping function, is given as

$$\frac{dx}{d\xi} = \frac{h_e}{2}. \tag{3.6}$$

The benefit of mapping to the reference space is fully realized when computing a solution of uniform polynomial order on a single element type grid, as the nodal basis functions need only be calculated once. Additionally, the uniformity of the reference space allows the same basis functions to be applied to elements of arbitrary size and orientation. With that in mind, the Lagrange polynomials are defined in the reference space as

$$\phi_{e,k}(\xi) = \prod_{s=1, s\neq k}^{K} \frac{\xi - \xi_s}{\xi_k - \xi_s}. \tag{3.7}$$

The 5^{th} order Lagrange polynomials, constructed using the Gauss points as solution points, are shown in Figure 3.5. As determined by Hesthaven [40], the chosen set of solution points used to generate the Lagrange polynomials is not unique to individual numerical methods, rather, they are chosen to improve the stability of the solution. For example, equidistant points often support the introduction of the notorious Runge phenomenon into the polynomial, which corrupts the solution and reduces stability. The Gauss points, on the other hand, minimize the effects of Runge's phenomenon and greatly improve numerical stability and accuracy. Following the procedure used to construct the global piecewise solution

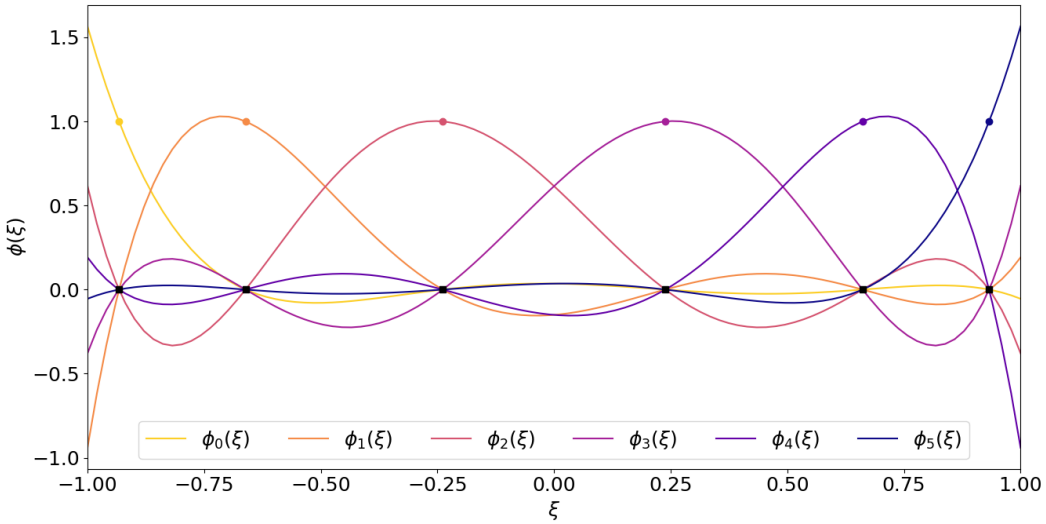

Figure 3.5. Lagrange polynomials using Gauss points for a 5^{th} order 1D element

polynomial, the global piecewise flux polynomial, $\mathcal{F}^G(x,t)$ is constructed as

$$\vec{f}(x,t) \approx \mathcal{F}^G(x,t) = \bigoplus_{e=1}^{N_E} \mathcal{F}_e^G(x,t), \tag{3.8}$$

with the continuous, element-wise flux polynomial, $\mathcal{F}_e^G(x,t)$, constructed in similar fashion to Equation 3.4. Both the global solution and flux piecewise polynomials, of degree $\mathcal{P} = K$-1, are then used to solve the conservation law,

$$\frac{\partial \mathcal{U}^G}{\partial t} + \frac{\partial \mathcal{F}^G}{\partial x} = 0. \tag{3.9}$$

Note, the condition of continuity has been enforced solely on the element-wise solution and flux polynomials. As no such restrictions have been imposed on the global solution and flux polynomials, discontinuities often occur across element interfaces. The discontinuities in the global flux polynomial yield erroneous results when computing the spatial derivative of Equation 3.9, as no information from neighboring elements is included in the derivative. To remedy this issue, Huynh [36] proposed a continuous global flux polynomial, $\mathcal{F}_c^G(x,t)$, which approximates the global flux polynomial while enforcing continuity across element interfaces. Equation 3.9 stipulates that the global flux polynomial be of the same degree as the global solution polynomial; therefore, the continuous global flux polynomial assumes a degree of $\mathcal{P}$+1. Applying the spatial derivative yields a polynomial of the same degree as the global solution polynomial. The continuous global flux polynomial is calculated by adding a correction field, ψ_e, to the existing global flux polynomial

$$\mathcal{F}_c^G(x,t) = \bigoplus_{e=1}^{N_e} \left(\mathcal{F}^G(x,t) + \psi_e\right), \tag{3.10}$$

where ψ_e is of degree $\mathcal{P}$+1 and corrects for the discontinuities in the global flux polynomial across element interfaces. Before proceeding with the derivation of the correction field, the numerical treatment of a discontinuous flux across an element interface must first be addressed.

The presence of two separate flux values along an element interface is characterized as a Riemann problem, and generally requires a Riemann solver to compute a common flux value along the interface, $f_{L,R}^C$, where L and R denote the left and right interfaces of element e, respectively. To preserve the flow of information, the common interface flux must incorporate the upwind interface flux. The choice of Riemann solver is not unique to individual numerical methods; however, the Riemann solver used to calculate the common flux value strongly dictates the error characteristics of the numerical method [40, 41]. For example, a purely upwinded Riemann solver assigns the value of the upwind interface flux

to the common flux, introducing numerical dissipation error. On the other hand, a central Riemann solver assigns an average of the two interface fluxes to the common flux value which introduces numerical dispersion error. To minimize numerical dissipation and dispersion error, a blended Riemann solver, which combines both the upwind and central flux schemes, is typically implemented. It is important to note that the viscous and inviscid fluxes associated with the NS equations are inherently dissimilar and, as such, often necessitate separate Riemann solvers. Throughout this report, the computation of inviscid interface fluxes is performed by applying a Rusanov flux [40] while the viscous interface fluxes are computed using the Bassi-Rebay II flux [42].

With the formulation of the common interface fluxes defined, the derivation of the correction field may proceed. The correction field, calculated on the reference element for simplicity and efficiency, is defined as

$$\psi_e = \left(f_L^C - \mathcal{F}^R(-1)\right) g_L(\xi) + \left(f_R^C - \mathcal{F}^R(1)\right) g_R(\xi), \tag{3.11}$$

where $\mathcal{F}^R$ is the reference flux polynomial, obtained by mapping the global flux polynomial to the reference element via Equation 3.5. The jump between the common interface flux and the value of the flux polynomial at the interface is accounted for by applying the correction functions g_L and g_R. The correction functions are chosen such that g_L corrects the flux jump at the left interface without affecting the flux values at the right interface, with g_R performing similarly on the right interface. The right Radau polynomials are chosen as the left correction functions as they assume a value of one at the left interface and zero at the right interface, as shown in Figure 3.6. The left Radau polynomials behave inversely and are thus applied as the right correction functions. The DG method is recovered by using the Radau polynomials as the correction functions.

Recall, the application of the correction field serves two purposes; to rectify any flux discontinuities across element interfaces in addition to elevating the degree of the global flux polynomial to order $\mathcal{P}$+1. To satisfy both requirements, the set of solution points used to construct the correction functions is expanded to include the upwind element interface. The inclusion of the upwind interface as a solution point enforces continuity between elements and enables the construction of the elevated $\mathcal{P}$+1 flux polynomial, as seen in Figure 3.7.

Following Equation 3.10, the construction of the continuous, elevated flux polynomial, in the reference space, is given by

$$\mathcal{F}_c^R(\xi, t) = \bigoplus_{e=1}^{N_e} \left(\mathcal{F}^R(\xi, t) + \psi_e\right). \tag{3.12}$$

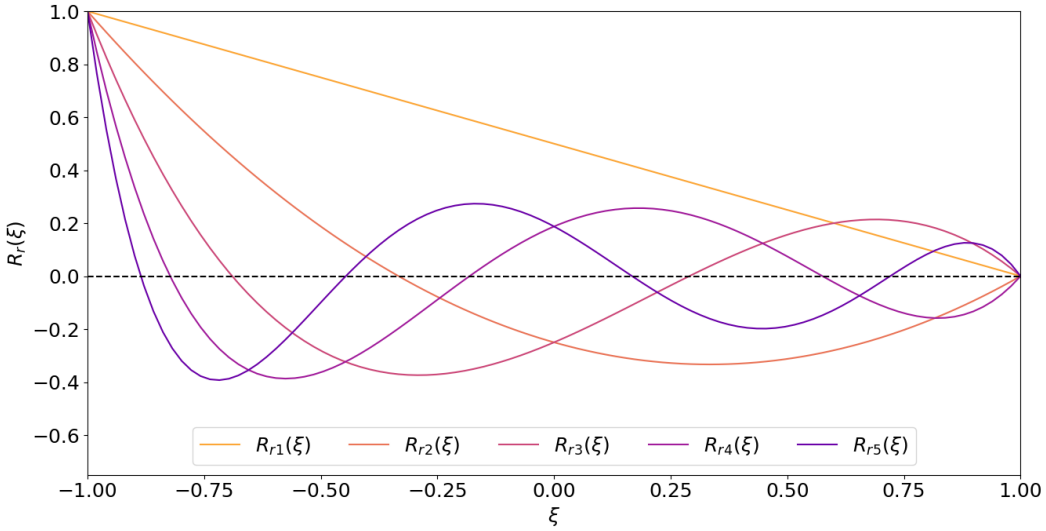

Figure 3.6. Right Radau polynomials using Radau points for a 5^{th} order 1D element

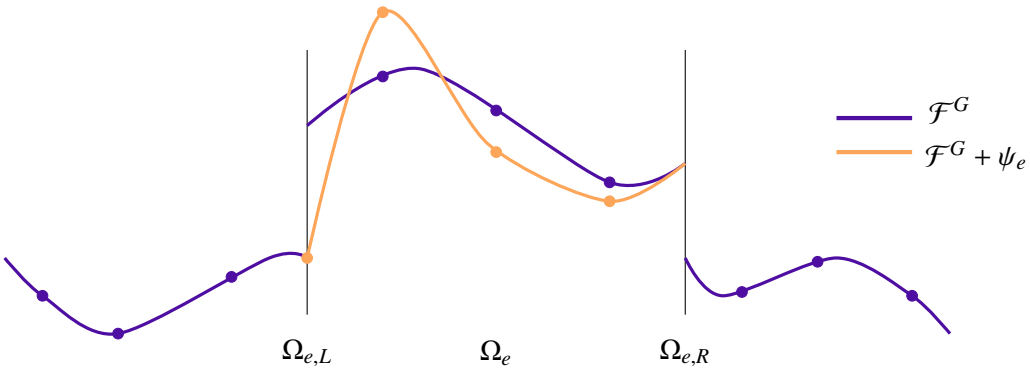

Figure 3.7. Discontinuous and continuous flux polynomials

The derivative of Equation 3.12 is computed via

$$\frac{\partial}{\partial \xi}\left(\mathcal{F}_c^R(\xi,t)\right) = \frac{\partial}{\partial \xi}\left(\mathcal{F}^R(\xi,t)\right) + \left(f_L^C - \mathcal{F}^R(-1)\right)\frac{\partial}{\partial \xi}\left(g_L(\xi)\right) + \left(f_R^C - \mathcal{F}^R(1)\right)\frac{\partial}{\partial \xi}\left(g_R(\xi)\right), \tag{3.13}$$

which provides the continuous flux polynomial, of the same degree as the continuous solution polynomial, required to solve Equation 3.9. The continuous flux polynomial is mapped back to the global space and the solution is advanced in time, using a temporal discretization, as defined in the following Chapter. The advantage of the FR method is realized by the absence of an integral in Equation 3.13, which allows the FR method to reclaim the strong form of the solution [36].

As determined by Huynh [36], the Radau polynomials provide the most accurate solution[2]; however,

[2]The most accurate solution of the polynomials tested by Huynh [36], which include the Radau, equi-distant, Lobatto, Chebyshev-Lobatto, Legendre-Lobatto, Lumped-Lobatto and Gauss polynomials.

this increased accuracy comes at the expense of numerical stability, embodied by a reduction in the maximum allowable time step size. On the other hand, the Chebyshev-Lobatto polynomials, which recover the SD method, provide lower orders of accuracy than the Radau polynomials but yield a maximum allowable time step size of roughly $\frac{3}{2}$ times that afforded by the Radau polynomials. The computation of aeroacoustics necessitates extremely accurate solutions; therefore, the paramount levels of accuracy administered by Radau polynomials outweighs the larger permissible time step sizes associated with each of the other sets of polynomials. As such, the Radau polynomials are used exclusively throughout this report.

The following section details the extension of the FR method to two and three dimensions, and includes the required derivation for each element type.

3.5.2 Extension to Multiple Dimensions

Following the 1D FR formulation, we consider the multidimensional conservation law of the form

$$\frac{\partial \vec{u}}{\partial t} + \nabla \cdot \vec{f} = 0, \tag{3.14}$$

where f_i is the solution flux in the i^{th}-direction. The domain is again discretized into N_E non-overlapping elements, Ω_e. The number of solution points, henceforth referred to as the DOF, required for 2D triangular and quadrilateral elements, as well as 3D tetrahedral, hexahedral and prismatic elements are shown in Table 3.1. The elements are again mapped to a reference space with coordinates $\xi, \eta, \zeta \in [-1, 1]$, as seen in Figure 3.8.

Dimension	Element type	DOF
2D	triangle	$(\mathcal{P}+1)(\mathcal{P}+2)/2$
	quadrilateral	$(\mathcal{P}+1)^2$
3D	tetrahedron	$(\mathcal{P}+1)(\mathcal{P}+2)(\mathcal{P}+3)/6$
	hexahedron	$(\mathcal{P}+1)^3$
	triangular prism	$(\mathcal{P}+1)^2(\mathcal{P}+2)/2$

Table 3.1. Degrees of freedom for 2D and 3D elements

The derivation of the FR procedure for quadrilateral and hexahedral elements is presented below followed by the derivation for triangular, tetrahedral and prismatic elements.

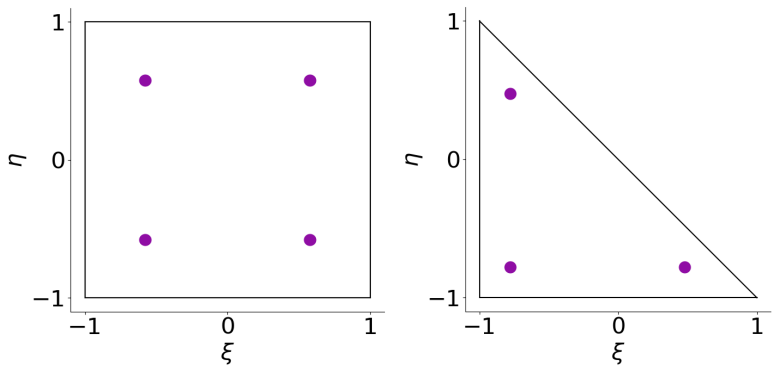

(a) $\mathcal{P}1$ reference quadrilateral (b) $\mathcal{P}1$ reference triangle

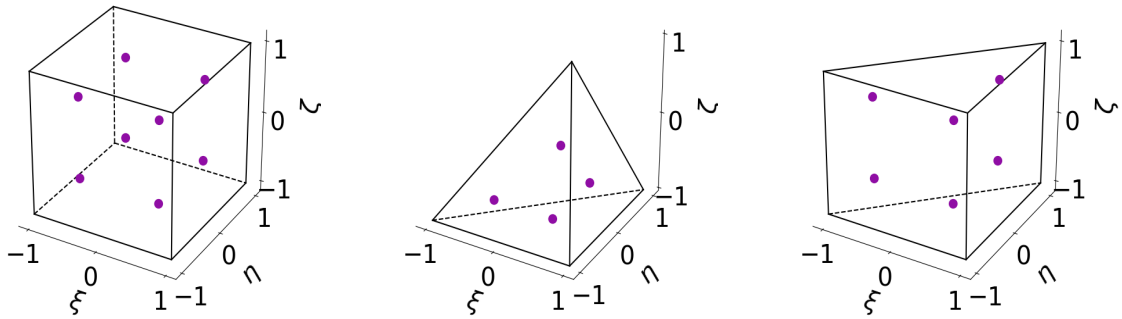

(c) $\mathcal{P}1$ reference hexahedral (d) $\mathcal{P}1$ reference tetrahedral (e) $\mathcal{P}1$ reference prism

Figure 3.8. 2D and 3D reference elements

Quadrilateral and Hexahedral Elements For simplicity, the solution points inside the reference quadrilateral element, (ξ_k, η_l $k,l=1,2,...,K$), are defined by the tensor product of the 1D Gauss points. The 2D basis function at each solution point is defined by the tensor product of the 1D Lagrange polynomials (Equation 3.7) in the ξ and η directions as,

$$\phi_{k,l} = \phi_k(\xi)\phi_l(\eta), \tag{3.15}$$

which assume a value of 1 at the solution point (ξ_k, η_l) and a value of 0 at every other solution point, as shown in Figure 3.10*a*. The continuous element-wise solution polynomial of degree $\mathcal{P} = K$-1 can then be constructed via

$$\mathcal{U}_e^G(x,t) = \sum_{k,l=1}^{K} U(x_{k,l},t)\,\phi_{e,k,l}(x,t). \tag{3.16}$$

For a constant η, the interpolation along the ξ direction reduces to a 1D problem, and vice-versa. This allows for the solution polynomial to be extrapolated to the element interfaces, providing convenient points to calculate the flux between elements, as shown in Figure 3.9. Employing an appropriate Riemann

solver at each flux point and calculating the flux at each solution point yields the necessary $K+1$ points required to construct the continuous flux polynomial of degree $\mathcal{P}$. The continuous element-wise flux polynomial is constructed in the same manner as the solution polynomial

$$\begin{aligned} \mathcal{F}_e^G(x,t) &= \sum_{k,l=1}^{K} f(x_{k,l},t)\,\phi_{k,l}(x_{k,l}), \\ \mathcal{F}_e^G(y,t) &= \sum_{k,l=1}^{K} f(y_{k,l},t)\,\phi_{k,l}(y_{k,l}). \end{aligned} \tag{3.17}$$

The continuous flux polynomial is then constructed by applying appropriate 2D correction functions to the discontinuous flux polynomial. The extension to hexahedral elements is conducted in a similar fashion.

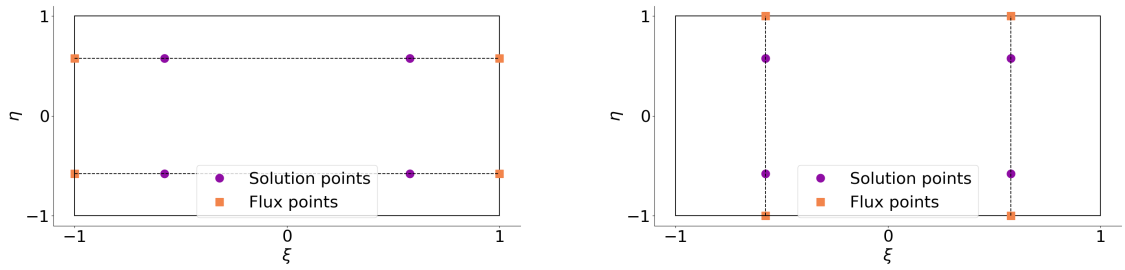

Figure 3.9. Extrapolated flux points at $\mathcal{P}1$ quadrilateral element interfaces

The solution points inside the reference hexagonal element, (ξ_k, η_l, ζ_m $k,l,m=1,2,...,K$) are defined by the tensor product of the 1D Gauss points and the 2D solution points defined above. The 3D basis function at each solution point are then defined by the tensor product of the 2D quadrilateral Lagrange polynomial and the 1D Lagrange polynomial in the ζ direction,

$$\phi_{k,l,m} = \phi_{k,l}\phi_m(\zeta). \tag{3.18}$$

The solution polynomial is constructed in the same fashion as the quadrilateral. The extrapolation of the solution polynomial to the element interfaces is again reduced to a 1D operation by considering a constant 2D plane. The continuous element-wise flux polynomials are constructed via

$$\begin{aligned} \mathcal{F}_e^G(x,t) &= \sum_{k,l,m=1}^{K} f(x_{k,l,m},t)\,\phi_{k,l,m}(x_{k,l,m}), \\ \mathcal{F}_e^G(y,t) &= \sum_{k,l,m=1}^{K} f(y_{k,l,m},t)\,\phi_{k,l,m}(y_{k,l,m}), \\ \mathcal{F}_e^G(z,t) &= \sum_{k,l,m=1}^{K} f(z_{k,l,m},t)\,\phi_{k,l,m}(z_{k,l,m}). \end{aligned} \tag{3.19}$$

The continuous flux functions are then constructed by applying appropriate 3D correction functions to the discontinuous flux polynomials.

Triangle elements Due to the asymmetrical nature of triangular elements, the tensor product of 1D Gauss points does not yield an applicable set of solution points. To address this issue, Witherden and Vincent [43] provide a comprehensive set of suitable solution points. The solution polynomial and the discontinuous flux polynomial can then be computed in similar fashion to the quadrilateral element. The reconstruction of the continuous flux function follows the lifting collocation penalty (LCP) formulation devised by Wang and Gao [44] for simplex elements. The general conservation law is re-written in the form

$$\frac{\partial \vec{u}}{\partial t} + \nabla \cdot \vec{f} + \Psi_{k,l} = 0, \tag{3.20}$$

where $\Psi_{k,l} \in \mathcal{P}$ is a scalar correction field for elements with triangular faces. Assuming straight element edges and a linear solution flux, the correction field may be computed as

$$\Psi_{e,k,l} = \frac{1}{|\Omega_e|} \sum_{\bar{f} \in \partial\Omega_e^{tri}} \sum_{l} \beta_{k,l} \hat{F}^n \left(\xi_{\bar{f},k}, \eta_{\bar{f},l} \right) S_{\bar{f}} = 0, \tag{3.21}$$

where $|\Omega_e|$ is the area of element e, $S_{\bar{f}}$ is the surface area of the element face, $\bar{f}$, $\beta_{k,l}$ are constant lifting coefficients, and $\hat{F}^n \left(\xi_{f,k}, \eta_{f,l} \right)$ is the normal interface flux jump at at the extrapolated flux points, calculated with an upwind Riemann solver.

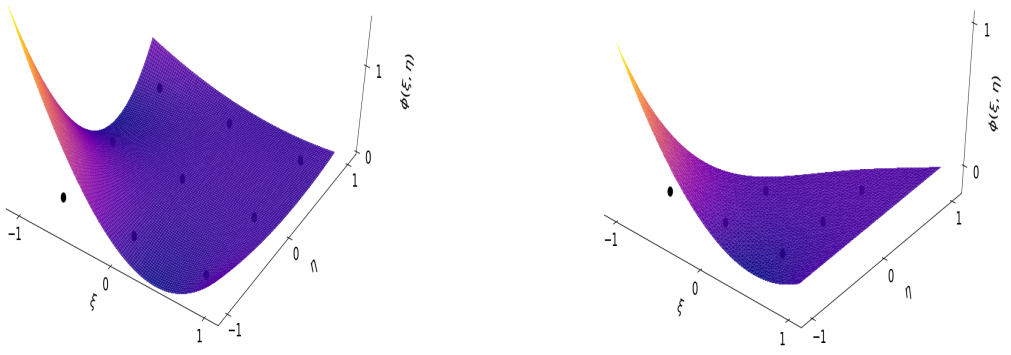

(a) $\mathcal{P}2$ quadrilateral basis function for (ξ_1, η_1) (b) $\mathcal{P}2$ triangular basis function for (ξ_1, η_1)

Figure 3.10. 2D Lagrange polynomials

Substituting Equation 3.21 into Equation 3.20 yields the continuous global flux polynomial.

Triangular Prism Elements The solution points for a prism element are given by the tensor product of the solution points of the triangular element defined above and the 1D Gauss points in the ζ-direction. The calculation of the solution and discontinuous flux polynomials are then simply the tensor product of the 2D triangular basis function, as seen in Figure 3.10, and the 1D basis functions. Along a constant ζ, flux points can easily be extrapolated to the element interfaces, as done with the quadrilateral element. The LCP formulation for a standard prism element is then given by [45]

$$\frac{\partial \vec{u}}{\partial t}+\nabla\cdot\vec{f}+\frac{1}{|\Omega_e^{tri}|}\sum_{\bar{f}\in\partial\Omega_e^{tri}}\sum_{l}\beta_{k,l}\hat{F}^n\left(\xi_{\bar{f},k},\eta_{\bar{f},l},\zeta_{\bar{f},m}\right)S_{\bar{f}}+\left[\hat{F}^n\left(\xi_k,\eta_l,-1\right)\right]g_{DG_L}\left(\zeta_m\right)+\left[\hat{F}^n\left(\xi_k,\eta_l,1\right)\right]g_{DG_R}\left(\zeta_m\right)=0, \tag{3.22}$$

where the superscript *tri* denotes the triangular element faces. Note that Equation 3.22 is a combination of Equation 3.11 and Equation 3.21. The continuous flux polynomial is obtained by taking the derivative of Equation 3.22.

Tetrahedral Elements The LCP formulation of a tetrahedron is identical to that of a triangle, simply extended to include the ζ-direction [45], as seen below

$$\frac{\partial \vec{u}}{\partial t}+\nabla\cdot\vec{f}+\frac{1}{|\Omega_e|}\sum_{\bar{f}\in\partial\Omega_{e,i}}\sum_{l}\beta_{k,l}\hat{F}^n\left(i_{\bar{f},k,l}\right)S_{\bar{f}_i}=0. \tag{3.23}$$

The continuous flux polynomial is again obtained by taking the derivative of Equation 3.23.

The following section provides a brief discussion on the performance and efficiency of the FR method while simultaneously demonstrating the inherent applicability towards modern hardware.

3.5.3 Flux Reconstruction On Modern Hardware

As the field of CAA continues to evolve, the competence of the underlying numerical methods is evaluated not only by the obtainable levels of accuracy, but also the efficient utilization of available compute resources. Historically, computer performance has been limited by the speed of the central processing unit (CPU) and as a result, early CFD codes were written to exploit the relatively high memory bandwidth rate. Advancements in computer hardware and numerical algorithms over recent decades have given rise to massively parallel CPUs, and as such, the performance of modern computers is now limited by relatively low memory bandwidth rates [27]. To maximize efficiency on modern computers, CFD codes and their underlying numerical methods must be adapted to methodically utilize the substantial

number of floating point operations per second (FLOP/s) afforded by modern CPUs. The adaptation towards economic integration on modern hardware is initiated by addressing the computational operations performed by a numerical method and their utilization of compute resources. The FR method requires three distinct computational operations, namely, elementwise operations, pointwise direct operations, and pointwise indirect operations. Elementwise operations are performed on all solution points within an element simultaneously by applying matrix mutliplies. Pointwise direct operations are again applied to every solution point within an element, but are executed on a point by point basis. Pointwise indirect operations are performed along element interfaces and are executed point by point. Both elementwise and pointwise direct operations require information exclusively located at the solution points within an element, which permits rapid, structured computations on the CPU. Pointwise indirect operations, on the other hand, require information from multiple elements, often located in separate matrices. The performance of pointwise indirect operations is thus limited by the memory bandwidth, as multiple locations in memory must be accessed before performing a calculation. For a numerical method to operate most efficiently on modern hardware, the number of elementwise and pointwise direct methods should be maximized while the number of pointwise indirect methods must be kept to a minimum. The FR method epitomizes this behavior, particularly at higher polynomial orders, as the number of internal solution points surpasses the number of points along the element interfaces. The elementwise high order framework allows the FR method to achieve roughly 55% of peak FLOP/s [34]. Conversely, the traditional FV method is dominated by pointwise indirect operations and therefore only achieves approximately 3% of peak FLOP/s [34]. The remarkably efficient operation of the FR method on modern hardware tremendously reduces the computational costs and run times of CAA simulations, thus alleviating the demand for hybrid CAA methods and enabling highly accurate computation of sound via DNS.

The following Chapter details the treatment of the temporal derivative in Equation 2.4 and summarizes the temporal discretization schemes employed throughout this report.

Chapter 4

Temporal Discretization

With the spatial derivative of Equation 2.4 accounted for in the previous Chapter, the current Chapter details the two distinct temporal discretization approaches and addresses their applicability towards CAA, followed by the derivation of the time-stepping schemes utilized in this report.

4.1 Explicit vs. Implicit Schemes

Explicit temporal discretization schemes advance the solution in time using the known solution at the current time step. The most common approach of explicit temporal discretization utilizes the explicit Runge-Kutta (RK) methods, which approximate the solution at s intermediate stages

$$u^{t_1} = u^{t_0} + \Delta t \sum_{i=0}^{s} b_i \mathcal{R}^i, \tag{4.1}$$

where u^{t_0} is the known solution at the current time step, u^{t_1} is the unknown solution at the following time step, Δt is the time step size, b_i is the weight coefficient, and $\mathcal{R}^i$ is the residual at each intermediate stage. The weights of each incremental time step are written compactly in Butcher tableaus [46], which, for explicit methods, take the shape of a lower triangular matrix with zeros along the diagonal

$$\begin{array}{c|cccc} 0 & & & & \\ c_2 & a_{21} & & & \\ c_3 & a_{31} & a_{32} & & \\ \vdots & \vdots & & \ddots & \\ c_s & a_{s1} & a_{s2} & \cdots & a_{s,s-1} \\ \hline & b_1 & b_2 & \cdots & b_s \end{array} \tag{4.2}$$

where $a_{i,j}$ is the RK matrix and c is the vector containing the time steps of the intermediate stages, represented as a fraction of the total time step. Explicit time-stepping schemes, especially the class of RK methods, are often used due to the simplicity of implementation. Additionally, the RK schemes allow for the extension to higher-orders of temporal accuracy without drastically increasing computational cost. However, the disadvantage of explicit time-stepping methods is that the maximum allowable time step size is strictly limited by the Courant-Friedrichs-Lewey (CFL) number

$$CFL = \frac{\alpha_a \Delta t}{\Delta x}. \tag{4.3}$$

With a fixed advection velocity and grid spacing, the time step must be reduced to meet the CFL criteria. Generally when using explicit time-stepping methods, the accuracy of the solution increases at the expense of the CFL limit, and vice-versa.

Implicit temporal discretization methods advance the solution in time using the unknown solution at the following time step. Similar to the explicit methods, the most common approach of implicit temporal discretization also utilizes the (implicit) RK methods, whose Butcher tableau assumes the form

$$\begin{array}{c|cccc} c_1 & a_{11} & a_{12} & \cdots & a_{1s} \\ c_2 & a_{21} & a_{22} & \cdots & a_{2s} \\ c_3 & a_{31} & a_{32} & \cdots & a_{3s} \\ \vdots & \vdots & \vdots & \ddots & \vdots \\ c_s & a_{s1} & a_{s2} & \cdots & a_{ss} \\ \hline & b_1 & b_2 & \cdots & b_s \\ & b_1* & b_2* & \cdots & b_s* \end{array} \tag{4.4}$$

where the b_s* row is used for calculating the error at each intermediate stage. Note that the implicit Butcher tableau is not a lower triangular matrix with zeros along the diagonal, creating a system of s algebraic equations that need to be solved at every iteration, which becomes computationally demanding and memory intensive as the size of the system increases. Although implicit time-stepping schemes are often considerably more computationally expensive than explicit schemes, they display unconditional stability, allowing for larger time steps compared to explicit schemes. The unconditional stability of implicit schemes is particularly advantageous for solving stiff systems, where the use of explicit schemes is typically unsuitable [40].

Although implicit schemes have proven successful in CAA applications [22, 25, 26], explicit schemes

are far more prevalent [22]. The enhanced grid resolutions required to adequately resolve the disparate array of length scales present in CAA simulations exacerbate the already increased computational costs and memory consumption issues inherent to implicit methods, effectively negating the benefits of the larger afforded time step sizes. Therefore, to minimize computational costs, explicit temporal discretization schemes were utilized exclusively throughout this report. The following sections detail the two primary explicit schemes used throughout this report, the classic RK method and the Paired Explicit Runge-Kutta (P-ERK) method.

4.2 Classic Runge-Kutta Method

The classic four stage fourth-order RK method ($RK_{4,4}$), whose Butcher tableau is given in Equation 4.5,

$$\begin{array}{c|cccc} 0 & & & & \\ \frac{1}{2} & \frac{1}{2} & & & \\ \frac{1}{2} & 0 & \frac{1}{2} & & \\ 1 & 0 & 0 & 1 & \\ \hline & \frac{1}{6} & \frac{1}{3} & \frac{1}{3} & \frac{1}{6} \end{array} \tag{4.5}$$

is extensively used throughout this report, and therefore the calculation of the intermediate stages and updated temporal solution are demonstrated in Equation 4.6.

$$\begin{aligned} stage\ 1 = &\begin{cases} u^1 &= u^t \\ \mathcal{R}^1 &= \mathcal{R}(u^1) \end{cases} \\ stage\ 2 = &\begin{cases} u^2 &= u^t + \frac{\Delta t}{2}\mathcal{R}^1 \\ \mathcal{R}^2 &= \mathcal{R}(u^2) \end{cases} \\ stage\ 3 = &\begin{cases} u^3 &= u^t + \frac{\Delta t}{2}\mathcal{R}^2 \\ \mathcal{R}^3 &= \mathcal{R}(u^3) \end{cases} \\ stage\ 4 = &\begin{cases} u^4 &= u^t + \Delta t\mathcal{R}^3 \\ \mathcal{R}^4 &= \mathcal{R}(u^4) \end{cases} \\ u^{t_1} &= u^t + \Delta t\left(\tfrac{1}{6}\mathcal{R}^1 + \tfrac{1}{3}\mathcal{R}^2 + \tfrac{1}{3}\mathcal{R}^3 + \tfrac{1}{6}\mathcal{R}^4\right) \end{aligned} \tag{4.6}$$

The $RK_{4,4}$ method is a compelling temporal discretization method, particularly for CAA, as it yields a fourth-order temporally accurate solution while minimizing memory overhead. The primary deficiency

of the $RK_{4,4}$ method, however, is the strict limitation on the maximum allowable time step size, thus, in a practical sense, restricting its application to non-stiff systems. To alleviate the restriction on the maximum allowable time step size, particularly in stiff regions of the domain, the P-ERK method, described in the following section, is implemented.

4.3 Paired Explicit Runge-Kutta Method

The P-ERK method allows RK schemes with a large number of derivative evaluations and large stability regions to be applied in stiff regions of the domain, while RK schemes with fewer derivative evaluations can be applied in less stiff regions to reduce computational costs [47]. The general butcher tableau for the P-ERK method is presented in Equation 4.7.

$$\begin{array}{c|cccccc} 0 & 0 & & & & & \\ c_2 & a_{2,1} & 0 & & & & \\ c_3 & c_3 - a_{3,2} & a_{3,2} & 0 & & & \\ c_4 & c_4 - a_{4,3} & 0 & a_{4,3} & \ddots & & \\ \vdots & \vdots & \vdots & \vdots & \ddots & 0 & \\ c_s & c_s - a_{s,s-1} & 0 & 0 & \cdots & a_{s,s-1} & 0 \\ \hline & 0 & 0 & 0 & \cdots & 0 & b_s \end{array} \tag{4.7}$$

The butcher tableau for the P-ERK method differs from that of the $RK_{4,4}$ butcher tableau in that there exists a single unknown coefficient per stage [47]. The unknown coefficients are determined from the stability polynomial, $P(z)$,

$$P(z) = \frac{det\left(I - Za + Ze_0 b^T\right)}{det\left(I - Za\right)}, \tag{4.8}$$

where Z is a point in the complex plane and e_0 is a vector of ones [47]. Note, the complete derivation of the P-ERK method is provided by Vermeire [47].

The P-ERK method is uniquely designed such that any RK schemes with the same number of stages can be paired, allowing specific RK schemes to be locally applied within the domain to accommodate any stiffness requirements [47]. This is a highly desirable feature, as the RK schemes with a large number of stages and enhanced stability regions, applied locally in the stiff regions, globally increase the maximum permissible time step. The increased time step size significantly reduces computational costs, yielding speedup factors of approximately five [47]. Although the P-ERK method considerably

reduces simulation run times, it is limited to second-order temporally accurate solutions; however, in this study, the substantial speedups afforded by the P-ERK method outweigh the benefits of the potential higher-orders of temporal accuracy provided by implicit schemes.

The following Chapter establishes the two distinct approaches of CAA and details the prevailing methods within each approach, followed by a discussion of the computational challenges associated with CAA.

Chapter 5

Computational Aeroacoustics

In 1952, Lighthill [17, 18] pioneered the field of aeroacoustics by rearranging the NS equations into an inhomogeneous wave equation depicting acoustic propagation. Lighthill's equation, applicable solely to unbounded turbulent flows, was quickly extended to include the effects of solid boundaries and trailing edges [19, 20]. The field of CAA, which applies numerical methods to analyze aerodynamically generated sound and acoustic propagation, arose in the mid-1980s when Hardin *et al.* [24] successfully computed the acoustic field of a cylinder in mean flow directly from the results of a CFD simulation. Hardin *et al.* split the acoustic calculation into two distinct steps, the first of which involved computing the time-dependent flow field using a stream function formulation to solve the incompressible 2D NS equations. The acoustic field was then computed by integrating over the flow field using a low-frequency Green's function [48]. Aided by the advancements in computing power and improvements in high order numerical methods, the CAA's scope has since drastically increased to include the computation of acoustic fields generated by exceedingly complex flow fields, including fully developed turbulence over airfoils in stall [32].

The following sections detail the prevailing CAA methods and their associated computational requirements. The Chapter is concluded with a discussion regarding the numerical challenges fundamentally inherent to the field of CAA.

5.1 Hybrid Methods

Following the methodology employed by Hardin *et al.* , traditional CAA simulations are performed using a hybrid method that splits the calculation of the acoustic field into two distinct steps. The conventional aerodynamic variables are initially computed using an appropriate CFD method, followed by

the calculation of the acoustic or perturbed variables, which require the aerodynamic variables as inputs. As discussed below, the computation of the acoustic variables is carried out either via post-processing measures or by applying a separate acoustic flow solver.

5.1.1 Acoustic Analogies

Acoustic analogies are a distinct family of hybrid methods that aim to evaluate the far-field acoustics using only the near-field aerodynamic variables. The far-field acoustics are calculated, as a post-processing measure, by rearranging the governing equations of fluid motion to establish a mathematical model resembling physical acoustic propagation. The model for the acoustic field is not based on the true physics of aerodynamically generated sound but rather the analogous representation of acoustic propagation through the governing equations. As such, acoustic analogies require highly accurate near-field CFD results to model the far-field acoustics properly.

Lighthill's acoustic analogy

Lighthill's analogy describes the acoustic field generated by turbulent structures radiating in free space [17, 18]. Note that Lighthill's acoustic analogy is exact, with respect to the original governing equations, in the sense that no approximations were made in its derivation; however, it is often convenient to represent the turbulent structures in the flow field as a distribution of source quadrupoles, thus introducing slight approximations into the analogy. Lighthill defines the density perturbations, ρ', as

$$\rho'(\mathbf{x}, t) = \frac{1}{4\pi c_0^2} \frac{\partial^2}{\partial x_i \partial x_j} \int_\Omega \frac{T_{ij}(\mathbf{y}, \check{t})}{\bar{D}} d(\mathbf{y}), \tag{5.1}$$

where $\mathbf{x}$ is the location at which the acoustic pressure is observed, $\mathbf{y}$ is the location where the acoustic pressure is generated, c_0 is the speed of sound, $\bar{D}$ is the distance between the observation and generation points, $\check{t}$ is the delayed time, defined as t - $\frac{\bar{D}}{c_0}$, and the Lighthill stress tensor, T_{ij}, which governs the strength of the acoustic quadrupoles, is given by

$$T_{ij} = \rho V_i V_j + p_{ij} - c_0^2 \rho \delta_{ij}, \tag{5.2}$$

where δ_{ij} is the Kronecker delta. Lighthill's analogy is well suited for the acoustic prediction of highly turbulent flows in free space, particularly turbulent jet noise [16, 17, 18, 22]; however, excluding the effects of solid boundaries and trailing edges prohibit the application of Lighthill's analogy towards complex, industrial CAA simulations.

Curle's acoustic analogy

Curle extended Lighthill's analogy to include the presence of solid boundaries in the generation of the acoustic field [19]. Curle showed that the inclusion of solid boundaries results in an acoustic field equivalent to a distribution of acoustic dipoles radiating in free space. The fluctuating density field is then calculated as

$$\rho'(\mathbf{x},t) = \frac{1}{4\pi c_0^2}\frac{\partial^2}{\partial x_i \partial x_j}\int_\Omega \frac{T_{ij}(\mathbf{y},\check{t})}{\bar{D}} d(\mathbf{y}) - \frac{1}{4\pi c_0^2}\int_S \frac{p_i(\mathbf{y},\check{t})}{\bar{D}} dS(\mathbf{y}), \tag{5.3}$$

where p_i is the mechanical pressure defined by Equation 2.11 multiplied by the surface normal vector pointing towards the fluid [19]. Curle's analogy is quite pertinent in the calculation of acoustics generated by wall-bounded flows, in particular, the field of duct acoustics.

Ffowcs-Williams Hawkings acoustic analogy

Ffowcs-Williams and Hawkings (FWH) further extended Lighthill's analogy to account for turbulent flow in the vicinity of a trailing edge [20]. The FWH analogy implements a control surface (CS) encompassing all sound generation mechanisms, thus truncating the volume of integration. The acoustic field along the CS is then approximated as a distribution of source monopoles, dipoles, and quadrupoles. The fluctuating density field inside and along the CS is defined as

$$\rho'(\mathbf{x},t) = \frac{1}{4\pi c_0^2}\frac{\partial^2}{\partial x_i \partial x_j}\int_\Omega \frac{T_{ij}(\mathbf{y},\check{t})}{\bar{D}} d(\mathbf{y}) - \frac{1}{4\pi c_0^2}\frac{\partial}{\partial x_i}\int_S \frac{p_i(\mathbf{y},\check{t})}{\bar{D}} dS(\mathbf{y},\check{t}) + \frac{1}{4\pi c_0^2}\frac{\partial}{\partial t}\int_{CS} \frac{Q_i}{\bar{D}} dCS(\mathbf{y}), \tag{5.4}$$

where Q_i is evaluated as

$$Q_i = \rho\left(\vec{V} + \vec{V}_\infty\right)\hat{n} - \left(\rho_\infty \vec{V}\right)\hat{n}, \tag{5.5}$$

with the ∞ subscript denoting free-stream conditions. The FWH analogy is the most commonly used acoustic analogy as it is suitable for a wide range of CAA applications, specifically configurations containing trailing edge and rotor noise [16, 25].

Amiet's acoustic analogy

Amiet's acoustic analogy is similar to the FWH analogy in that it models turbulent flow over a trailing edge; however, the CS for Amiet's analogy is taken to be the solid boundary itself. Additionally, Amiet's analogy computes the acoustic pressure as a function of frequency, ω, and the fluctuating density as a

function of time. The far-field acoustic pressure spectrum is defined by [49]

$$p'(\mathbf{x},\omega) = \left(\frac{\omega L_c \mathbf{y}}{4\pi c_0^2 (\mathbf{x}+\Gamma\mathbf{y})^2}\right)^2 l_y(\omega) d|\mathcal{L}|^2 S_{qq}(\omega,0)\,, \tag{5.6}$$

where L_c is the characteristic length of the flow field, $S_{qq}(\omega,0)$ is the spanwise cross-spectrum of surface pressure, $\Gamma = \sqrt{1-Ma^2}$, $\mathcal{L}$ is defined by

$$\mathcal{L} = \int_{L_c}^{0} g\left(\xi,\omega,\vec{V}_c\right) e^{-1\mu\xi(Ma-\mathbf{x}/(\mathbf{x}+\beta\mathbf{y}))} d\xi, \tag{5.7}$$

where $\vec{V}_c$ is the convective velocity and the function $g\left(\xi,\omega,\vec{V}_c\right)$ is a combination of Fresnel integrals defined by

$$g\left(\xi,\omega,\vec{V}_c\right) = \int_0^{\mathbf{x}} (2\pi\xi)^{\frac{-1}{2}} e^{-i\xi} d\xi, \tag{5.8}$$

and $l_y(\omega)$ is defined as

$$l_y(\omega) = \frac{1}{S_{qq}(\omega,0)} \int_0^{\infty} S_{qq}(\omega,\mathbf{y})\, dy. \tag{5.9}$$

Taking the CS as the solid boundary itself permits a highly accurate depiction of the acoustic field generated by the interaction of turbulent structures with the solid body; however, any acoustic sources not located directly on the solid boundary are neglected. As such, the accuracy of Amiet's analogy typically degrades as the distance from the solid boundary increases and free stream turbulent sound sources become more prevalent [50].

Acoustic analogies, applied as a post-processing step, use the aerodynamic quantities calculated by the applied CFD method as input to generate the radiated acoustic field. An appealing feature of acoustic analogies is that the extent to which the far-field can be extended is independent of computational cost, permitting far-field acoustic calculations at arbitrarily large distances. Furthermore, the application of a CS in the FWH analogy, which encapsulates all acoustic sources, eliminates the calculation of the computationally expensive volume integral. In addition to lowering the computational cost, the inclusion of the CS in the near-field vastly reduces the demand for stringent outflow BCs. Acoustic analogies, in particular the FWH analogy, provide an inexpensive and efficient means of calculating far-field aeroacoustics; however, the implementation of the CS is not a trivial process as the size and location of the CS are strictly problem-dependent. Additionally, the governing equations of fluid motion are not used to directly compute the acoustic field but rather a mathematical representation of the governing equations. This non-physical representation of the acoustic waves introduces multiple sources of error [51]. Firstly, acoustic analogies are highly sensitive to the choice of computational variables (i.e. p', ρ', e'), such that

different variables yield different noise source terms [51]. Secondly, acoustic analogies have been proven to identify fictitious noise sources [51], as the numerical quadrupole source terms mask the true, physical noise sources. Although acoustic analogies calculate the acoustic field with reasonable accuracy, the inability to correctly identify noise sources limits their application towards design optimization and, ultimately, noise reduction [51].

The second family of hybrid CAA methods, detailed in the following sections, adopts a more direct approach for calculating the acoustic field by applying a separate, specialized acoustic flow solver, again requiring the results of the near-field CFD simulation as input.

5.1.2 Linearized Euler Equations

The linearized Euler equations (LEE) are obtained via the decomposition of the aerodynamic variables into the mean and acoustic components [52]. The Euler equations are re-arranged to include the linear, acoustic components on the left-hand side, with the remaining non-linear components on the right-hand side treated as acoustic sources. The LEE can then be written as [52]

$$\begin{aligned}
\frac{\partial \rho'}{\partial t} + \frac{\partial \left(\rho \vec{V}\right)'}{\partial x_i} &= 0, \\
\frac{\partial \left(\rho \vec{V}_i\right)'}{\partial t} + \frac{\partial}{\partial x_i}\left(\tilde{\vec{V}}_j \left(\rho \vec{V}_i\right)' + \tilde{\vec{V}}_i \left(\rho \vec{V}_j\right)' - \rho' \tilde{\vec{V}}_i \tilde{\vec{V}}_j + p' \delta_{ij} \right) &= -\frac{\partial}{\partial x_i}\left(\rho \tilde{\vec{V}}_{i'} \tilde{\vec{V}}_{j'} - \overline{\rho \tilde{\vec{V}}_{i'} \tilde{\vec{V}}_{j'}} \right), \\
\frac{\partial (\rho e)'}{\partial t} + \frac{\partial}{\partial x_i}\left(\tilde{h} \left(\rho \vec{V}_j\right)' + \tilde{\vec{V}}_j (\rho h)' - \rho' \tilde{h} \tilde{\vec{V}}_j \right) &= -\frac{\partial}{\partial x_i}\left(\rho \tilde{h}' \tilde{\vec{V}}_j{}' - \overline{\rho \tilde{h}' \tilde{\vec{V}}_j{}'} \right),
\end{aligned} \tag{5.10}$$

where the specific energy and enthalpy, h, are defined as

$$e = c_v T, \quad h = c_p T, \tag{5.11}$$

respectively. The overbars in Equation 5.10 denote time-averaging while the tilde denotes Favre averaging, which, for V_i, is given as

$$\tilde{V}_i = \frac{\overline{\rho V_i}}{\overline{\rho}}. \tag{5.12}$$

The LEE have become an increasingly popular hybrid CAA method as they do not require an explicit volume integration, as seen in the acoustic analogies. Additionally, the framework of a traditional CFD solver contains the necessary machinery to readily solve the LEE, with some minor adjustments. Typically, the viscous NS equations are used to capture the near-field sound generation mechanisms, and the LEE are then applied in the far-field to calculate the acoustic propagation. The omission of viscous terms in

the LEE allows for inexpensive computation of the acoustic field. The drawbacks of the LEE are that an additional auxiliary variable must be solved for, which increases computation time. Additionally, the distance at which the far-field acoustic calculations can be performed is strictly limited by the grid size, which becomes prohibitively expensive at large distances.

5.1.3 Acoustic Perturbation Equations

Similar to the LEE, the acoustic perturbation equations (APE) are derived by decomposing the aerodynamic variables into their mean and fluctuating components. The unsteady, viscous compressible flow is first computed using a CFD solver in the immediate vicinity of any acoustic sources. The acoustic field is then computed on a second, larger grid using the APE [53]. Ewert *et al.* [53] derive a set of APE by filtering the right-hand side of the LEE such that only the acoustic modes are excited, the derivation of which is excluded for brevity. The complete system of APE is defined as

$$\begin{aligned} \frac{\partial p'}{\partial t} + \overline{c_0}^{-2}\nabla \cdot \left(\overline{\rho}\vec{V}^a + \overline{\vec{V}}\frac{p'}{\overline{c_0}^{-2}}\right) &= \overline{c_0}^{-2} q_c, \\ \frac{\partial \vec{V}^a}{\partial t} + \nabla \cdot \left(\overline{\vec{V}} \cdot \vec{V}^a\right) + \nabla \cdot \left(\frac{p'}{\overline{\rho}}\right) &= q_m, \end{aligned} \tag{5.13}$$

where the superscript a denotes an irrotational acoustic perturbation. The source terms of Equation 5.13 are given as

$$\begin{aligned} q_c &= -\nabla\rho \cdot \vec{V}^a + \frac{\overline{\rho}}{c_p}\frac{\overline{D}\vec{s}'}{Dt}, \\ q_m &= \nabla\phi_p + \nabla q_{\tilde{\omega}} + \mathcal{T}'\nabla\overline{\vec{s}} - \vec{s}'\nabla\overline{\mathcal{T}}, \end{aligned} \tag{5.14}$$

where $\mathcal{T}$ denotes the filtering matrix and $\vec{s}$ is a vector containing the filtered acoustic source terms exciting only the acoustic eigenmodes.

The APE provide a highly efficient means of calculating the far-field acoustics by computing the CFD and CAA equations on separate grids. By minimizing the CFD grid to the immediate vicinity of the acoustic sources, the CAA grid can be extended much further than the grid used in the LEE. Although the reduced CFD region vastly reduces computational expense, the necessity of two grids can become burdensome, particularly when dealing with complex geometries. Additionally, transferring information between the CFD and CAA grids can cause numerical instability, especially at higher Reynolds numbers [22]. Furthermore, the APE require a filtered solution, which potentially compromises the accuracy of the acoustic field.

As previously stated, all hybrid CAA methods split the computation of the acoustic field into two distinct steps. An appropriate CFD method is used to calculate the aerodynamic variables, which are then used as inputs to calculate the aeroacoustic variables separately. The direct CAA method, which calculates the aerodynamic and aeroacoustic variables concurrently, is discussed in the following section.

5.2 Direct Methods

The development of numerical methods that provide geometric flexibility and operate efficiently on modern hardware has given rise to a new family of CAA methods that aims to directly compute both the unsteady aerodynamic flow field and the corresponding acoustic field. The simultaneous calculation of the sizable aerodynamic flow features and the diminutive aeroacoustic flow features necessitates a highly accurate solution, which strongly depends on the implemented turbulence approach in addition to the applied numerical method.

The restriction on turbulence approaches is exclusive to direct CAA methods. Note, hybrid methods used in conjunction with the RANS model are capable of calculating the acoustic field, although the time-averaging of RANS could seriously compromise the accuracy of the solution. Direct methods, on the other hand, capture the generation and propagation of the time-dependent acoustic waves; therefore, the time-averaging expunges the acoustic field and invalidates the RANS model for usage in direct methods. As such, direct methods are restricted to turbulence approaches that do not utilize time-averaging, such as LES and DNS. The choice of turbulence approach incorporates several factors, including the desired level of fidelity and computational expense. The selective resolution of flow features in LES permits relatively fast computation; however, only the acoustic waves generated by the resolved flow features can be captured [32]. While more expensive, DNS resolves all flow features, thus providing the most accurate means of calculating the acoustic field. Note that the effect of modeling the unresolved flow features in LES using SGS on acoustic generation has not been determined [22, 32], and as such, DNS is applied as the turbulence approach throughout this report.

In addition to the turbulence approach, direct CAA methods are also restricted in the choice of numerical methods. As stated by Tam in a detailed review on the recent advances in CAA [21], "standard CFD schemes, designed for applications to fluid problems, are generally not adequate to compute aeroacoustics accurately and efficiently". Low order FV and FD based CFD codes severely dissipate the low amplitude acoustic waves. Additionally, as these numerical methods, particularly the FV method, operate inefficiently on modern hardware, the vast number of DOF required to adequately resolve

the acoustic generation mechanisms and the acoustic waves amplifies the computational cost beyond feasibility. Therefore, direct CAA methods are intrinsically restricted to high order numerical methods, such as the FR method.

Direct CAA methods utilize the existing framework of CFD solvers and require no additional modifications to the code base, contrary to the LEE and APE. Furthermore, as the aerodynamic and aeroacoustic variables are computed simultaneously, direct methods require considerably less post-processing than acoustic analogies. However, the extent to which the far-field can extend is severely limited, as increasing the computational domain becomes exceedingly expensive, particularly at higher polynomial orders. Consequently, direct CAA methods are currently not a suitable means of calculating far-field acoustics but offer an extremely promising method for computing near-field acoustics. The remainder of this report details the applicability and usage of the FR method for directly computing near-field acoustics.

Before verifying the FR method as a suitable direct method for near-field CAA, the underlying differences between CFD and CAA must be addressed. The following section outlines the discrepancies between CFD and CAA and details the numerical challenges fundamentally associated with CAA.

5.3 Numerical Challenges Associated with CAA

In recent years, tremendous advancements have been made in the field of CFD, particularly the development of robust high order spatial and temporal discretization schemes [21, 22, 25]. This seemingly bodes well for the field of CAA as both hybrid and direct methods utilize CFD codes to calculate the acoustic field; however, the nature of CFD and CAA simulations are inherently dissimilar, and as such, numerical methods applied in CFD are often unsuitable for CAA applications. In a review on the current status of CAA, Tam [21] details four distinct numerical challenges unique to CAA, which traditional CFD codes typically fail to satisfy, the likes of which are summarized below.

1. CAA problems are fundamentally time-dependent, while CFD problems are generally time-independent, or involve only low frequency unsteadiness.

2. Acoustic waves have very small amplitudes and propagate over extremely long distances; therefore, any CAA solver must introduce very little numerical error.

3. Numerical approximation of high-frequency waves with short wavelengths requires extremely high levels of accuracy.

4. Aerodynamic flow features tend to decay very quickly away from their source of generation while acoustic waves decay very slowly and often reach the computational boundaries, which require special treatment to ensure the acoustic field is not contaminated by spurious, non-physical reflections.

For a numerical method to be applicable for CAA, each of the above numerical challenges must be sufficiently resolved. The small amplitudes and high frequencies, characteristic of acoustic waves, present a formidable obstacle to the traditional low order CFD codes, which are intrinsically dissipative. Additionally, the DOF required to resolve both the acoustic sources and acoustic waves becomes prohibitively large for the inefficient low order numerical methods. Therefore, CAA methods, particularly direct CAA methods, necessitate the use of high order numerical schemes.

The following Chapter verifies the ability of the FR method to be applied as a direct CAA method. In addition to resolving each of the numerical challenges faced by CAA, the benefits of extending to higher-orders are demonstrated by comparing solutions using five different polynomial orders.

Chapter 6

Verification

The objective of the current Chapter is to verify the suitability of the FR method to be applied as a direct method in the computation of near-field aeroacoustics. Several verification studies are performed, each of which addresses a particular numerical challenge fundamental to CAA. Finally, the aptitude of high order solutions for CAA is examined by comparing the orders of accuracy and required DOF for several polynomial orders.

6.1 Time Dependence

Typically, the aerodynamic variables of interest in CFD simulations, such as the lift and drag on an airfoil, are independent of time and allow for the time-averaging of variables. On the contrary, all aeroacoustic variables are fundamentally time-dependent, and therefore time-averaging can not be applied.

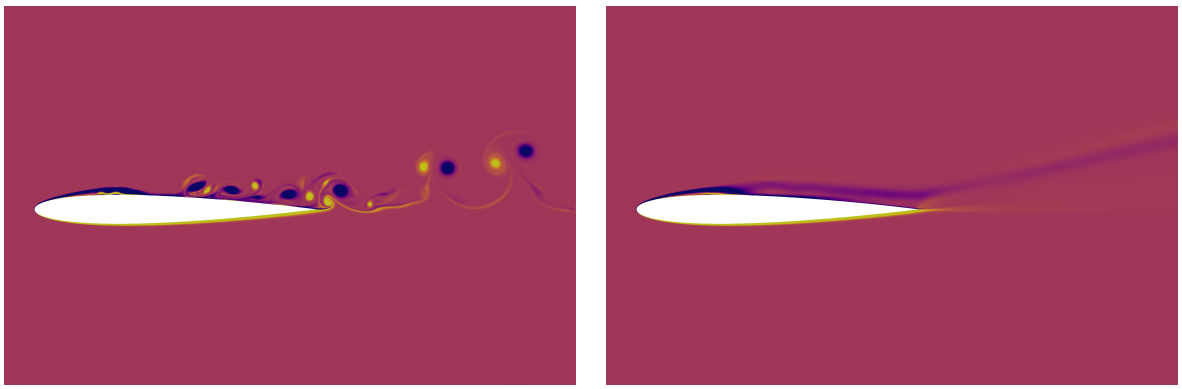

(a) Instantaneous Vorticity (b) Time-averaged Vorticity

Figure 6.1. Instantaneous and time-averaged vorticity contours of NACA0012

Figure 6.1 shows the detrimental effects of time-averaging on the development of vortices, which are the primary sources of acoustic generation for flow over an airfoil [20, 24, 25]. Figure 6.2 shows the

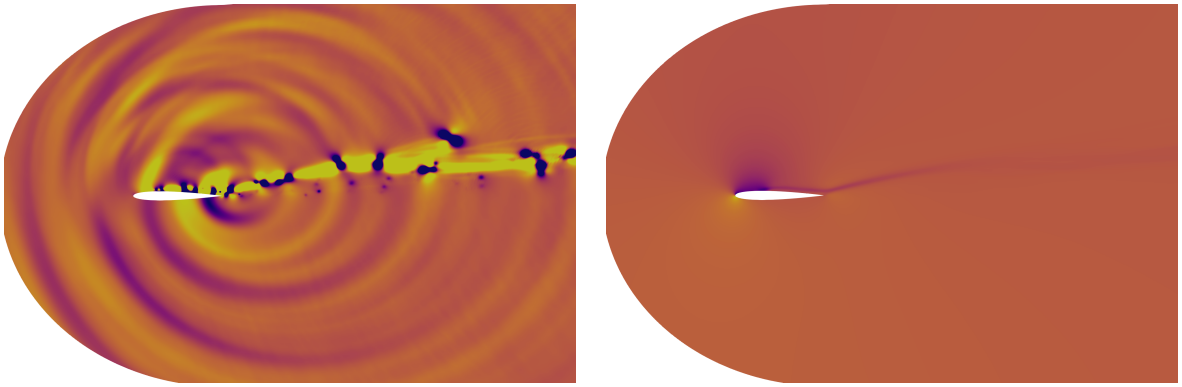

(a) Instantaneous pressure (b) Time-averaged pressure

Figure 6.2. Instantaneous and time-averaged pressure contours of NACA0012

instantaneous pressure field, with acoustic waves emanating from both the trailing edge and boundary layer reattachment zone, alongside the time-averaged pressure field, which contains no acoustic waves.

Figures 6.1 and 6.2 provide visual affirmation towards the adverse effects of time-averaging in direct CAA, thus further invalidating the use of RANS or other turbulence models that employ time-averaging.

6.2 Numerical Error

As stated in the previous Chapter, for a numerical method to be suitable for CAA, it must allow for the accurate propagation of low amplitude acoustic waves over long distances. To verify the FR method's propagative characteristics, error convergence studies were performed using the one, two, and three-dimensional linear advection equations. The linear advection equation, which describes the active transport of a passive scalar value, simulates the propagation of an acoustic wave, thus providing an inexpensive means to quantify the numerical error incurred in acoustic propagation. The impact of extending to higher-orders of accuracy is realized by comparing the $\mathcal{P}_1$-$\mathcal{P}_5$ solutions. All simulations were performed on a uniform periodic domain of length L = 20. The flow is initialized with a Gaussian pulse of the form

$$u(x,0) = \prod_{i=1}^{N_{dim}} e^{-\frac{L_i}{100}(x-x_{ic})^2}, \tag{6.1}$$

where x_{ic} is the center of the domain in the i^{th} direction. In order to simulate a large propagation distance, the simulations were run for 200 seconds with advection velocities, α_a, set to unity, corresponding to 10 complete cycles through the periodic domain, after which the error values were recorded. A numerical scheme's error is typically classified into two distinct categories, dissipation and dispersion errors [40]. The individual errors may be assessed by applying Von-Neumann analysis, as seen in the detailed report

on the FR method's error characteristics conducted by Vermeire *et al.* [39]. However, as both dissipation and dispersion errors corrupt the small-scale time-dependent acoustic waves, it is often more convenient to analyze the total error of the numerical scheme. This is done by calculating the L_2 error norm, defined as

$$\|L_2\| = \sum_{e=1}^{N_E} |u_{exact} - u_e|^2, \tag{6.2}$$

which incorporates both the numerical dissipation and dispersion errors. Note that an 8^{th} order polynomial was used in the error calculations to strengthen the quadrature. To evaluate the performance of different polynomial orders, the L_2 errors are reported for a range of grid sizes in one, two, and three dimensions, the results of which are presented in the following sections.

6.2.1 1D Results

The results of the 1D advection verification simulations are presented in Figure 6.3, the contents of which are seen in Table 6.1. As expected, on a constant grid size, the error is reduced by increasing the polynomial order, as seen in Figure 6.3*a*. Additionally, increasing the number of elements further reduces the error, albeit at different rates for each polynomial order. Huynh [36] showed that the order of accuracy, O, of a given numerical method is determined by the slope of the L_2 error as the grid is uniformly refined. Huynh [36] also demonstrated that the FR method experiences super-accuracy, where the maximum achievable order of accuracy is at least $O = \mathcal{P} + 1$. The orders of accuracy are presented in 6.1, where the bold quantities represent the maximum achievable order of accuracy for the given polynomial degree and indicate that the solution is fully converged on the mesh. The $\mathcal{P}_3$-$\mathcal{P}_5$ polynomial orders resolve the solution to machine precision, while the lower order $\mathcal{P}_1$ and $\mathcal{P}_2$ solutions cannot properly resolve the solution on the given grid sizes.

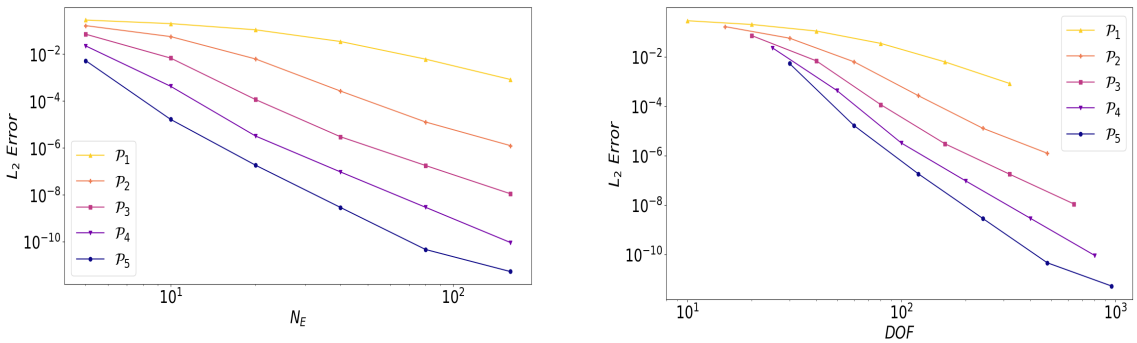

(a) L_2 Error vs. Number of Elements

(b) L_2 Error vs. Degrees of Freedom

Figure 6.3. One dimensional advection error convergence rates

$\mathcal{P}$	N_E	DOF	L_2 *Error*	O
	5	10	2.83×10^{-1}	- -
	10	20	2.00×10^{-1}	0.50
	20	40	1.09×10^{-1}	0.88
$\mathcal{P}_1$	80	10	3.45×10^{-2}	1.66
	80	160	6.14×10^{-3}	2.49
	160	320	8.31×10^{-4}	2.88
	5	15	1.64×10^{-1}	- -
	10	30	5.59×10^{-2}	1.55
	20	60	6.24×10^{-3}	3.16
$\mathcal{P}_2$	40	120	2.67×10^{-4}	4.55
	80	240	1.29×10^{-5}	4.37
	160	480	1.26×10^{-6}	3.35
	5	20	7.08×10^{-2}	- -
	10	40	6.81×10^{-3}	3.37
	20	80	1.16×10^{-4}	5.88
$\mathcal{P}_3$	40	160	3.01×10^{-6}	5.27
	80	320	1.80×10^{-7}	4.08
	160	640	8.12×10^{-9}	**4.00**
	5	25	2.26×10^{-2}	- -
	10	50	4.27×10^{-4}	5.72
	20	100	3.24×10^{-6}	7.04
$\mathcal{P}_4$	40	200	9.53×10^{-8}	5.09
	80	400	2.99×10^{-9}	**5.00**
	160	800	9.37×10^{-11}	4.99
	5	30	5.30×10^{-3}	- -
	10	60	1.66×10^{-5}	8.23
	20	120	1.85×10^{-7}	6.49
$\mathcal{P}_5$	40	240	2.89×10^{-9}	**6.00**
	80	480	4.74×10^{-11}	5.93
	160	960	5.43×10^{-12}	3.13

Table 6.1. 1D advection convergence rates

Although required for the computation of the orders of accuracy, Figure 6.3*a* offers a biased portrayal of the benefits of extending to higher-orders, as the additional computational expenses incurred with higher-order polynomials are not depicted. Figure 6.3*b* presents the error versus DOF to remedy this issue, yielding a far more equitable comparison between polynomial orders. From Table 6.1, it is evident the $\mathcal{P}_5$ polynomial provides the most accurate solution per DOF. This is a promising characteristic of extending to higher-order polynomial degrees, as more accurate solutions can be obtained using fewer DOF. It is worth noting that the steep decline in the reported order of accuracy for the $\mathcal{P}_5$ simulation is due to numerical round-off errors and is not a relic of the FR method. Additionally, as per Table 6.1, each polynomial order experiences a dramatic initial increase in the order of accuracy followed by decreasing values converging toward the expected order of accuracy. This provides a misguided representation regarding the accuracy of the polynomial order, as the rise in O is not a product of the numerical method

or polynomial degree, but rather a direct result of the Nyquist sampling limit [40]. The Nyquist sampling limit, defined as

$$\Delta x_m < \frac{1}{\lambda}, \tag{6.3}$$

dictates the minimum grid spacing required to spatially resolve a wavelength of λ. Therefore, the rise in the O is accredited to the increase in spatial resolution gained by increasing the number of elements, consequently decreasing the grid spacing. The O continues to increase alongside the number of elements until the grid spacing becomes sufficiently small so as to satisfy the Nyquist sampling limit, after which the true O of the numerical method can be properly assessed. The effect of spatial resolution on solution accuracy is clearly demonstrated in Figure 6.4, which compares the final solution for all polynomial orders computed on the coarsest grid, with the exact solution included for reference. The $\mathcal{P}_1$ solution is under resolved, thus resulting in a severely dissipated solution. As the polynomial degree increases, the corresponding grid spacing decreases, and the solution's spatial resolution is enhanced.

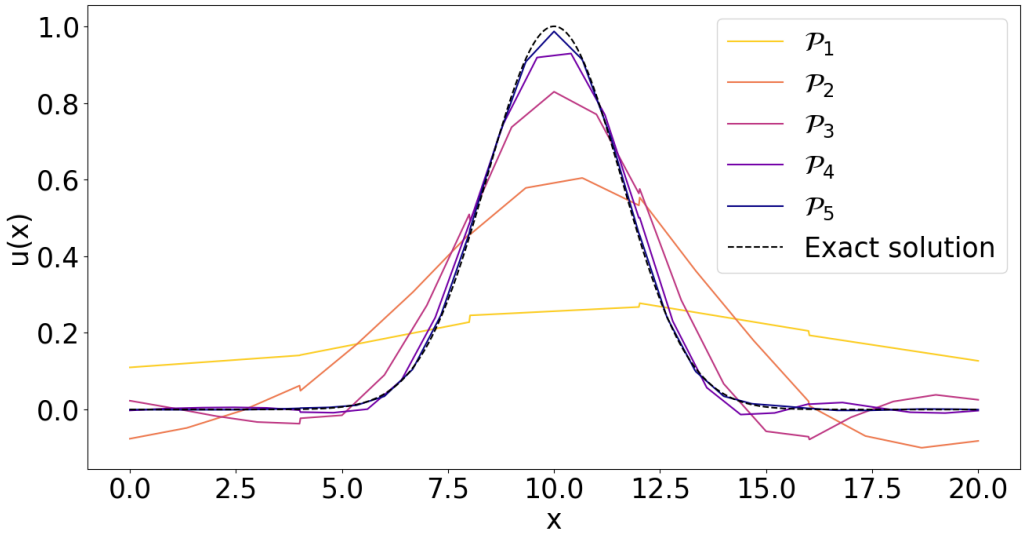

Figure 6.4. 1D spatial resolution versus solution accuracy

6.2.2 2D Results

The 2D advection verification case was performed on uniform quadrilateral meshes. To enable comparison of the accuracy and efficiency of the different polynomial orders against those reported in the 1D case, the 2D meshes were constructed such that the grid spacing in both the x and y directions be equivalent to the 1D grid spacing.

The 2D advection verification case results are presented in Figure 6.5, with the details reported in

Table 6.2. Note that the x-axis in Figure 6.5*b* displays the square root of the total DOF, yielding the DOF per direction and thus permitting direct comparison to results obtained in the previous section. As seen in the 1D advection case, the higher-order polynomials provide a more accurate solution per DOF. The benefit of higher-order polynomial solutions is unequivocally recognized as the $\mathcal{P}_5$ solution on the coarsest grid yields a smaller L_2 error value than the $\mathcal{P}_1$ solution on the most refined grid, as seen in Table 6.2. Additionally, only the higher-order $\mathcal{P}_4$ and $\mathcal{P}_5$ polynomials yield convergence to machine precision, with the $\mathcal{P}_5$ polynomial requiring roughly three times fewer DOF than the $\mathcal{P}_4$ polynomial. Note that the extension to the largest grid, containing 160^2 elements, was excluded for the sake of computational cost.

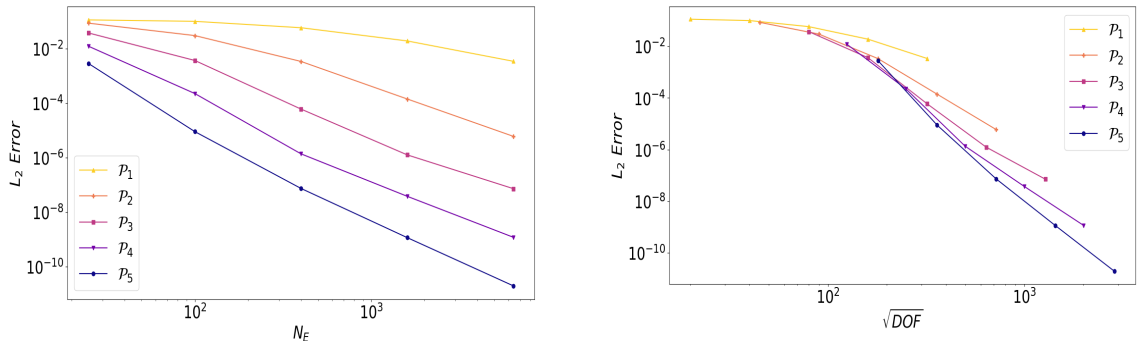

(a) L_2 Error vs. Number of Elements

(b) L_2 Error vs. Degrees of Freedom

Figure 6.5. Two-dimensional advection error convergence rates

6.2.3 3D Results

The 3D advection verification cases were performed on uniform hexahedral meshes. Again, to enable comparison of the performance of polynomial orders in multiple dimensions, the 3D meshes were constructed by applying the 1D grid spacing in the x, y, and z directions.

The results of the 3D advection verification case are presented in Figure 6.6 with the details reported in Table 6.3. The advantages of higher-order polynomial solutions are further exemplified by analyzing the results of the 3D advection case, with the $\mathcal{P}_5$ solution computed on the coarsest grid, yielding an L_2 error value roughly seven times smaller than the $\mathcal{P}_1$ solution on the most refined grid. Once again, only the $\mathcal{P}_4$ and $\mathcal{P}_5$ polynomial solutions obtain the maximum O. Similar to the previous section, the extension to the two largest grid sizes were excluded as the computational costs become prohibitively high for exceedingly large domains, especially in 3D.

$\mathcal{P}$	N_E	DOF	L_2 *Error*	O
	5^2	100	1.27×10^{-1}	- -
	10^2	400	9.90×10^{-2}	0.37
$\mathcal{P}_1$	20^2	1,600	5.78×10^{-2}	0.78
	40^2	6,400	1.89×10^{-2}	1.61
	80^2	25,600	3.38×10^{-3}	2.48
	5^2	225	8.30×10^{-2}	- -
	10^2	900	2.98×10^{-2}	1.48
$\mathcal{P}_2$	20^2	3,600	3.34×10^{-3}	3.16
	40^2	14,400	1.43×10^{-4}	4.55
	80^2	57,600	6.83×10^{-6}	4.38
	5^2	400	3.70×10^{-2}	- -
	10^2	1,600	3.63×10^{-3}	3.37
$\mathcal{P}_3$	20^2	6,400	5.96×10^{-5}	5.88
	40^2	25,600	1.24×10^{-6}	5.27
	80^2	102,400	7.15×10^{-8}	**4.07**
	5^2	625	1.20×10^{-2}	- -
	10^2	2,500	2.22×10^{-4}	5.72
$\mathcal{P}_4$	20^2	10,000	1.36×10^{-6}	7.04
	40^2	40,000	3.75×10^{-8}	5.09
	80^2	160,000	1.17×10^{-9}	**5.00**
	5^2	900	2.79×10^{-3}	- -
	10^2	3,600	8.90×10^{-6}	8.32
$\mathcal{P}_5$	20^2	14,400	7.29×10^{-8}	6.49
	40^2	57,600	1.14×10^{-9}	**6.00**
	80^2	230,400	1.93×10^{-11}	5.85

Table 6.2. 2D advection convergence rates

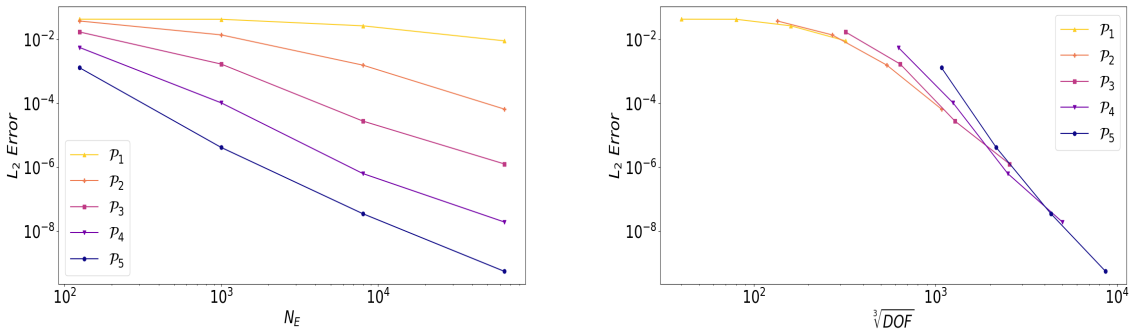

(a) L_2 Error vs. Number of Elements

(b) L_2 Error vs. Degrees of Freedom

Figure 6.6. Three dimensional advection error convergence rates

6.2.4 Discussion

The results obtained from the one, two, and three-dimensional advection verification studies substantiate the FR method's ability to accurately simulate the propagation of small amplitude waves over large distances. The attainable levels of super-accuracy establish the pertinence of the FR method in calculating

$\mathcal{P}$	N_E	DOF	L_2 *Error*	O
	5^3	1,000	4.25×10^{-2}	- -
$\mathcal{P}_1$	10^3	8,000	4.24×10^{-2}	0.01
	20^3	64,000	2.64×10^{-2}	0.68
	40^3	512,000	8.94×10^{-3}	1.56
	5^3	3,375	3.74×10^{-2}	- -
$\mathcal{P}_2$	10^3	27,000	1.37×10^{-2}	1.44
	20^3	216,000	1.55×10^{-3}	3.15
	40^3	1,728,000	6.48×10^{-5}	4.58
	5^3	8,000	1.69×10^{-2}	- -
$\mathcal{P}_3$	10^3	64,000	1.67×10^{-3}	3.34
	20^3	512,000	2.75×10^{-5}	5.93
	40^3	4,096,000	1.24×10^{-6}	4.46
	5^3	15,625	5.53×10^{-3}	- -
$\mathcal{P}_4$	10^3	125,000	1.02×10^{-4}	5.76
	20^3	1,000,000	6.23×10^{-7}	7.36
	40^3	8,000,000	1.88×10^{-8}	**5.05**
	5^3	27,000	1.28×10^{-3}	- -
$\mathcal{P}_5$	10^3	216,000	4.08×10^{-6}	8.29
	20^3	1,728,000	3.23×10^{-8}	6.9
	40^3	13,824,000	5.35×10^{-10}	**6.00**

Table 6.3. 3D advection convergence rates

acoustic propagation, as solutions of higher accuracy are obtained using fewer DOF. Furthermore, the necessity of higher-order polynomials is undeniably recognized, particularly in two and three dimensions, as the $\mathcal{P}_5$ polynomial yields L_2 errors that are orders of magnitude smaller than the $\mathcal{P}_1$ polynomial, using only a fraction of the total DOF.

Before proceeding to the following section, a few details of the error convergence studies must be addressed. First, note that only quadrilaterals and hexahedrals were used to discretize the 2D and 3D domains, respectively. Pereira [54, 55] provides a comprehensive analysis of different element types and their corresponding error tendencies and demonstrates that quadrilaterals and hexahedrals display the highest levels of accuracy per DOF, thus manifesting themselves as the ideal element types for acoustic propagation. Secondly, while the spatial discretization scheme strongly dictates the L_2 error values, as seen above, the temporal discretization method also has a significant impact on the numerical error. To minimize the temporal scheme's influence on the L_2 errors, the solution was temporally advanced using the four stage fourth-order RK method described in Chapter 4. Furthermore, temporal convergence studies were performed by reducing the Δt values on a constant grid spacing and comparing the corresponding L_2 error values. The time step size applied throughout this section was chosen such that on a constant grid, reducing the time step further resulted in negligible changes to the L_2 error, indicating temporal convergence. Table 6.4 summarizes the results of the temporal convergence study performed in 1D for

the $\mathcal{P}_5$ solution computed with 20 elements. Note that the time step of 0.0625 seconds is the smallest time step that satisfies the CFL criteria, and increasing the time step results in an unstable system. Additionally, reducing the time step size further is futile as the differences in the L_2 error begin to approach the limits of double precision.

$N_{iterations}$	Δt	L_2 *Error*	*% Change* L_2 *Error*
3200	0.0625	$5.23744548757339 \times 10^{-6}$	- -
6400	0.03125	$3.7537269867266 \times 10^{-7}$	9.28×10^{-1}
12800	0.015625	$1.86084500529387 \times 10^{-7}$	5.04×10^{-1}
25600	0.0078125	$1.85035178065841 \times 10^{-7}$	5.64×10^{-3}
51200	0.00390625	$1.85035791103158 \times 10^{-7}$	3.31×10^{-6}
102400	0.001953125	$1.85036100468104 \times 10^{-7}$	1.67×10^{-6}
204800	0.0009765625	$1.85036121422954 \times 10^{-7}$	1.13×10^{-7}
409600	0.000048828125	$1.85036122624245 \times 10^{-7}$	6.49×10^{-9}
819200	0.0000244140625	$1.85036122787862 \times 10^{-7}$	8.84×10^{-10}

Table 6.4. 1D grid with 20 elements $\mathcal{P}_5$ temporal convergence study

The following section addresses the third numerical challenge associated with CAA by detailing the FR method's ability to accurately resolve high-frequency waves with short wavelengths.

6.3 High-Frequency Resolution

Compact, high-frequency waves often characterize acoustic fields . The accurate numerical representation of these high-frequency waves poses a daunting challenge as the required grid spacing to adequately resolve the wave becomes exceedingly small, thus necessitating an impractically large number of elements. To verify the FR method's ability to adequately and efficiently resolve such high-frequency waves, error convergence studies on the advection of a Gaussian pulse, superimposed with a high-frequency sinusoidal component, are conducted. The initial conditions of the simulations are given by Equation 6.4,

$$u\left(x,0\right) = \left(2 + \cos\left(1.7\left(x - x_{ic}\right)\right)\right) e^{-\frac{ln(2)}{\left(\frac{x-x_{ic}}{10}\right)^2}}, \tag{6.4}$$

which is visualized in Figure 6.7. Noting from the previous section that the FR method displays similar advective properties across all spatial dimensions, the error convergence studies of the high-frequency Gaussian pulse are conducted on a uniform 1D periodic grid of length L = 200, to reduce computational costs. The simulations were run for 400 seconds, corresponding to two complete cycles through the domain, before calculating the L_2 errors. In addition to testing the FR method's capacity to resolve high-frequency waves, the large simulation length provides additional verification towards the ability of

the FR method to accurately propagate acoustic waves over long distances.

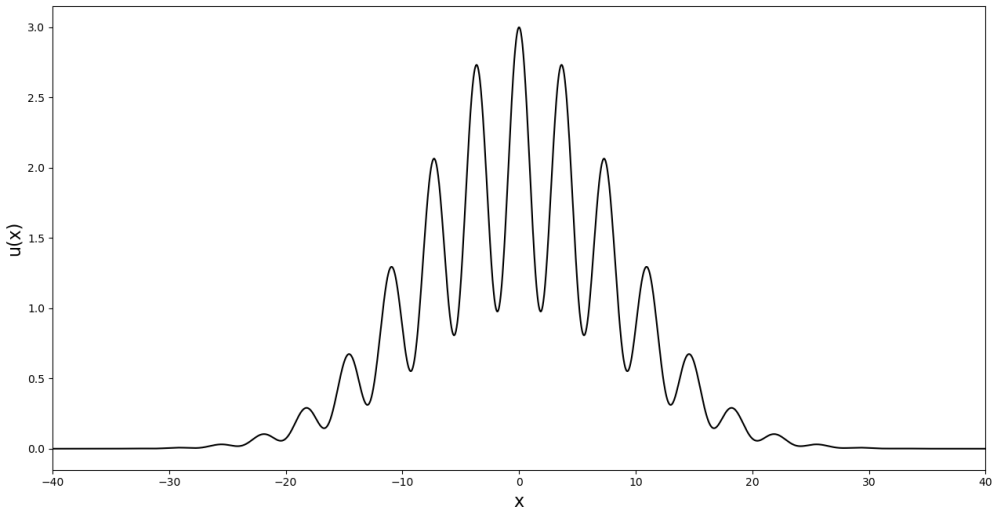

Figure 6.7. High-frequency wave initial conditions

6.3.1 Results

The error convergence studies are performed in a similar fashion to those in the previous section by reporting the L_2 error for each gird spacing and polynomial degree; however, to illustrate the proficiency of higher-order polynomials, the number of elements was increased until the solution fully converged for each polynomial order. The results of the error convergence studies are shown in Figure 6.8, with the details reported in Table 6.5. From Figure 6.8, the ineptitude of low order polynomials to resolve high-frequency waves is fully recognized, as the converged $\mathcal{P}_1$ solution requires significantly more DOF than the $\mathcal{P}_5$ solution while still yielding a larger L_2 error value.

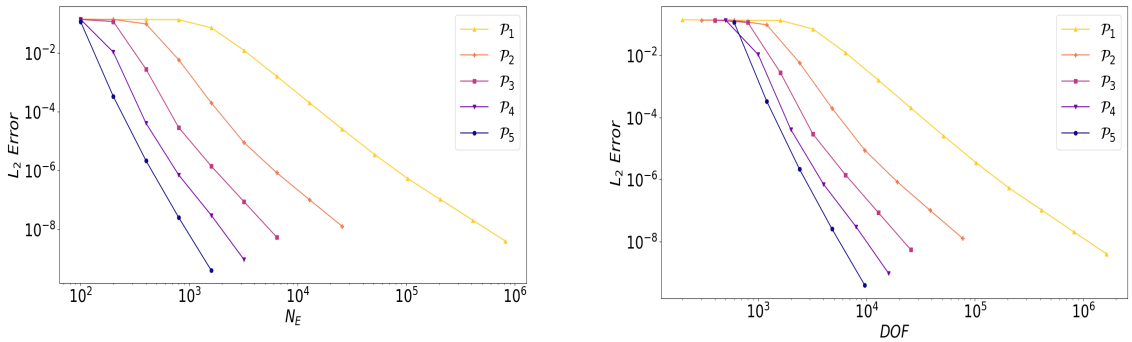

(a) L_2 Error vs. Number of Elements

(b) L_2 Error vs. Degrees of Freedom

Figure 6.8. High-frequency wave error convergence rates

$\mathcal{P}$	N_E	DOF	L_2 *Error*	O
	100	200	1.41×10^{-1}	- -
	200	400	1.37×10^{-1}	0.03
	400	800	1.36×10^{-1}	0.01
	800	1,600	1.34×10^{-1}	0.02
	1,600	3,200	7.09×10^{-2}	0.92
	3,200	6,400	1.22×10^{-2}	2.93
	6,400	12,800	1.60×10^{-3}	2.99
$\mathcal{P}_1$	12,800	25,600	2.02×10^{-4}	2.97
	25,600	51,200	2.58×10^{-5}	2.89
	51,200	102,400	3.47×10^{-6}	2.68
	102,400	204,800	5.40×10^{-7}	2.36
	204,800	409,600	1.05×10^{-7}	2.36
	409,600	819,200	2.41×10^{-8}	2.12
	819,200	1,638,400	6.02×10^{-9}	**2.00**
	100	300	1.37×10^{-1}	- -
	200	600	1.36×10^{-1}	0.01
	400	1,200	9.67×10^{-2}	0.50
	800	2,400	5.86×10^{-3}	4.04
$\mathcal{P}_2$	1,600	4,800	1.99×10^{-4}	4.88
	3,200	9,600	8.91×10^{-6}	4.48
	6,400	19,200	8.39×10^{-7}	3.41
	12,800	38,400	1.02×10^{-7}	3.04
	25,600	76,800	1.28×10^{-8}	**3.00**
	100	400	1.37×10^{-1}	- -
	200	800	1.16×10^{-1}	0.24
	400	1,600	2.80×10^{-3}	5.37
$\mathcal{P}_3$	800	3,200	2.90×10^{-5}	6.59
	1,600	6,400	1.40×10^{-6}	4.37
	3,200	12,800	8.67×10^{-8}	4.01
	6,400	25,600	5.42×10^{-9}	**4.00**
	100	500	1.37×10^{-1}	- -
	200	1,000	1.06×10^{-2}	3.69
$\mathcal{P}_4$	400	2,000	4.07×10^{-5}	8.02
	800	4,000	7.09×10^{-7}	5.84
	1,600	8,000	2.98×10^{-8}	4.57
	3,200	16,000	9.31×10^{-10}	**5.00**
	100	600	1.15×10^{-1}	- -
	200	1,200	3.30×10^{-4}	8.44
$\mathcal{P}_5$	400	2,400	2.17×10^{-6}	7.25
	800	4,800	2.53×10^{-8}	6.42
	1,600	9,600	3.95×10^{-10}	**6.00**

Table 6.5. high-frequency wave error convergence rates

6.3.2 Discussion

The efficacy of higher-order polynomials is realized by comparing the $\mathcal{P}_1$ and $\mathcal{P}_5$ solutions. The $\mathcal{P}_1$ solution requires roughly 171 times as many DOF to fully resolve the high-frequency wave to machine

precision as required by the $\mathcal{P}_5$ solution. Furthermore, the finest $\mathcal{P}_5$ solution yields an L_2 error roughly six orders of magnitude smaller than the $\mathcal{P}_1$ solution using the same DOF. The slow convergence rates and the larger L_2 error values suggest that typical, low order CFD methods are generally inapplicable for the computation of high-frequency waves associated with aeroacoustics; therefore, attention must be refocused on higher-order methods to be used as direct CAA methods. The next section addresses the fourth numerical challenge associated with CAA by discussing the importance of NRBCs and assessing the viability of the Riemann invariant BCs in conjunction with the FR method for direct acoustic computation.

6.4 Boundary Conditions

As previously stated, the computational domains used in direct CAA methods must extend far beyond the near-field region, where acoustic sources are generated, to permit the calculation of far-field acoustics. This imposes a computational challenge, as infinitely large domains can not be calculated and therefore must be truncated. The truncation of the computational domain creates a non-physical BC, which requires special numerical treatment to prevent any non-physical reflections from entering the flow and contaminating the acoustic field. Gill *et al.* [56] provide a detailed review of effective BCs for hybrid CAA methods, including but not limited to the Perfectly Matched Layer BC, the Sommerfield BC, the characteristic BC, and the asymptotic BC. These methods have proven effective for hybrid CAA methods as they are typically constructed via the LEE or APE equations and are accordingly well suited to allow for the smooth, non-reflective passage of acoustic waves. Generally, BCs derived for hybrid CAA methods are largely inept when applied to direct CAA methods, as the flow encountering the BC is no longer comprised solely of acoustic waves. To the best of the author's knowledge, a general perfectly non-reflecting BC for direct CAA methods does not exist, and therefore the BCs developed for CFD simulations must be employed, often combined with a so-called "buffer zone" [57], as described in the following section, which specifies the BCs used throughout this report and details several buffer zone techniques and their applicability as direct CAA boundary treatments.

6.4.1 Riemann Invariant Boundary Conditions

The Riemann invariant BCs are widely used in CFD due to their generality and ease of implementation. The Riemann invariants were developed initially for the 1D Euler equations and have been extended to include the 3D NS equations [58]. Assuming that the free stream velocity is subsonic, the Riemann

invariants corresponding to the incoming and outgoing characteristic waves, $\mathcal{W}^-$ and $\mathcal{W}^+$, respectively, are

$$\begin{aligned} \mathcal{W}_\infty^- &= \hat{\vec{V}}_\infty - \frac{2c_{0\infty}}{\gamma - 1}, \\ \mathcal{W}_e^+ &= \hat{\vec{V}}_e - \frac{2c_{0e}}{\gamma - 1}, \end{aligned} \tag{6.5}$$

where the subscript ∞ denotes the free stream values, the subscript e denotes the values inside the boundary element, and c_0 is speed of sound [58]. Note that supersonic flow requires alternative Riemann invariants; however, the current report only investigates acoustics at subsonic speeds, and therefore the supersonic Riemann invariants are omitted. The Riemann invariants are combined to give the normal boundary velocity, $\hat{\vec{V}}_B$, and the normal speed of sound at the boundary, $\hat{c_0}_B$, as

$$\begin{aligned} \hat{\vec{V}}_B &= \frac{1}{2}\left(\mathcal{W}_e^+ + \mathcal{W}_\infty^-\right), \\ \hat{c_0}_B &= \frac{\gamma - 1}{4}\left(\mathcal{W}_e^+ + \mathcal{W}_\infty^-\right). \end{aligned} \tag{6.6}$$

If $\hat{\vec{V}}_B$ is positive, then the flow is exiting the domain, and the entropy along the boundary, $\mathcal{S}_B$, is extrapolated from the values inside the boundary element, which is used to update the values of density and pressure along the boundary. On the other hand, if $\hat{\vec{V}}_B$ is negative, then the flow is entering the domain, and the free stream entropy value is used to update the BCs [58]. The entropy along the boundary is computed via Equation 6.7

$$\mathcal{S}_B = \frac{{c_0}_{e/\infty}^2}{\gamma \rho_{e/\infty}^{\gamma-1}}, \tag{6.7}$$

where the free stream or boundary element values are again chosen depending on the sign of $\hat{\vec{V}}_B$ [57]. The density and pressure along the boundary are calculated via

$$\begin{aligned} \rho_B &= \left(\frac{{c_0}_B^2}{\gamma \mathcal{S}_B}\right)^{\frac{1}{\gamma-1}}, \\ p_B &= \frac{\rho_B {c_0}_B^2}{\gamma}. \end{aligned} \tag{6.8}$$

The Riemann invariant BCs are most effective when considering laminar flow, as $\hat{\vec{V}}_B$ approximates $\vec{V}_B$ very closely, allowing the incoming characteristic waves to enter the domain and the outgoing characteristic waves to exit the domain at the correct speeds. This makes the Riemann invariant BCs well suited for inflow and far-field boundaries, which generally do not experience large velocity fluctuations. The outflow

boundary, however, is often subjected to the passage of highly vortical structures, particularly as the flow transitions into turbulence. Vortices of sufficient strength can alter the magnitude and direction of $\hat{\vec{V}}_B$ at the outflow, resulting in the generation of non-physical waves propagating upstream, as seen in Figure 6.9.

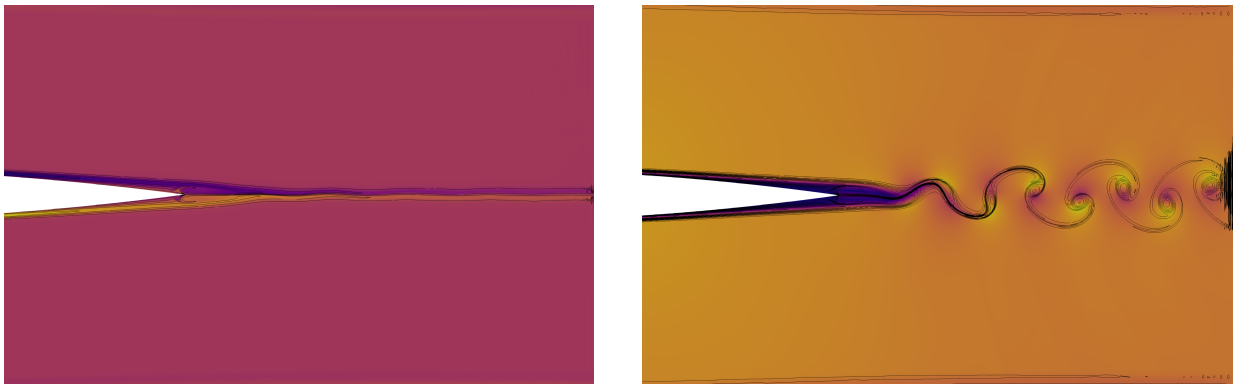

(a) Velocity profiles with vorticity contours in range [-1,1]

(b) Acoustic pressure profiles in range [-0.001,0.001]

Figure 6.9. Riemann invariant boundary condition performance

The following sections detail various methods used to reduce the strength of outgoing vortices and mitigate the generation of these non-physical waves.

6.4.2 Boundary Treatment Methods

The current section details four methods used to damp vortical structures before exiting the domain, namely, increasing the domain size, adding a sponge zone, reducing the polynomial order, and introducing artificial viscosity. To test the effectiveness of the proposed damping methods, the advection of an

isentropic vortex with initial conditions

$$
\begin{aligned}
\Upsilon &= \frac{1 - x_c^2 - y_c^2}{2R^2}, \\
\rho &= \left[1 - \frac{\left(S_v{}^2 Ma^2 \left(\gamma - 1\right) e^{2\Upsilon}\right)}{8\pi^2}\right]^{\left(\frac{1}{\gamma - 1}\right)}, \\
V_i &= \frac{S_v y_c e^{\Upsilon}}{2\pi R}, \quad V_j = 1 - \frac{S_v x_c e^{\Upsilon}}{2\pi R}, \quad V_k = 0, \\
p &= \frac{\rho^{\gamma}}{\gamma Ma^2}, \\
e &= \frac{p}{\rho\left(\gamma - 1\right)} + 0.5\left(V_i{}^2 + V_j{}^2 + V_k{}^2\right),
\end{aligned}
\tag{6.9}
$$

where $S_v = 13.5$ is the vortex strength and $R = 1.5$ is the vortex radius, is computed using the Euler equations. For all simulations, the vortex was temporally advanced using $RK_{4,4}$ method, described in Chapter 4. The isentropic vortex is an ideal verification case as the analytical solution can be computed at any given time, yielding a quantitative metric for comparing each method's performance.

Domain Size

The most primitive method of damping vortices relies solely on the dissipative properties of the numerical method. With each time step, an incremental amount of error gets introduced into the solution, and as time progresses, the error accumulates and can become large enough to diminish flow features. To test the FR method's damping properties, the simulation of the isentropic vortex was run for 1000 convective time steps, t_c, recording the L_2 error in increments of 50 t_c. The simulations were performed using polynomial orders $\mathcal{P}_1$-$\mathcal{P}_5$ on a uniform square domain of length L = 25 with periodic boundaries. The periodic boundaries allow for large simulation times while minimizing the number of elements, thus reducing the computational expense. With a domain of length 25, 50 t_c corresponds to 2 complete cycles of the vortex through the domain. To give a fair comparison between polynomial orders, the number of elements for each polynomial order was adjusted to yield a constant DOF per simulation, as seen in Table 6.6.

$\mathcal{P}$	N_E	DOF
1	120^2	57600
2	80^2	57600
3	60^2	57600
4	48^2	57600
5	40^2	57600

Table 6.6. Number of elements for domain size simulations

The results of the simulations are shown in Figure 6.10, where the L_2 error is plotted against the

simulated domain lengths. It is worth noting that although the L_2 error does not directly measure the dissipation of the numerical method, as illustrated in the previous section, the FR method produces very little dispersion error. Therefore, the L_2 error is a good representation of the dissipation error. For all polynomial orders, the L_2 error increases with increasing domain length. Additionally, the L_2 error increases as the polynomial order decreases. The $\mathcal{P}_1$ solution yields a nearly linear relationship between the L_2 error and the domain length; however, as the polynomial order increases, the aforementioned linearity diminishes.

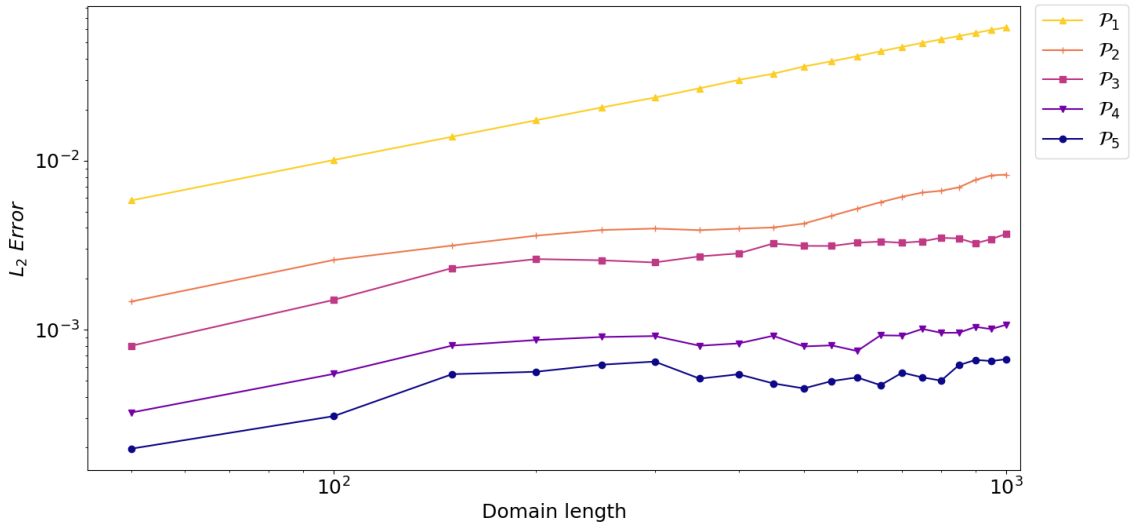

Figure 6.10. L_2 Error vs. Domain size

As seen in Figure 6.11, the $\mathcal{P}_1$ solution results in a noticeable reduction of vorticity, while the higher-order $\mathcal{P}_5$ solution experiences almost no reduction of vorticity. For practical applications, the benefit of reducing the amplitude of the vortex by increasing the domain length is outweighed by the increase in computational cost, especially at higher $\mathcal{P}$ values. Therefore, solely increasing the domain length is not a viable boundary treatment method.

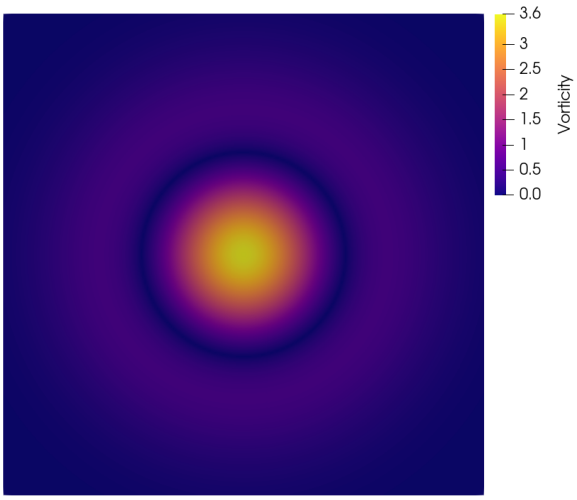

(a) Exact Solution

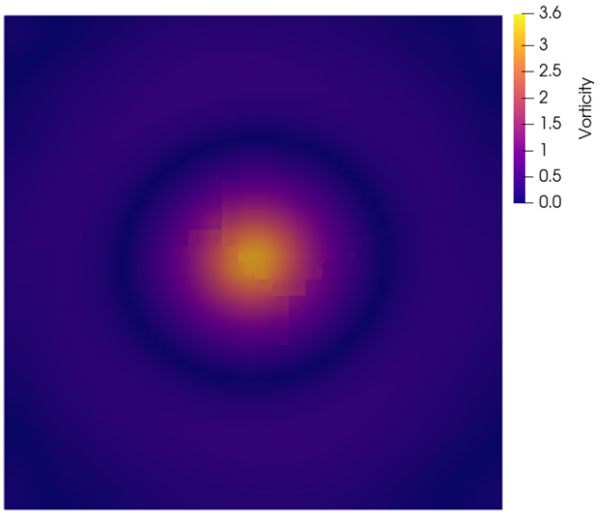

(b) $\mathcal{P}_1$ solution at 1000 t_c^*

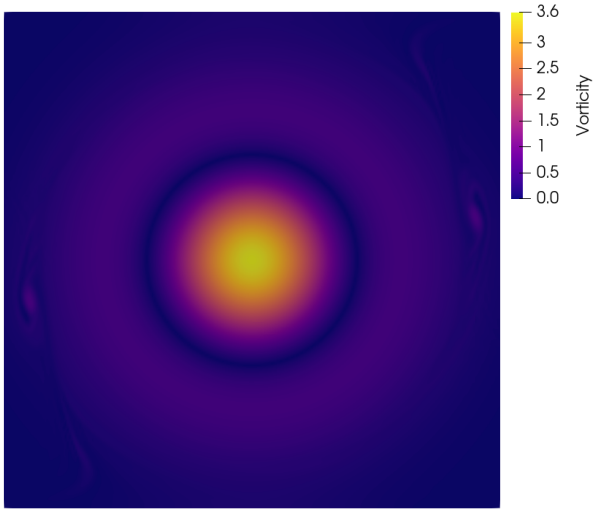

(c) $\mathcal{P}_5$ solution at 1000 t_c^*

Figure 6.11. Isentropic vortex vorticity contours in range [0,3.5]

Sponge Zone

In the previous section, the simulations of an isentropic vortex were performed on a uniform grid. This section details the advection and dissipation of an isentropic vortex on a non-uniform grid. The application of a non-uniform, or stretched, grid, particularly near the edge of the computational domain, is typically referred to as a "sponge zone" [57]. The ideology behind implementing a sponge zone is to under resolve vortices, therefore adding artificial dissipation to the existing numerical dissipation. Note that severely under resolved outgoing vortices can result in a non-physical solution, and therefore it is common practice to implement the stretched grid within a "buffer zone" [50, 57, 59]. The buffer zone is typically located beyond the region where data measurements occur, thus allowing the presence of non-physical solutions.

To enable maximum reduction of outgoing vortices, the stretching ratio is applied in the direction of fluid motion, as shown in Figure 6.12. The application and implementation of buffer zones are discussed in further detail in the following Chapter.

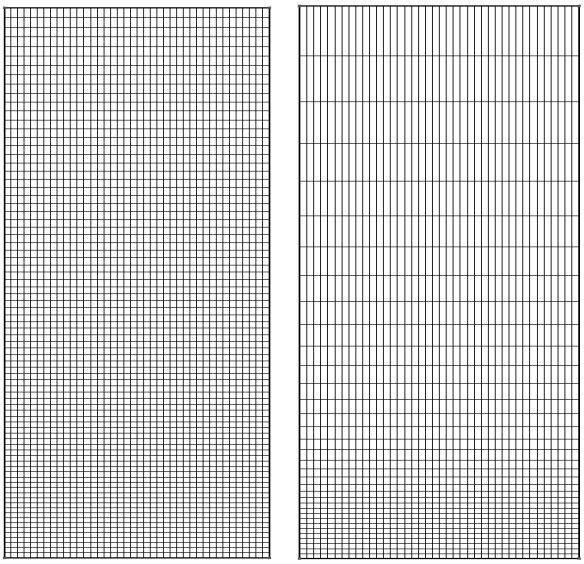

(a) Stretching ratio 1.01 (b) Stretching ratio 1.1

Figure 6.12. Stretched grid for isentropic vortex

The simulations, performed on non-uniform grids of width, W_d, = 25 and length L = 110, were run for 100 t_c before recording the error values. The grids were stretched by applying stretching ratios ranging from 1.01 to 1.1, with an interval of 0.1. For all polynomial degrees, increasing the stretching ratio yielded a reduction in vorticity, as shown in Figure 6.13, which plots the final results of the $\mathcal{P}_5$ simulations with stretching ratios of 1.01, 1.05, and 1.1. The stretching ratio of 1.01 provided a negligible reduction of vorticity, while the maximum stretching ratio of 1.1 vastly reduced the vorticity and almost completely diminished the vortex. Although the objective of a sponge zone is to eliminate vortices before encountering the computational boundaries, applying substantial stretching ratios severely under-resolves the system and disperses information, as demonstrated by Figure 6.13*c*. The stretching ratio of 1.05, however, provided an optimal balance between the stretching ratios of 1.01 and 1.1 by introducing significantly more dissipation than the stretching ratio of 1.01 while minimizing the dispersion error, as compared to the stretching ratio of 1.1.

Applying a stretching ratio to the mesh increases the element sizes, thus reducing the total number of elements on a fixed length domain. While the reduced element count decreases the computational cost, it also prohibits an equitable comparison of the L_2 error, as the total DOF is not constant for each polynomial degree. To alleviate this issue, the amplitude of the maximum and average pressure oscillations throughout

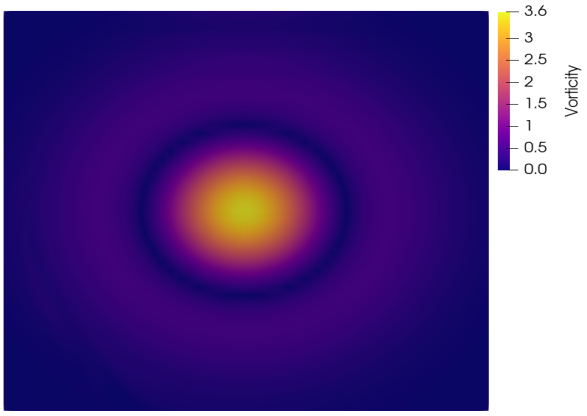

(a) SR = 1.01

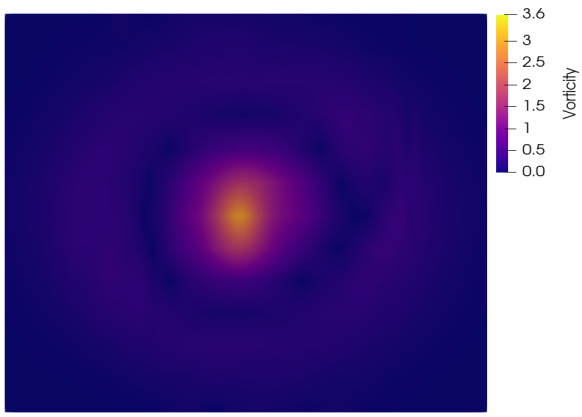

(b) SR = 1.05

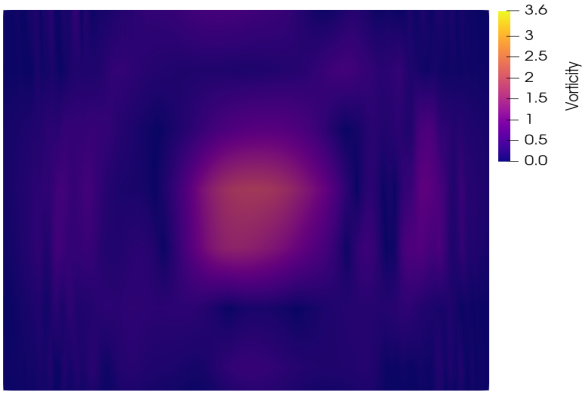

(c) SR = 1.1

Figure 6.13. $\mathcal{P}_5$ Isentropic vortex on stretched grid

the domain were recorded, as shown in Figure 6.14. For a stretching ratio to be most effective, it should maximize vorticity reduction while minimizing spurious pressure oscillations. At lower stretching ratios, the high order polynomials proved more accurate than the low order polynomials, producing spurious oscillations with smaller amplitudes. However, as the stretching ratios were increased, thus decreasing the grid resolution, the high order polynomials produced significantly larger spurious oscillations than the low order polynomials. Note, the grid resolution afforded by the low order polynomials is insufficiently large to adequately resolve the vortex, even at the smallest stretching ratios; therefore, increasing the stretching ratio had little effect on the spurious pressure oscillations.

The application of a sponge zone is a powerful boundary treatment method, as large stretching ratios can completely diminish outgoing vortices; however, caution must be exercised, as large stretching ratios are liable to create spurious reflections, potentially contaminating the acoustic field. Selecting an optimal stretching ratio is not a trivial task, as the size of the sponge zone and intensity of the outgoing vortices must be taken into consideration; nonetheless, the stretching ratios applied throughout this thesis are kept

below 1.05 to ensure minimal spurious reflections.

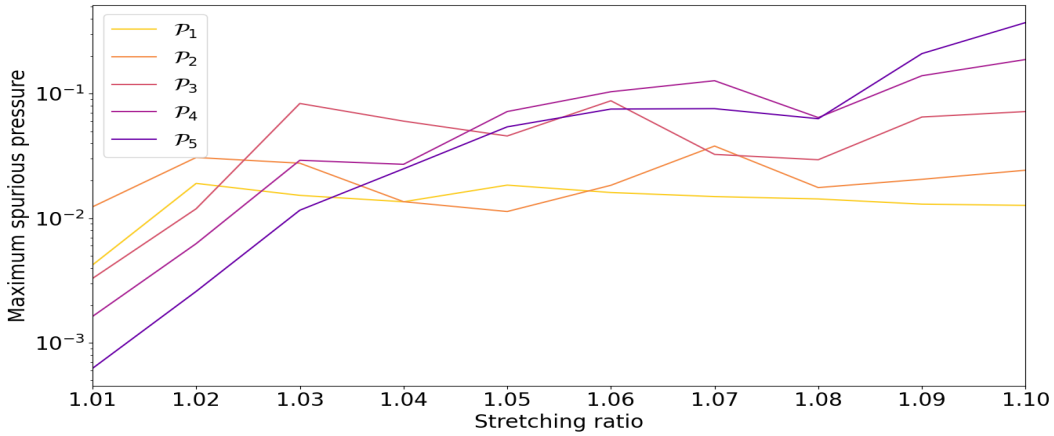

(a) Maximum spurious pressure oscillation amplitude

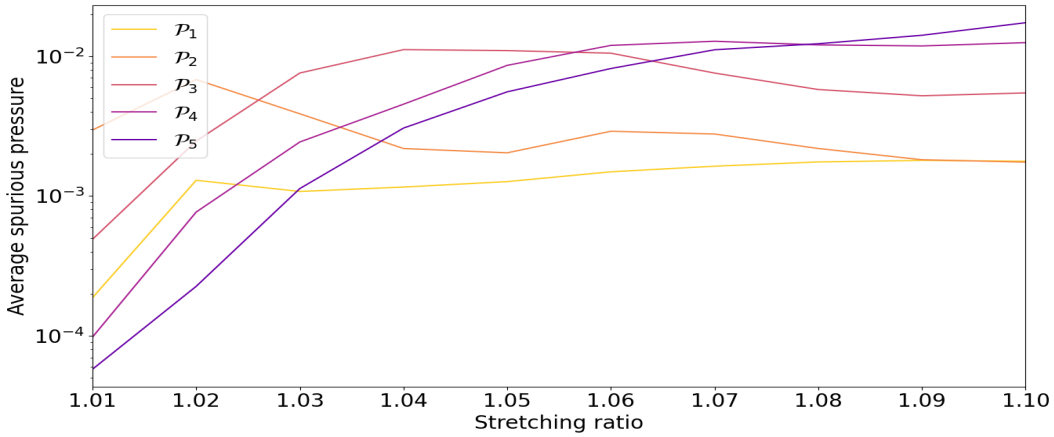

(b) Average spurious pressure oscillation amplitude

Figure 6.14. Maximum and average spurious pressure oscillations from isentropic vortex on stretched grids

Polynomial Adaptation

A highly attractive feature of element-based numerical methods, such as the FR method, is the ability to adjust the polynomial degree within individual elements to locally enhance the spatial resolution, often referred to as polynomial adaptation, or p-adaptation. P-adaptation is typically applied to elevate the spatial resolution in the vicinity of challenging flow features, including strong shocks and highly vortical structures [40]; however, applied as a boundary treatment method, p-adaptation acts inversely and decreases the polynomial degree to take advantage of the dissipative nature of low order solutions. Therefore, p-adaptation acts similarly to a sponge zone by decreasing the spatial resolution and under-resolving vortices before exiting the domain. Additionally, p-adaptation reduces the computational

demand, particularly in 2D and 3D simulations, as the DOF per element is significantly lowered with each reduction of the polynomial degree, as outlined in Table 3.1. Comparable to applying a large stretching ratio, rapidly decreasing the polynomial degree is likely to cause spurious reflections. Thus a gradual reduction in polynomial degree is required, as shown in Figure 6.15, which illustrates the $\mathcal{P}_5$ to $\mathcal{P}_1$ adaptation.

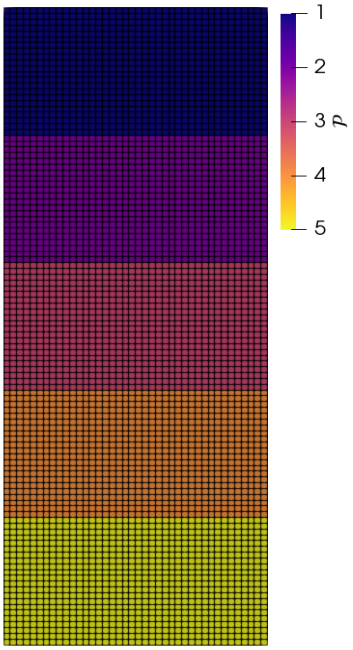

Figure 6.15. Isentropic vortex computational domain polynomial adaptation $\mathcal{P}_5$ to $\mathcal{P}_1$

The simulations, performed on uniform grids of $W_d = 25$ and $L = 110$, progressed for 100 t_c before the error values were recorded. All simulations were initialized with a $\mathcal{P}_5$ polynomial, and each subsequent simulation incrementally reduced the polynomial degree, ranging from $\mathcal{P}_4$ to $\mathcal{P}_1$, as seen in Figure 6.16. For all simulations, the p-adaptation was applied such that each polynomial degree contain an equal number of elements, as seen in Figure 6.15. The competency of p-adaptation, applied as a boundary treatment method, is fully recognized from Figure 6.16, as each subsequent reduction in polynomial degree yields a considerable reduction in vorticity. Note, although possible, further reduction to a $\mathcal{P}_0$ polynomial solution, which is mathematically similar to a FV scheme, is ill-advised, as such schemes are intrinsically unsuitable for steep gradients in the flow [40].

Evaluation of the error on a per DOF basis is negated by the application of p-adaptation, as each simulation does not contain an equal number of DOF. Therefore, similar to the sponge zone simulations, the maximum and average spurious pressure oscillations were recorded and are presented in Table 6.7. By comparing the results in Table 6.7 to those in Figure 6.14, it is evident that p-adaptation outperforms sponge zones as a boundary treatment method, as the amplitudes of the maximum and average spurious

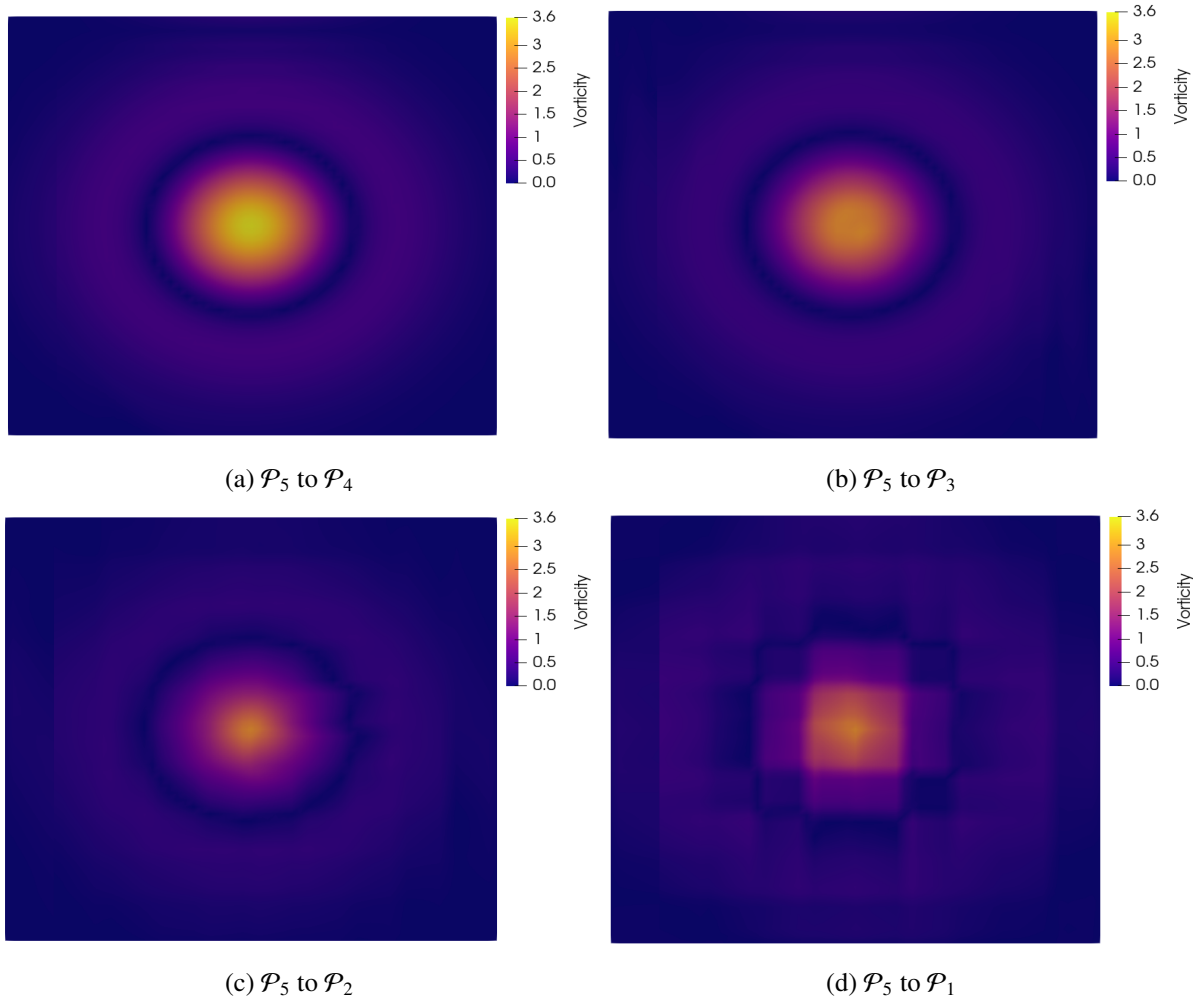

(a) $\mathcal{P}_5$ to $\mathcal{P}_4$

(b) $\mathcal{P}_5$ to $\mathcal{P}_3$

(c) $\mathcal{P}_5$ to $\mathcal{P}_2$

(d) $\mathcal{P}_5$ to $\mathcal{P}_1$

Figure 6.16. Isentropic vortex on p-adaptation grid

pressure oscillations caused by p-adaptation are roughly an order of magnitude smaller than those caused by sponge zones, even with the smallest stretching ratios. Spurious oscillations are created when there is a significant disparity in spatial resolution between neighboring elements, as epitomized by stretched grids. P-adaptation, on the other hand, solely experiences this disparity at the interface between two separate polynomial degrees, and therefore, produces significantly fewer spurious oscillations. In addition to producing minimal reflections, the uniformity of the grid enables the dissipation of outgoing vortices without dispersing the information. This is evidenced by comparing the diminished yet coherent vortex in Figure 6.16*d* to the highly dispersed vortex in Figure 6.13*c*.

P-adaption is a highly efficient boundary treatment method and is applied extensively throughout the remainder of this thesis, both to reduce the intensity of outgoing vortices and the computational cost. Similar to the sponge zone, a universal approach to applying p-adaptation is nonexistent, as the length of each individual polynomial region, as well as the required reduction in polynomial degree, strongly depend on the flow configuration; however, a set of best practices is presented. Firstly, to ensure minimal spurious

$\mathcal{P}$	Maximum pressure oscillation amplitude	Average pressure oscillation amplitude
$\mathcal{P}_5$ to $\mathcal{P}_4$	0.00019	4.48×10^{-5}
$\mathcal{P}_5$ to $\mathcal{P}_3$	0.0009	7.78×10^{-5}
$\mathcal{P}_5$ to $\mathcal{P}_2$	0.0042	7.37×10^{-4}
$\mathcal{P}_5$ to $\mathcal{P}_1$	0.0084	1.85×10^{-3}

Table 6.7. Maximum and average amplitudes of spurious pressure oscillations for p-adaptation simulations

oscillations, the length of each individual polynomial region should be at least twice the characteristic length, L_c, of the simulation. Secondly, when permissible, a large $\mathcal{P}_1$ region should be applied near the computational boundaries. As stated above, the dissipative nature of the $\mathcal{P}_1$ elements further aids in reducing outgoing vortices. Furthermore, if the outgoing vortices are insufficiently reduced before crossing the boundary and generate non-physical reflections, the poor propagative characteristic of the $\mathcal{P}_1$ elements severely hinders the non-physical reflections from propagating upstream and contaminating the acoustic field.

Artificial Viscosity

Although particularly adept at resolving many challenging flow features, high order numerical methods are poorly suited to resolve strong shocks, as they produce the well known Gibbs-type oscillations along discontinuities [35]. To reduce the intensity of these oscillations, the concept of artificial viscosity, which incrementally increases the numerical viscosity to provide additional dissipation to the system, was introduced [35]. Due to the innate dissipative capacity, the scope of artificial viscosity was quickly extended towards application as a boundary treatment method [60]. Contrary to applying artificial viscosity as a shock capturing method, which locally alters the numerical viscosity within individual elements, artificial viscosity as a boundary treatment method typically adjusts the viscosity over a large region, spanning a considerable number of elements. Accordingly, any solution obtained in the applied artificial viscosity boundary treatment region is fundamentally non-physical, thus requiring the artificial viscosity to be applied with a buffer region.

The simulations were performed on uniform grids of $W_d = 25$ and $L = 110$ and were progressed for 100 t_c before recording the error values. As the addition of artificial viscosity does not alter the DOF of the system, the number of elements for each simulation was adjusted to yield an equal DOF across all polynomial degrees. Similar to the sponge zone and p-adaptation, the artificial viscosity must be applied gradually to minimize the generation of spurious oscillations. For the simulations presented in

this section, the artificial viscosity, ν_a, was applied along a hyperbolic tangent profile

$$\nu_a = \left(\left(\frac{A}{2}\right) tanh\left(\epsilon\left(x_c - x\right)\right)\right) + \frac{A}{2}, \tag{6.10}$$

where A is the maximum amplitude of the artificial viscosity, ϵ controls the slope, and x_c is the geometrical center of the buffer zone. As detailed by Persson and Peraire [35], the addition of artificial viscosity significantly impacts the stability of the numerical method, and increasing the amplitude of the artificial viscosity reduces the maximum allowable time step size. Therefore, following the work of Staroverov *et al.* [60], who provide a detailed analysis on the application of artificial viscosity as a boundary treatment method, a value of A = 0.03 was selected, which provides significant dissipation while still permitting a relatively large time step. The results of the $\mathcal{P}_5$ simulation are shown in Figure 6.17, with the exact solution included for reference. The proficiency of applying artificial viscosity as a boundary treatment method is undeniably recognized, as the isentropic vortex is almost completely diminished. With an equal number of DOF, the addition of artificial viscosity yields similar results across all polynomial degrees, as evidenced by Figure 6.18, which plots the vorticity magnitude, recorded along the horizontal center-line of the vortex, for all polynomial degrees. The marginal disparities in the vorticity magnitudes are thus accredited to the individual propagation characteristics of each polynomial degree.

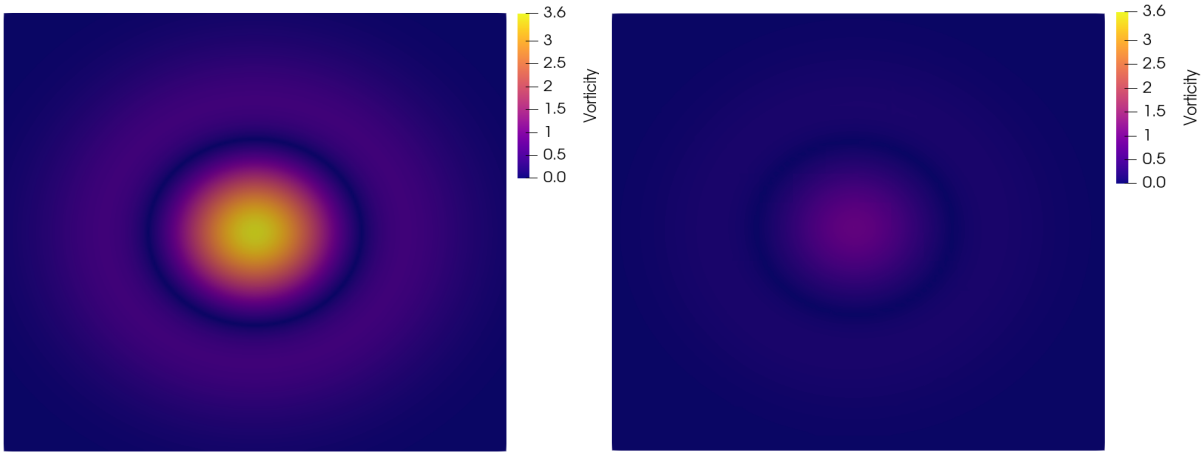

(a) Exact solution

(b) $\mathcal{P}_5$ solution

Figure 6.17. Effect of artificial viscosity on propagation of isentropic vortex

Of the boundary treatment methods discussed in this section, artificial viscosity provides the most powerful approach towards eliminating outgoing vortices before encountering the computational boundaries. Although locally adaptive artificial viscosity boundary treatment methods, which measure the vorticity in the far-field and adjust the artificial viscosity accordingly, have shown success [60], the method of application proposed in this section was chosen for two distinct reasons. First, applying the

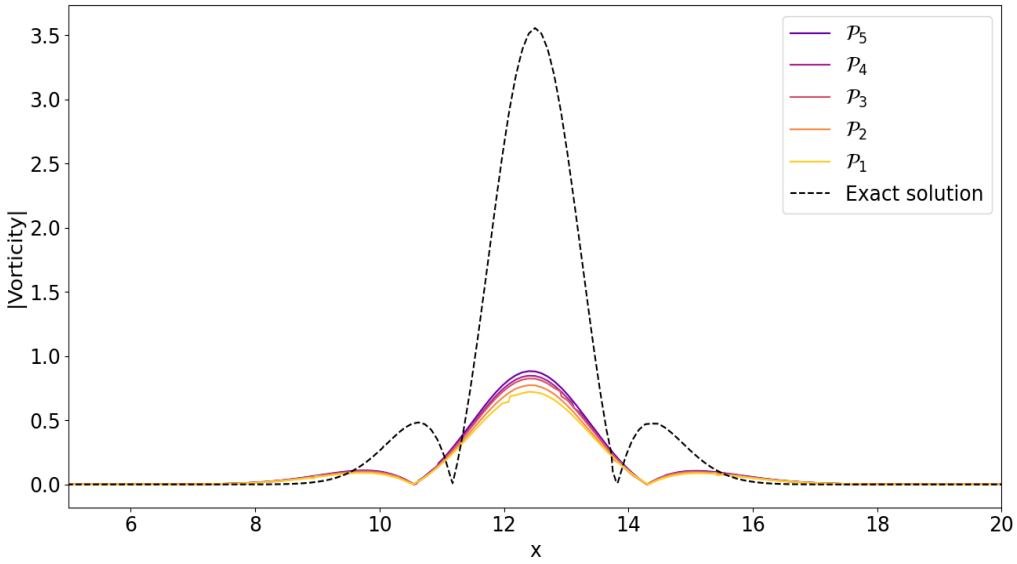

Figure 6.18. Vorticity amplitude of isentropic vortex with artificial viscosity

artificial viscosity along a constant profile is performed once, during the initialization of the simulation, and requires no additional measurements or calculations, as opposed to the adaptive methods, which necessitate supplemental vorticity measurements and calculations at every time step. Secondly, the gradual application of artificial viscosity provides ample dissipation, not only to the outgoing vortices, but also any spurious reflections which may be generated. Although tempting, the benefits of increasing the artificial viscosity amplitude to further dissipate outgoing vortices are quickly thwarted by the reduction in allowable time step sizes, which significantly increase the computational costs. Lastly, dissimilar to sponge zones and p-adaptation, which decrease the computational demand, artificial viscosity requires an additional calculation, specifically, the addition of the artificial and physical viscosities, and therefore slightly increases simulation run times. Therefore, throughout the remainder of this thesis, artificial viscosity is applied solely in vortex dominated regions, such as the wake behind a NACA0012 airfoil.

6.4.3 Discussion

A computational domain of infinite length cannot be calculated; therefore, the computational domain must be truncated. The truncation of the domain creates a non-physical boundary, which is liable to create non-physical reflections, potentially corrupting the acoustic field. To maintain generality towards both CFD and CAA applications, the well-known Riemann invariant BCs are applied throughout this thesis. Although well-suited for the passage of laminar flows, the Riemann invariant BCs are susceptible to produce non-physical reflections with the passage of highly vortical structures. These spurious reflections

are typically orders of magnitude smaller than the CFD variables of interest, and therefore, can be neglected in CFD applications. CAA applications, however, can not neglect these reflections, as they can severely pollute the acoustic field. Therefore, boundary treatment methods are applied, which aim to eliminate any outgoing vortices before encountering the computational boundaries. The application of boundary treatment methods is not a trivial process, as the required level of dissipation strongly depends on the flow configuration. Often, to increase the dissipation, several boundary treatment methods are applied simultaneously, for example, applying a stretching ratio inside the p-adaptation region. Caution must be applied when implementing a boundary treatment method, particularly the sponge zone, as large stretching ratios are liable to generate spurious reflections. As a universal boundary treatment method for the Riemann invariant BCs does not exist, the boundary treatments applied throughout this thesis were constructed iteratively and with a posteriori knowledge. The growth and advancement of direct CAA necessitates either the development of a general boundary treatment method, or perfectly NRBCs which are suitable for both CFD and CAA applications.

6.5 Discussion

The results presented in this Chapter verify that the four prevailing numerical challenges associated with CAA are well resolved by the FR method, especially when applied with high order polynomials.

The time-dependent nature of acoustic variables presents a challenging obstacle for numerical methods applied in direct CAA. Traditional, low-order methods, such as the FV method, operate rather inefficiently on modern hardware, and therefore, typically utilize low-fidelity approaches, including RANS, to minimize the computational costs. As demonstrated in Figure 6.2, the time-averaging employed by RANS completely expunges the acoustic field, thus invalidating its application, and subsequently, the application of inefficient, low order numerical methods towards direct CAA. The high order FR method, on the other hand, operates extremely efficiently on modern hardware and provides elevated levels of accuracy with fewer total DOF, as compared to low order methods. Accordingly, the high order FR method is well suited towards direct CAA, providing increased accuracy and the ability to apply high-fidelity approaches which do not utilize time-averaging, including DNS.

The proficiency of high order polynomials is recognized from the results of the grid convergence studies on the linear advection of a Gaussian pulse. In the 1D and 2D simulations, the high order polynomials, $\mathcal{P} \geq 3$, successfully converged to the expected orders of accuracy, while the low order polynomials were unable to with the applied grid resolutions. In the 3D simulations, only the $\mathcal{P}_4$ and $\mathcal{P}_5$

solutions converged to their expected order with the given grid spacing. Despite the fast and accurate converge rates of the high order polynomials, for every simulation, the high order polynomials provided higher accuracy on a per DOF basis than the low order polynomials, with the $\mathcal{P}_5$ polynomial proving the most accurate per DOF, thus substantiating the suitability of the high order FR method to propagate small scale acoustic waves accurately over large distances.

Compact, high-frequency acoustic waves, characterized by the sinusoidal Gaussian pulse simulations, require significant numerical resolution to accurately resolve. From Table 6.5, the low order polynomials, particularly the $\mathcal{P}_1$ polynomial, require an exceedingly large number of elements to converge to the same error level as the high order polynomial. Furthermore, the inability of low order polynomials to efficiently resolve highly fluctuating waves is evidenced by the massively disproportionate number of DOF required for convergence. The results in Table 6.5 epitomize the necessity of high order methods for direct CAA, particularly the application of the aforementioned high-fidelity approaches.

Effective BCs, which permit the smooth passage of both aerodynamic and aeroacoustic flow features, are of paramount importance to the field of direct CAA. To retain the accuracy of the simulations, the boundary treatments applied throughout the remainder of this thesis, often as a combination of the boundary treatment methods discussed in the previous section, are meticulously optimized for each individual simulation. The development of a universal boundary treatment is a pressing task for future considerations.

The necessity of high order solutions in direct CAA is undoubtedly identified, and therefore, the remainder of this thesis focuses on high order, specifically $\mathcal{P}_4$ and $\mathcal{P}_5$, solutions and does not consider the lower order polynomials, other than their implementation in p-adaptation as a boundary treatment method.

Lastly, in addition to the four numerical challenges unique to CAA as discussed in this Chapter, Tam also identified two conceptual challenges that are prevalent in CAA [21]. First, trailing edges and sharp corners act as effective acoustic generation mechanisms, and therefore, the applied numerical method must operate accurately and efficiently in the vicinity of complex geometries, commonly discretized with unstructured grids. Secondly, similar to the numerical resolution of turbulence, CAA contains an extensive range of length scales. In particular, the length scales of the acoustic sources are often orders of magnitude smaller than the length scales of the acoustic waves. Therefore, the numerical method must accurately resolve both small and large length scales within the same domain. The two conceptual challenges of CAA are addressed and verified in the following Chapters.

The following Chapter presents two canonical validation cases for direct CAA and compares the

high-order numerical solutions to reference and experimental data.

Chapter 7

Validation

The previous Chapter illustrates that the FR method sufficiently resolves each of the numerical challenges associated with CAA and emphasizes the proficiency of higher-order solutions. The objective of the current Chapter is to assess the aptitude of the high-order FR method as a direct near-field CAA method by performing several validation studies. Additionally, the boundary treatments discussed in the previous Chapter are implemented, and their performance is evaluated.

7.1 Flow Over a Cylinder

As stated in Chapter 5, the first successful CAA simulation [24] computed the acoustic field resulting from cylinder in mean flow. The relatively simple physics of this configuration allows for the straightforward, unambiguous identification of the alternating shedding of vortices as the primary acoustic source mechanism. Additionally, the steady fluctuation of vortices over the cylinder creates a uniform acoustic field. Furthermore, the Reynolds number is typically restricted to values in the range of $40 \lesssim R_e \lesssim 150$, as Reynolds numbers below this range do not produce an alternating vortex street and Reynolds numbers above this range are liable to cause the flow to transition into turbulence. The simple geometry and low Reynolds number allow for accurate and efficient calculation of the acoustic field, and as such, the flow over a cylinder has materialized into a canonical validation case for CAA.

7.1.1 Computational Details

The validation study presented in this section follows the work of Inoue *et al.* [61], who provide a detailed analysis of the flow over a cylinder and the corresponding acoustic characteristics. The simulation was performed with M_a, P_r, and R_e values of 0.2, 0.75, and 150, respectively, with the ratio of specific heats, γ,

set to 1.4. The cylinder diameter, d, equal to unity and centered at the origin, is used to non-dimensionalize all length scales present in the current case. The computational domain was radially extended to $200d$. The domain was split into two distinct regions, specifically, the acoustic region and the buffer region. The acoustic region, where all data measurements took place, extends to $100d$ and consists entirely of $\mathcal{P}_5$ elements. The buffer region, which reduces the strength of vortices before crossing the outflow boundary to prevent spurious reflections from contaminating the acoustic field, extends from $100d$ to $200d$ and contains $\mathcal{P}_4$ - $\mathcal{P}_1$ elements, as seen in Figure 7.1. A structured, quadrangular only domain was used with 72 equally spaced elements in the θ direction and 212 radial elements, for a total of 15,264 elements. To reduce the element count, the elements in the acoustic region were stretched using a stretching ratio of 1.04. The elements within the buffer region were not stretched as the p-adaptation provided effective grid stretching. In addition to the polynomial adaptation, artificial viscosity was applied in the buffer region to further reduce the strength of outgoing vortices, as shown in Figure 7.1. The Riemann invariant BCs detailed in the previous Chapter were applied to all inflow and outflow boundaries.

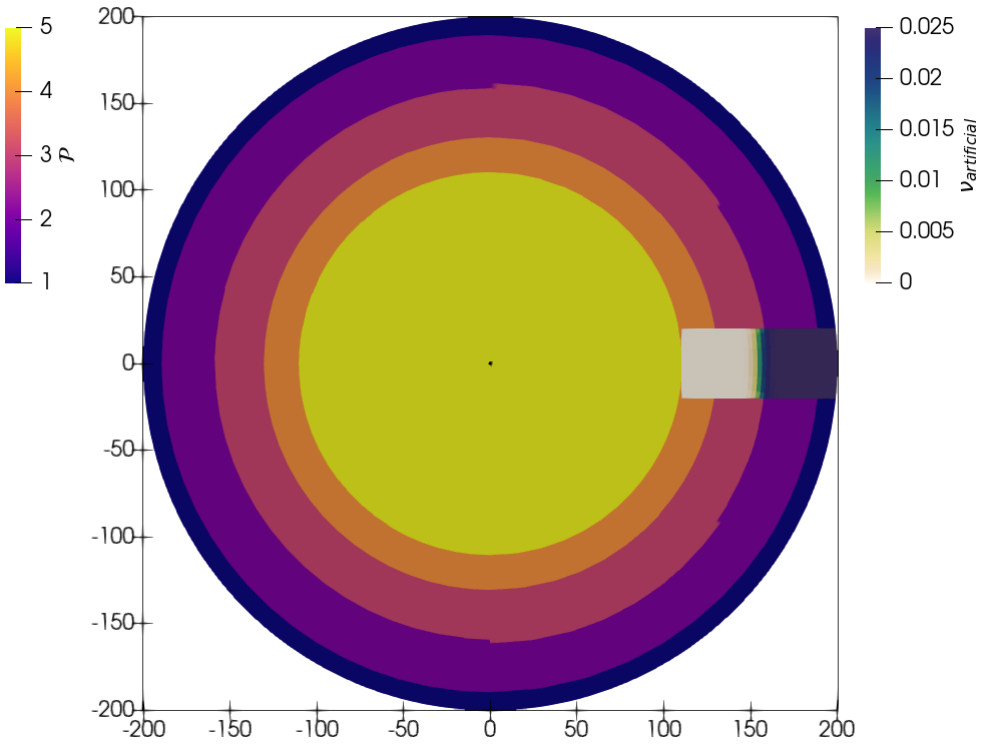

Figure 7.1. Radial polynomial adaptation for acoustic cylinder

The low Reynolds number used in the simulation results in a highly viscous flow, thus necessitating considerable resolution in the vicinity of the cylinder. The diminutive grid spacing required to achieve the proper resolution severely limits the maximum allowable time step size. The simulation was originally performed using the classic $RK_{4,4}$ time-stepping scheme. The maximum Δt which satisfied the CFL

limit was determined to be $\Delta t \approx 0.000178$, which proved to be prohibitively slow and computationally expensive. To alleviate these issues, the P-ERK time stepping scheme detailed in Chapter 4 was applied, with elements in the cylinder's immediate vicinity assigned 16 RK stages. The computational elements and their corresponding number of RK stages are shown in Figure 7.2, with all elements beyond the scope of the Figure assigned 4 RK stages. The increased number of RK stages near the cylinder permits a much larger time step size, $\Delta t \approx 0.0012$, while still satisfying the CFL limit, thus drastically reducing the computational expense.

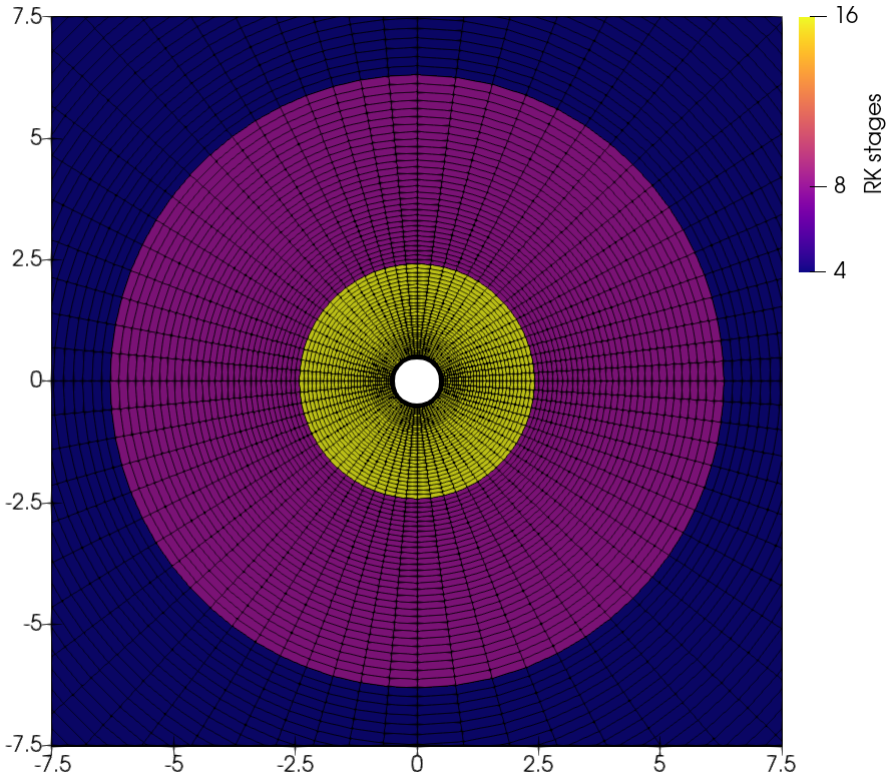

Figure 7.2. Runge-Kutta stages for acoustic cylinder

7.1.2 Results

Before proceeding with the CAA analysis, it is imperative to validate the CFD results to ensure the overall accuracy of the simulation. As CFD variables typically do not include the effects of transient flow, the simulation was progressed until a steady-state had been reached, after which the data measurements commenced. Figure 7.3 shows the time history of the non-dimensional pressure at a point located directly in the wake and illustrates the simulation reaching steady-state after approximately 200 non-dimensional time steps. Note that unless explicitly stated otherwise, all time and pressure values, including the time-averaged and acoustic components, presented throughout the remainder of this thesis follow the non-dimensionalization techniques applied in Figure 7.3.

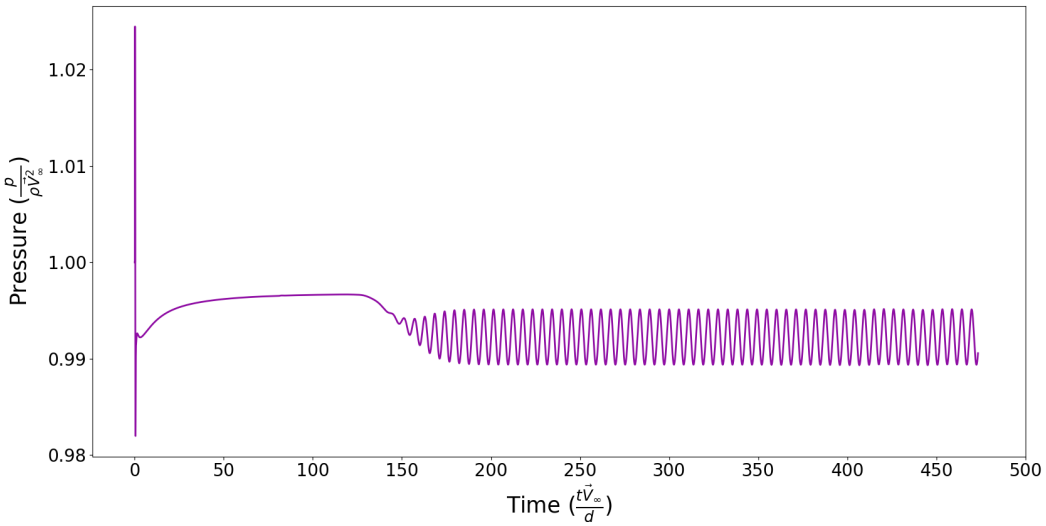

Figure 7.3. Time history of pressure in cylinder wake

From Figure 7.3, the vortex shedding frequency, ω, was determined by calculating the inverse of the time between successive peaks. The vortex shedding frequency, ω, was then used to calculate the Strouhal number, S_t, as

$$S_t = \frac{\omega d}{\vec{V_\infty}}. \tag{7.1}$$

Figure 7.4 shows the computed S_t number against the empirical S_t line, with supplemental experimental data for reference. The calculated S_t number agrees well with the empirical line as well as the experimental data of Inoue and Hatakeyama [61]. As an additional means of validating the CFD results, the calculated coefficients of pressure, C_P, lift, C_L and drag, C_D, as defined in Equation 7.2, where L_F and D_F are the non-dimensional lift and drag forces, respectively, and A_c is the characteristic area, are shown in Figure 7.5.

$$\begin{aligned} C_p &= \frac{p - p_0}{\frac{1}{2}\rho V_\infty^2} \\ C_L &= \frac{L_F}{\frac{1}{2}\rho V_\infty^2 A_c} \\ C_D &= \frac{D_F}{\frac{1}{2}\rho V_\infty^2 A_c} \end{aligned} \tag{7.2}$$

The pressure, lift, and drag coefficients in Figure 7.5 are in excellent agreement in both phase and magnitude with those reported by Inoue *et al.* [61], with an error value of less than 0.1 percent, illustrating the accuracy of the CFD results.

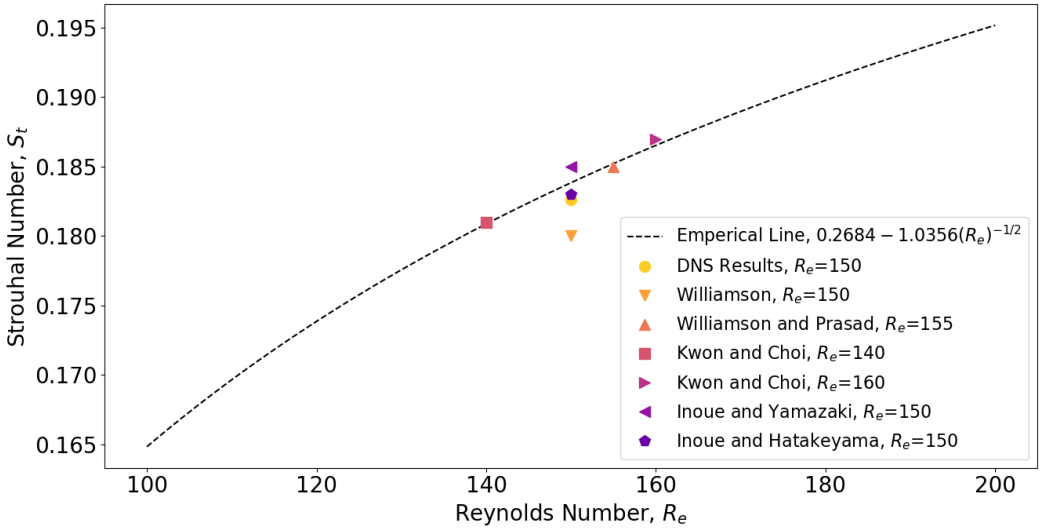

Figure 7.4. Strouhal number for cylinder

With the CFD results validated, the validation of the CAA results can now be properly assessed. Inoue *et al.* begin the validation process by investigating the mechanisms responsible for the generation of acoustic waves. This is done by comparing the time development of the vorticity field in the wake to the time development of the near-field acoustic pressure, as seen in Figures 7.6 and 7.7. Figure 7.6*a* displays the instantaneous vorticity field as a vortex is shed off the top half of the cylinder while Figure 7.6*b* shows the corresponding vorticity field as a vortex is shed off the bottom half of the cylinder. The vorticity fields of Figures 7.6*a* and 7.6*b* are of equal magnitude and near-perfect phase opposition, perfectly illustrating that the flow has reached a steady-state of oscillation. From Figure 7.7*a*, which shows the acoustic pressure field at the same time instance as Figure 7.6*a*, it is evident that as a vortex sheds over the top half of the cylinder, a negative acoustic pressure pulse is generated from the top half of the cylinder and a positive acoustic pressure pulse is generated from the bottom half of the cylinder, denoted by the negative and positive signs, respectively. Figure 7.7*b*, captured at the same time as Figure 7.6*b*, demonstrates that the shedding of a vortex from the bottom half of the cylinder acts inversely, generating a positive acoustic pulse from the top half of the cylinder and a negative acoustic pulse from the bottom. As the positive acoustic pulse on the upper half of the cylinder is generated, the negative acoustic pulse from Figure 7.7*a*, denoted again by the minus sign, is propagated outward, confirming that the alternating shedding of vortices acts as the primary source of acoustic generation [61]. Additional noise sources, including the leading edge noise and the noise from the rotating free stream vortices, are orders of magnitude smaller than the noise generated by the shedding vortices and therefore are often ignored.

With the identification of the acoustic sources concluded, the propagation characteristics of the

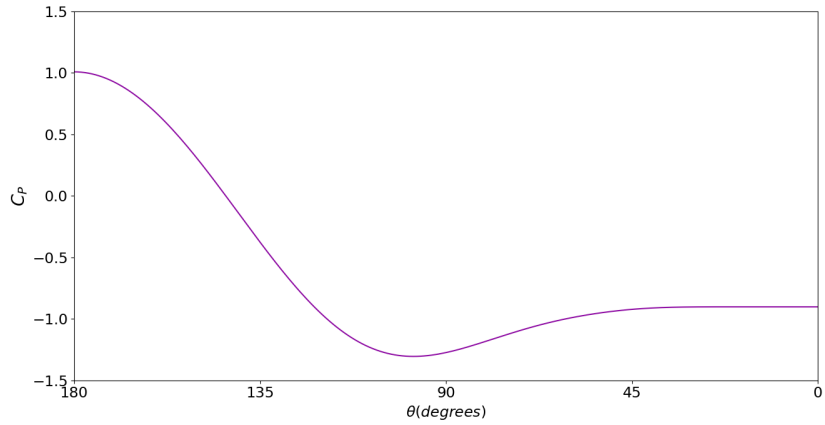

(a) Time-averaged pressure coefficient

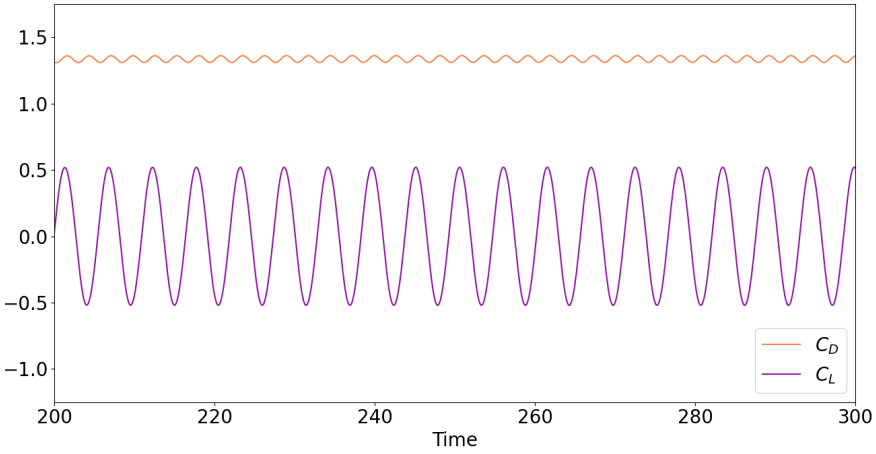

(b) Lift and drag coefficients

Figure 7.5. Force coefficients acting on cylinder

acoustic field are examined. From Figure 7.6, it is evident that the vortices are shed at ± 90^o from the cylinder, and therefore the acoustic pulses are expected to propagate along the same angles; however, in Figure 7.7 the acoustic pulses appear to propagate upstream, at a propagation angle, θ_p, of roughly θ_p = 101.5 degrees. This is not a defect of the FR method but rather a direct manifestation of the Doppler effect [61], which changes the frequency of the acoustic waves proportional to the fluid velocity. The Doppler effect's influence on the directivity of the acoustic field is visualized in Figure 7.8, where the acoustic pressure under the influence of the Doppler effect, p'_D, was recorded along a circle of radius, R, 75, centered at the origin. The resulting directivity field is shifted upstream along the propagation angle, as shown by the dashed line connecting the origin and the maximum value. Although p'_D displays the true propagation of the acoustic waves, it is often more convenient to analyze the propagation of acoustic waves independent of the fluid velocity. This is accomplished by introducing the modified acoustic

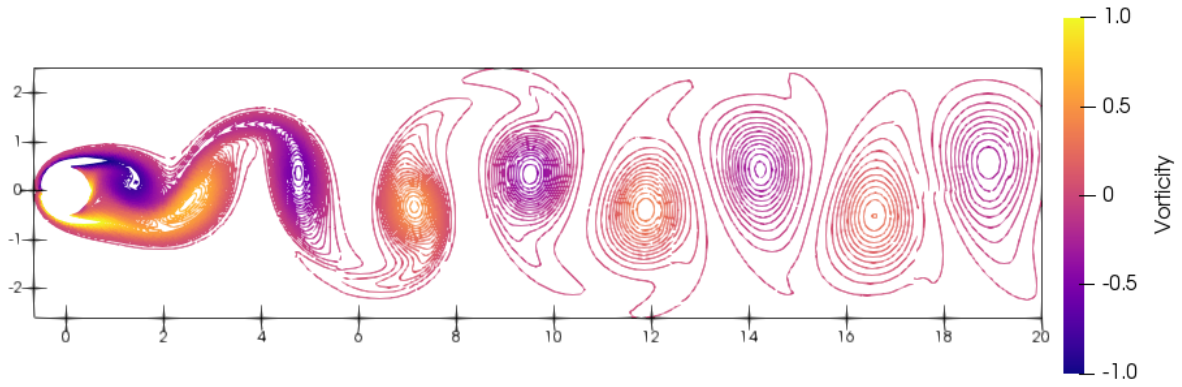

(a) Vorticity contours in range [-1,1], t = 283.97

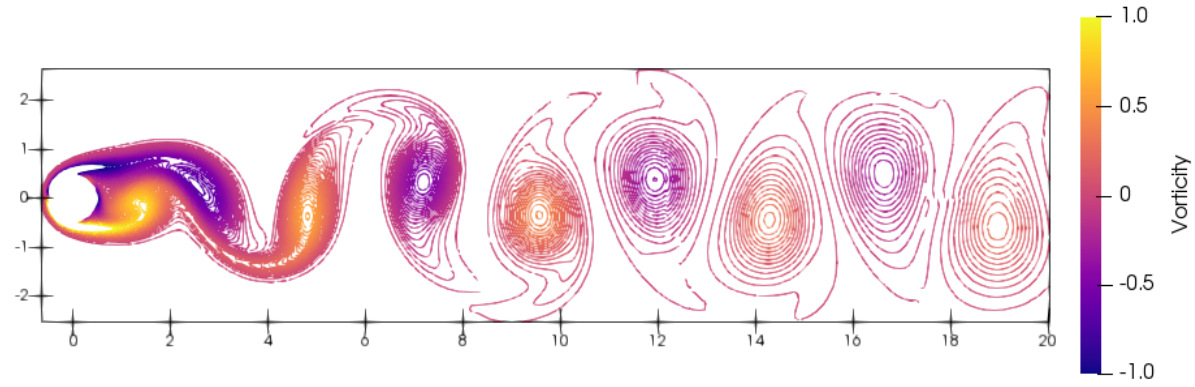

(b) Vorticity contours in range [-1,1], t = 289.89

Figure 7.6. Cylinder wake vortex shedding

pressure, p'_M, which eliminates the influence of the Doppler effect. The modified acoustic pressure was recorded along a circle centered at the origin, with a modified radius, R_M,

$$R_M = \frac{R}{1 - M_a \cos(\theta)}. \tag{7.3}$$

This transformation eliminates the impact of the Doppler effect, as seen in Figure 7.8, where the modified acoustic pressure creates a perfectly dipolar directivity field with the acoustic waves propagating at the expected $\pm 90^o$.

Continuing with the analysis of the acoustic propagation characteristics, Inoue *et al.* evaluate the effect of the average pressure on the total and acoustic pressure fields. The total pressure field, comprised of both the acoustic and average pressure fields, is shown in Figure 7.9*a* with the isolated acoustic and average pressure fields shown in Figure 7.9*b* and 7.9*c*, respectively. The average pressure field contains no temporal information, and therefore is perfectly symmetrical about the x-axis, as seen in Figure 7.9*c*. The acoustic pressure field in Figure 7.9*b* further illustrates the impact of the Doppler effect, with the

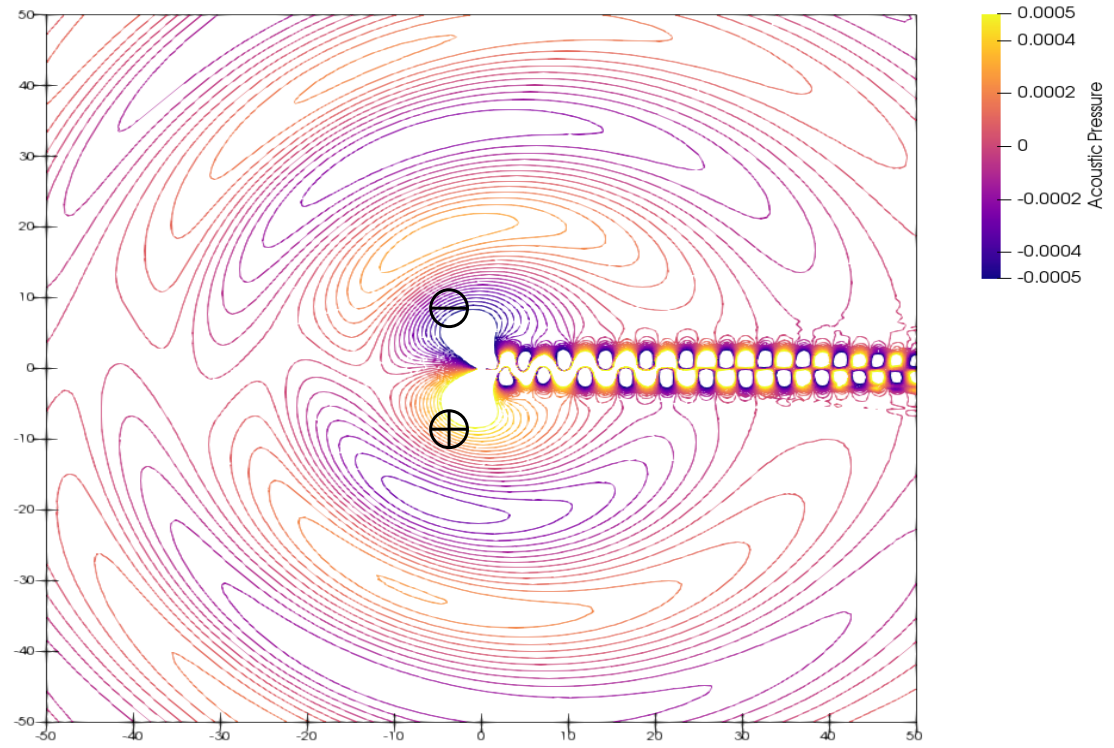

(a) Acoustic pressure, t = 283.97

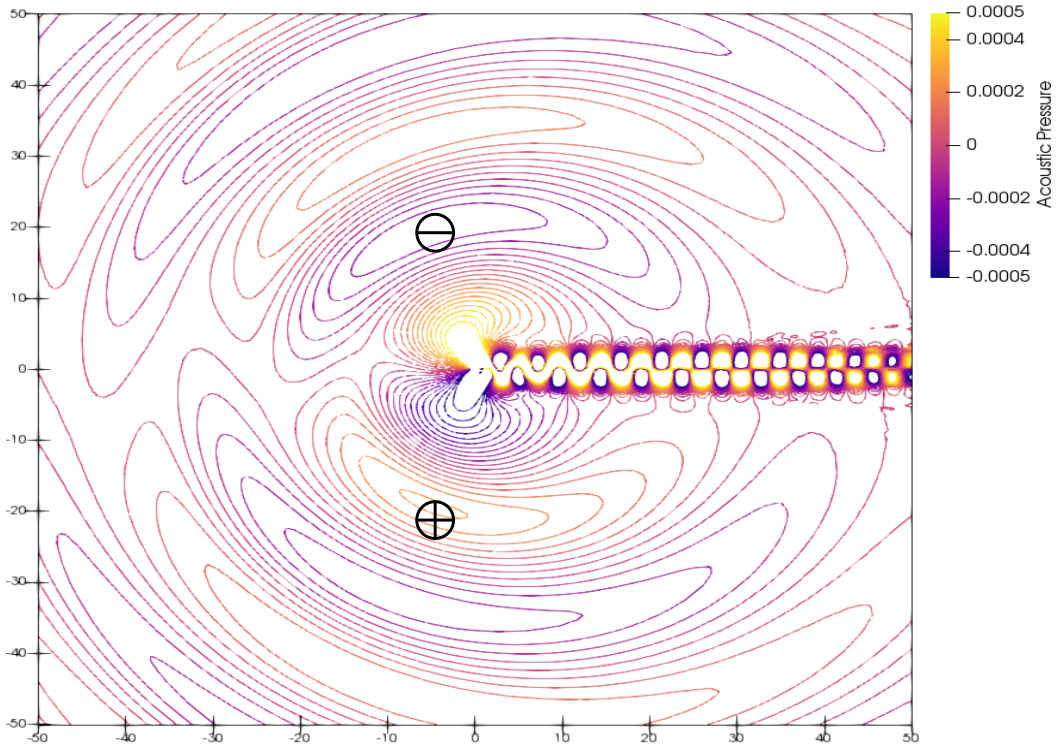

(b) Acoustic Pressure, t = 289.89

Figure 7.7. Acoustic pressure contours in range $[-5 \times 10^{-4}, 5 \times 10^{-4}]$

acoustic pressure pulses propagating along the propagation angle $\theta_p = 101.5^o$. The total pressure field, as seen in Figure 7.9*a*, however, displays a unique and counter-intuitive directivity pattern, with the

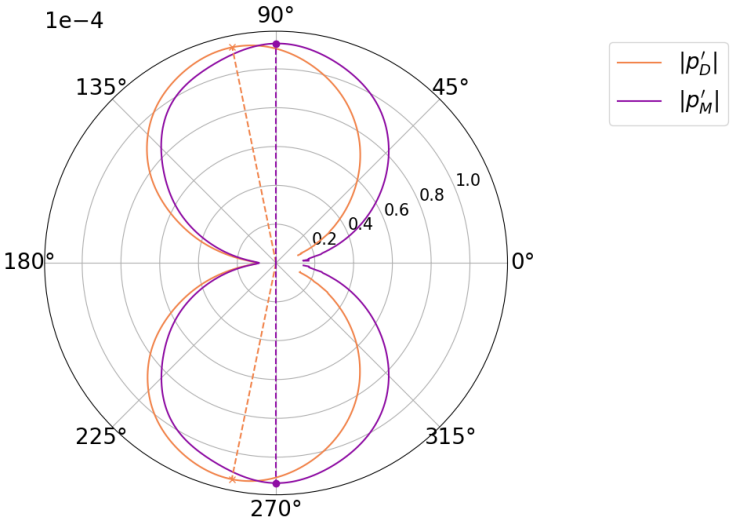

Figure 7.8. Doppler effect on acoustic pressure directivity

positive and negative pressure pulses seemingly propagating in different directions. The positive pressure pulses, denoted again by $\oplus$, propagate at approximately $\pm\ 130^o$, while the negative pulses propagate at roughly $\pm\ 60^o$. The apparent differences between the total and acoustic pressure fields is best explained by comparing the radial distribution of the total, acoustic, and average pressures, as seen in Figure 7.10. The positive total pressure pulses appear to propagate at $\pm 130^o$ owing to the positive value of average pressure, which increases the total pressure, as seen in Figure 7.10*a*. At $\pm 50^o$, the inverse occurs, where the negative values of average pressure reduce the total pressure, thus giving the impression of negative total pressure propagation, as seen in Figure 7.10*c*. Along the true propagation angle of $\theta_p = 78.5^o$, the average pressure tends to zero, resulting in total and acoustic pressure fields with remarkably similar magnitudes.

As a final means of validation, the rate of decay of the acoustic waves is measured. Figure 7.11*a* depicts the propagation of an acoustic wave, measured along 90^o, for three subsequent instances in time. As clearly shown, the magnitude of the acoustic wave diminishes both radially and temporally. The rate of decay for acoustic waves is governed by the inverse-square law [61], dictating that acoustic waves decay proportionately to the inverse-square root of the distance from the acoustic source. Figure 7.11*b* plots the magnitude of all the acoustic maxima and minima for the time range depicted in Figure 7.11*a*, against the radial distance from the top of the cylinder, with the inverse-square root of the radius included for comparison. Clearly, the rate of decay of the acoustic waves is well captured as the slope of the acoustic maxima and minima are parallel to the inverse square root of the radius.

Lastly, the effectiveness of the applied boundary treatments is analyzed. From Figure 7.12, which

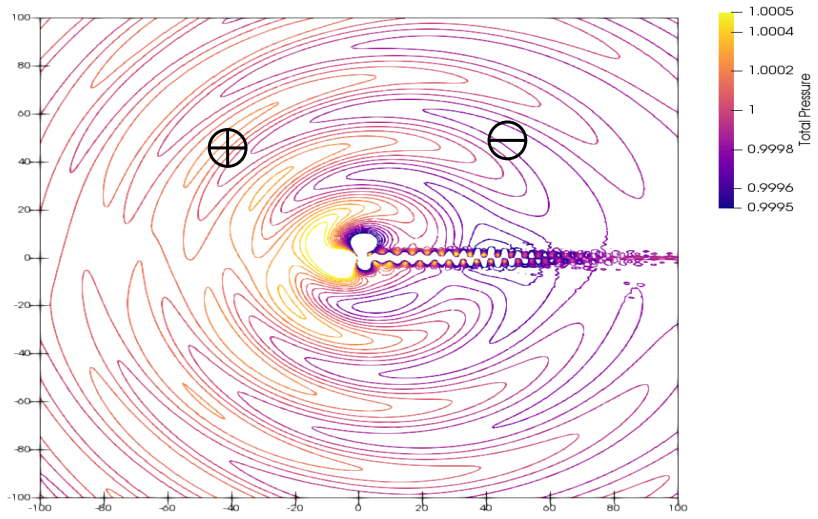

(a) Total pressure

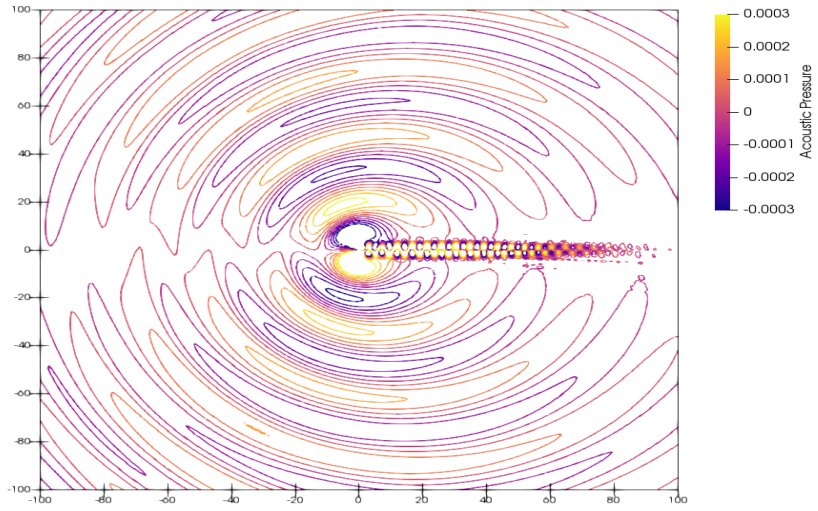

(b) Acoustic pressure

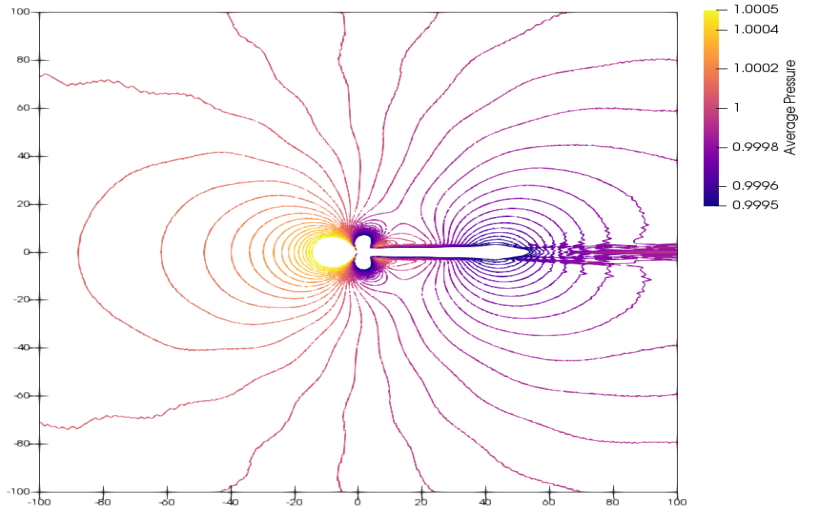

(c) Average pressure

Figure 7.9. Total, acoustic, and average pressure contours at t = 1200s

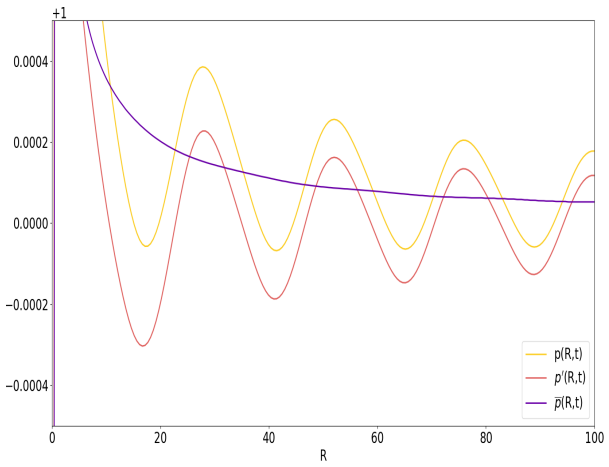

(a) Radial distribution along $\theta = 130^o$

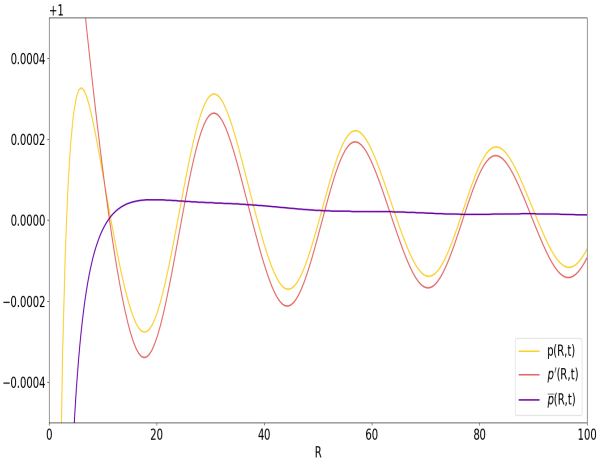

(b) Radial distribution along $\theta_p = 78.5^o$

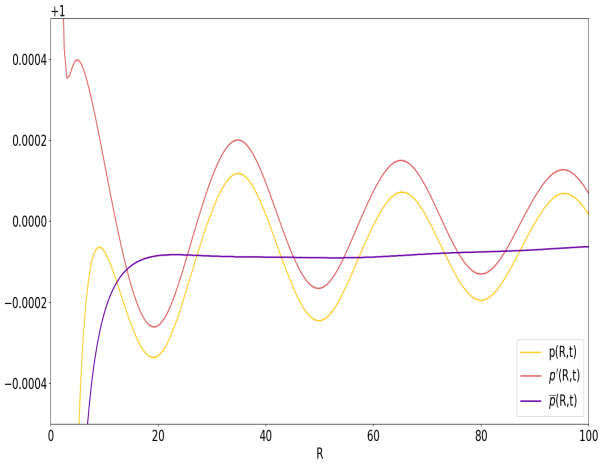

(c) Radial distribution along $\theta = 50^o$

Figure 7.10. Radial distribution of total, acoustic, and average pressures at t = 283.97

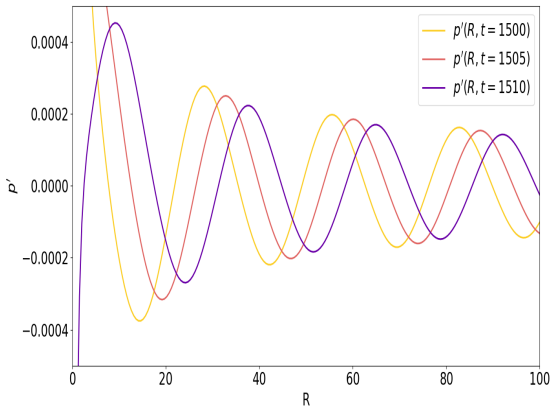

(a) Time history of acoustic propagation along $\theta = 90^o$

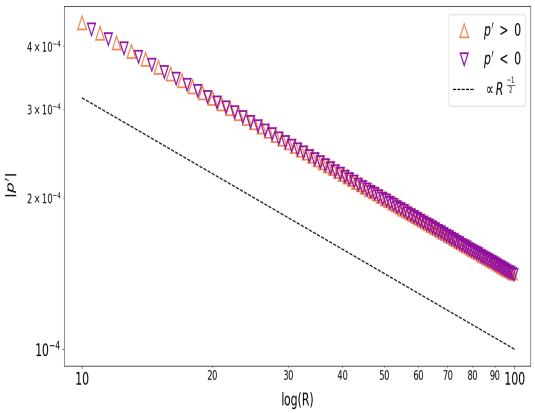

(b) Decay of acoustic pressure peaks along $\theta = 90^o$

Figure 7.11. Propagation and decay of acoustic pressure waves

shows the acoustic pressure field over the entire domain, it is evident that the polynomial adaptation in conjunction with the artificial viscosity completely diminishes the vortices before reaching the outflow

boundary. Within the acoustic region, the vortices behind the cylinder are still present, but quickly diminish with the addition of the artificial viscosity. It must be made clear that adding viscosity to diminish vortices produces a non-physical solution, and therefore can only be applied in the buffer region, where no data measurements are recorded. Additionally, the increased grid spacing obtained from the polynomial adaptation results in a severely under-resolved solution, visualized by the block-like solution near the outflow boundary. Although the applied boundary treatments contaminate the solution in the buffer region, no spurious reflections are produced at the outflow boundary, indicating that artificial viscosity and polynomial adaptation are effective boundary treatments for the FR method in direct CAA simulations. It is worth noting that the considerable length of the domain aids in the reduction of the vortices; however, as stated in Chapter 6, increasing the length of the domain is inefficient as a stand-alone boundary treatment and therefore is not considered in this validation study.

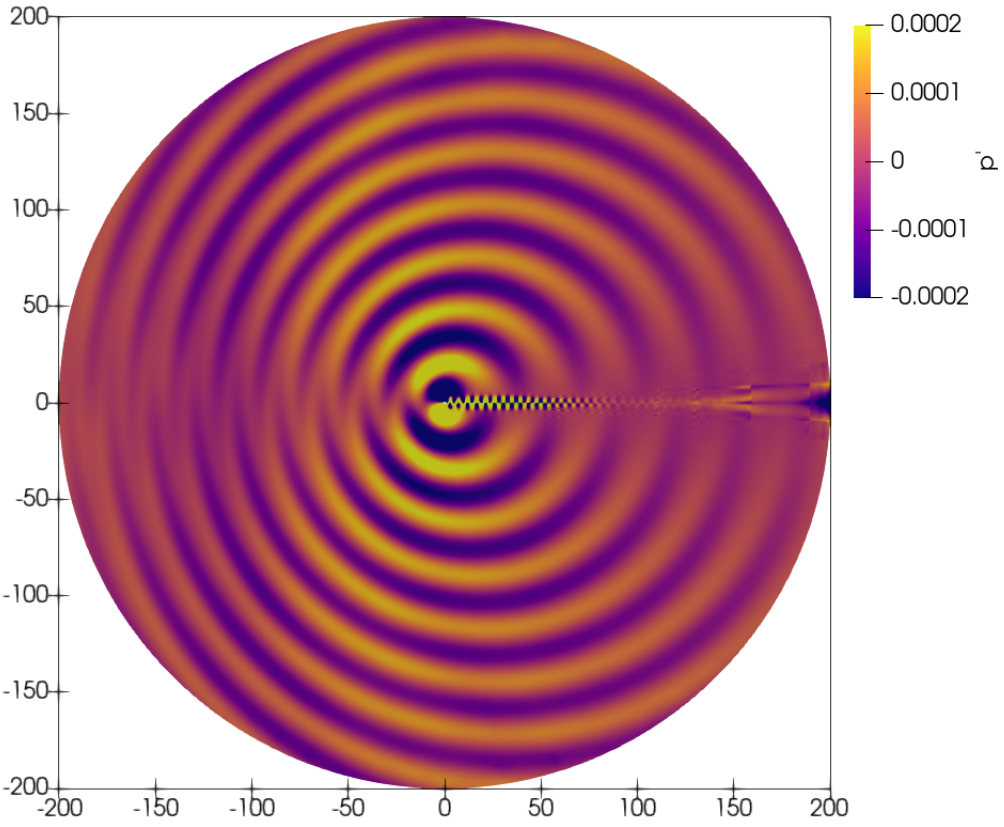

Figure 7.12. Cylinder boundary treatments

The overall agreement between the results presented in the current section and those reported by Inoue *et al.* validate the ability of the FR method to accurately capture both the mechanisms responsible for acoustic generation and the near-field acoustic propagation characteristics, including the directivity, magnitude, and decay of acoustic waves, directly from the results of the CFD simulation. Furthermore, the applicability of Riemann invariant BCs, combined with polynomial adaptation and artificial viscosity,

is substantiated as an acceptable BC for direct CAA.

Although the current validation case provides an inexpensive means to test the aptitude of numerical methods for application in direct CAA, the simple geometry and low Reynolds number result in a relatively simple flow configuration, the likes of which are not encountered in practical applications. To further validate the FR method's performance and to substantiate the applicability towards real-world CAA applications, an additional, far more computationally intensive validation case is presented in the following section.

7.2 Flow Over a Deep Cavity

The following validation case was selected from the National Aeronautics and Space Administration's (NASA) Third Computational Aeroacoustics Workshop on Benchmark Problems [59] as a challenging means in which to validate the performance of the FR method as a direct CAA approach towards complex, industrial applications. The case details the flow of air over an open cavity with an overhanging lip, commonly encountered in the automobile industry as the gap between doors, which has been determined as a significant contributor to automobile noise via the generation of distinct tonal frequencies. The tonal frequencies and corresponding SPL are recorded at the center of the vertical wall of the over-hanging lip, and the results are compared to the experimental data provided by the Workshop.

7.2.1 Computational Details

The cavity's geometric configuration is presented in Figure 7.13, with all length scales non-dimensionalized by the width of the cavity, W_d. The problem specifies a free stream velocity, $\vec{V}_\infty$, of 50.9 m/s and a laminar boundary layer with displacement thickness, δ^*, of $0.87W_d$ at the opening of the cavity. These values correspond to a Reynolds number based on boundary layer displacement thickness, $R_{e\delta^*}$, of 47,093 and Mach value of $M_a = 0.147$. The Prandtl number and the ratio of specific heats were set to 0.72 and 1.4, respectively. In lieu of implementing the one-seventh power-law velocity profile at the inflow boundary, as suggested by the CAA workshop, the inflow length, L_i, was extended to allow for the natural development of the boundary layer. Additionally, to ensure the vortices created by the cavity did not contaminate the acoustic field by creating spurious reflections when exiting the domain, the outflow boundary was also extended. As seen in Figure 7.14, polynomial adaptation was applied along the outflow wall to provide additional damping to the outgoing vortices. The surface friction produced by the no-slip BC, applied along the horizontal and vertical walls, reduces the intensity of outgoing vortices, similar

to the addition of artificial viscosity, thus providing a sufficient boundary treatment. As a supplemental means of eliminating vortices before encountering the outflow boundary, a large stretching ratio of 1.1 was applied in the $\mathcal{P}_1$ region of the domain. As determined in Chapter 6, large stretching ratios quickly diminish vortices but are liable to cause non-physical reflections; however, the high dissipation rate of the low order $\mathcal{P}_1$ elements effectively damps any spurious reflections, as demonstrated in the following section.

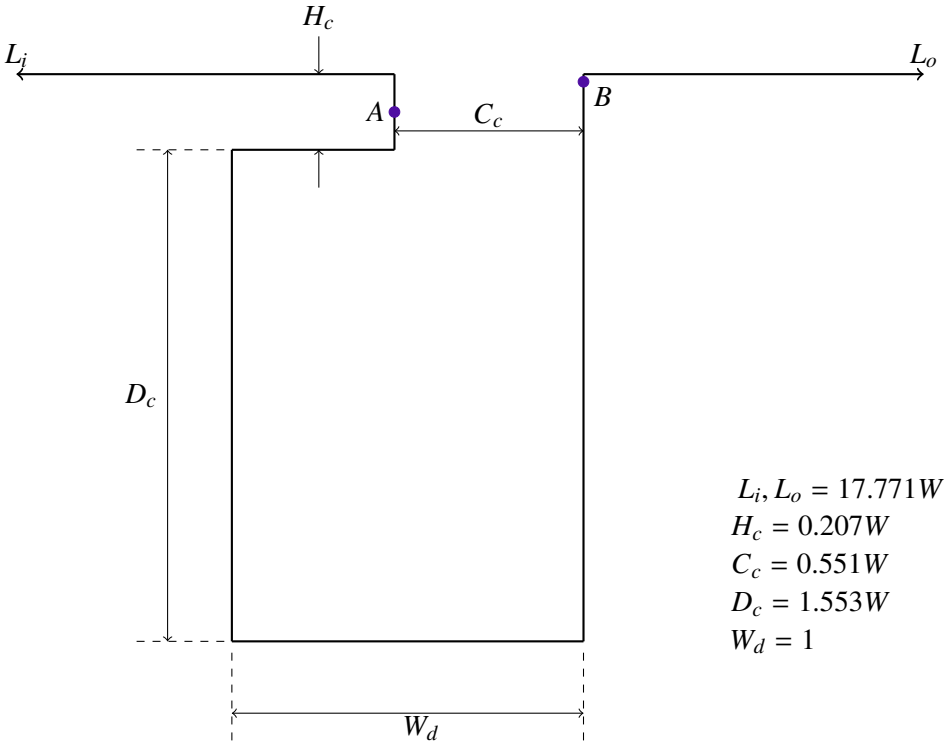

Figure 7.13. Cavity geometry

As reported by the Workshop's participants, the quality of both the CFD and CAA solutions are directly proportional to the grid resolution. To avoid performing a grid convergence study, an equivalent grid resolution to those employed by the low-order FV codes of the Workshop participants was applied, resulting in a comparable number of DOF while significantly reducing the total element count. The applied grid resolution is visualized in Figure 7.15, which shows the computational elements inside the cavity, with enhanced resolution near the walls and around corners. A structured, quadrangular grid was applied throughout cavity, with 60 elements along D_c, 50 elements along W_d, and 15 elements along H_c for a total of 3,525 $\mathcal{P}_5$ elements, resulting in 126,900 DOF within the cavity and cavity opening. To ensure all length scales within the flow were adequately resolved, a y^+ value of 0.5 was applied throughout the domain. Although the stringent y^+ value assures the obtained solutions are independent of the mesh, the maximum allowable Δt is severely limited. To compensate for the small y^+ value, the P-ERK time

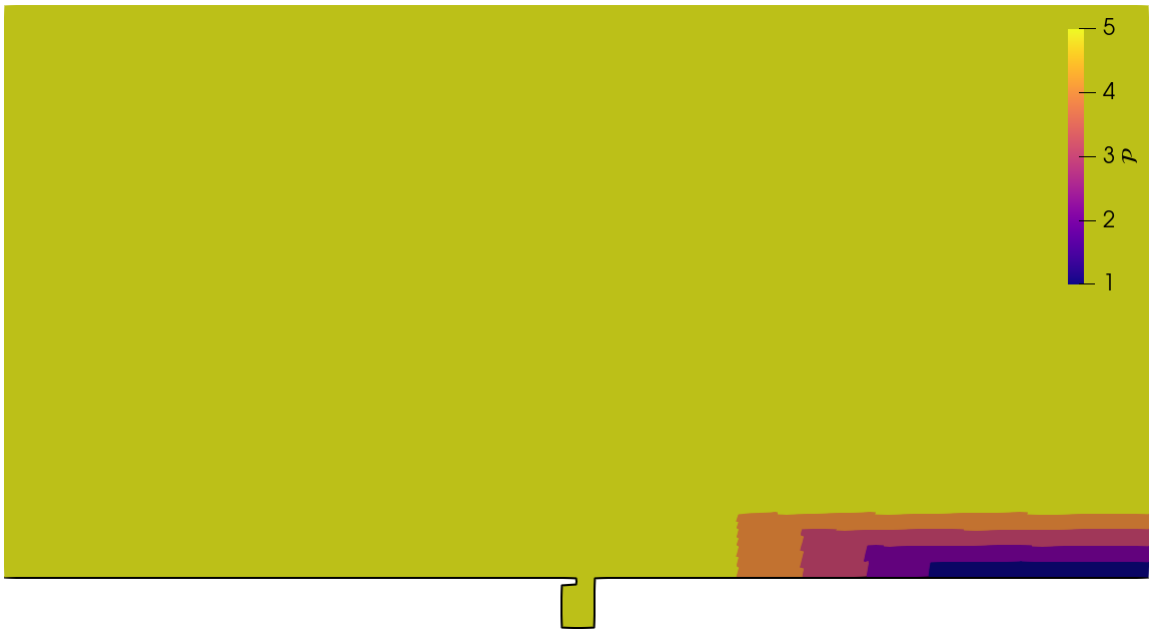

Figure 7.14. Polynomial degree for cavity flow

stepping scheme was applied, with the applied number of RK stages shown in Figure 7.16. To satisfy the CFL criteria, 16 RK stages were applied to the smallest elements, in particular those along walls and within boundary layers. The size of the elements increases proportionally to the distance from the wall, and accordingly, the corresponding number of RK stages decreases. This pattern continues until sufficiently far from the wall where the effects of viscosity are mitigated, after which all elements are assigned 4 RK stages.

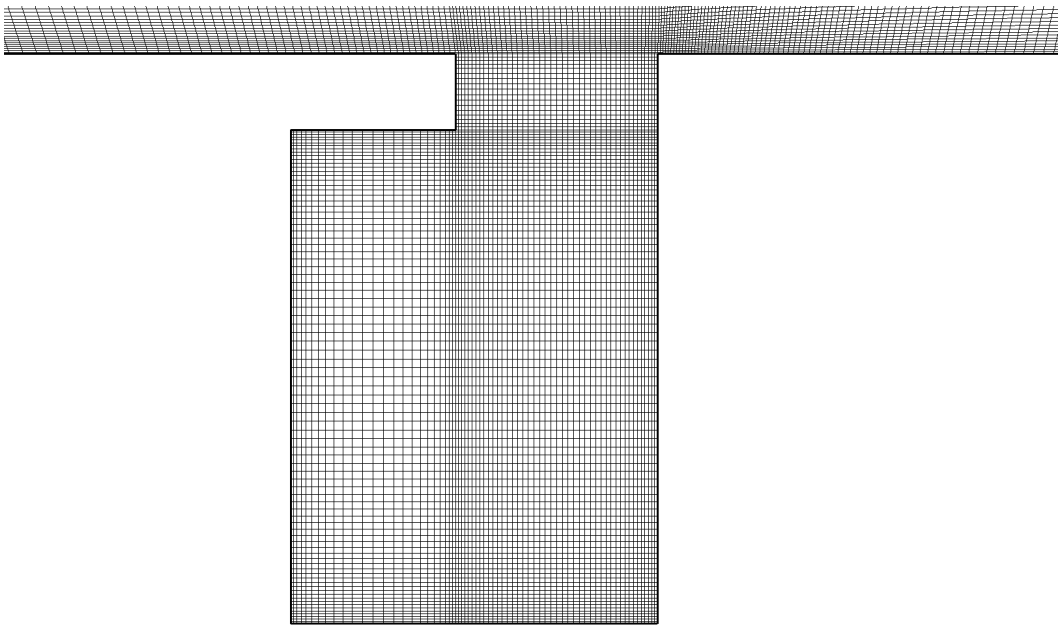

Figure 7.15. Cavity computational mesh

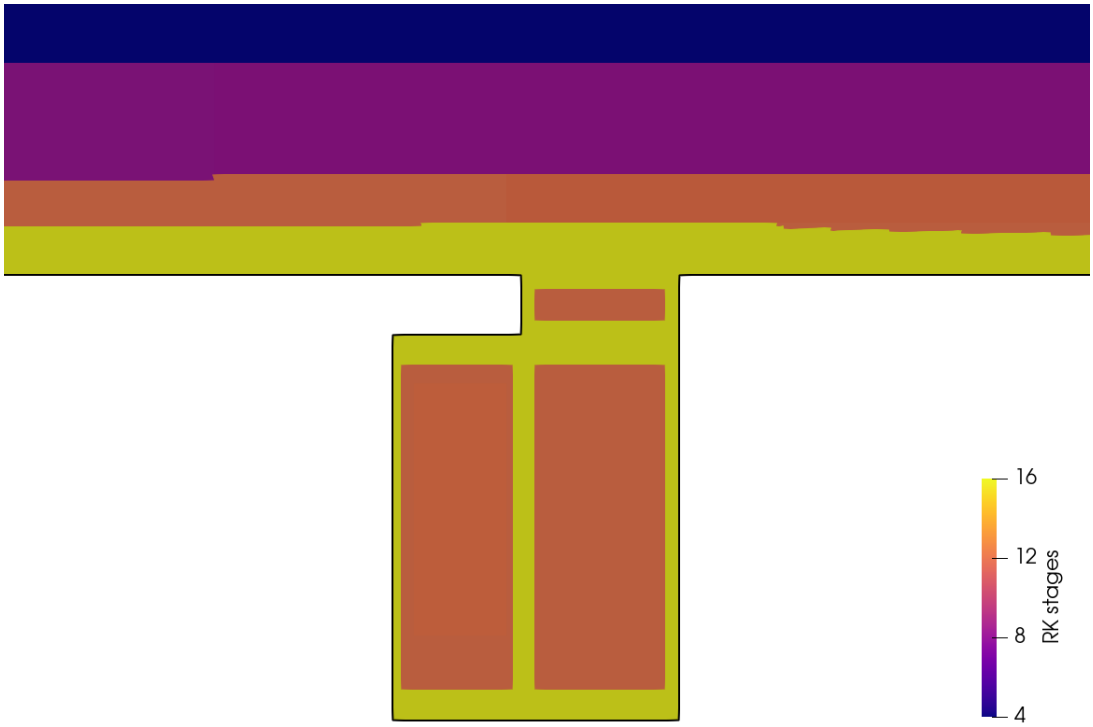

Figure 7.16. Runge-Kutta stages for cavity flow

7.2.2 Results

As a preliminary means of validating the results of the current simulation, the CFD results are compared to those of Tam *et al.* [62] in their investigation on the tones and pressure oscillations induced by flow over rectangular cavities. For deep cavities, such that $(D_c+H_c)>W_c$, Tam *et al.* detail the oscillation mechanisms responsible for generating acoustic waves. As the flow develops, instabilities in the shear layer at the mouth of the cavity become unstable and eventually cause the shear layer to oscillate, similar to the wake behind a cylinder. As shown in Figure 7.17*a*, as the shear layer oscillates upward, a vortex forms at the cavity's downstream edge and deflects the free-stream fluid out of the cavity, creating a low pressure system inside the cavity. This period of the oscillation cycle is often referred to as the expansion mode. As the shear layer transitions to a downward motion, the vortex at the downstream edge of the cavity rolls up over the corner and convects downstream, as shown in Figure 7.17*b*. This forces the free-stream fluid to impinge on the downstream cavity wall, creating a high pressure system inside the cavity, referred to as the compression mode of oscillation. The vortex at the edge of the over-hanging lip in figure 7.17*b* convects downstream, forcing the shear layer to oscillate upward, thus restarting the oscillation cycle.

The true cyclical nature of the oscillating shear layer, responsible for the alternating expansion and compression modes, is definitively identified in Figure 7.18, which shows the time history of pressure

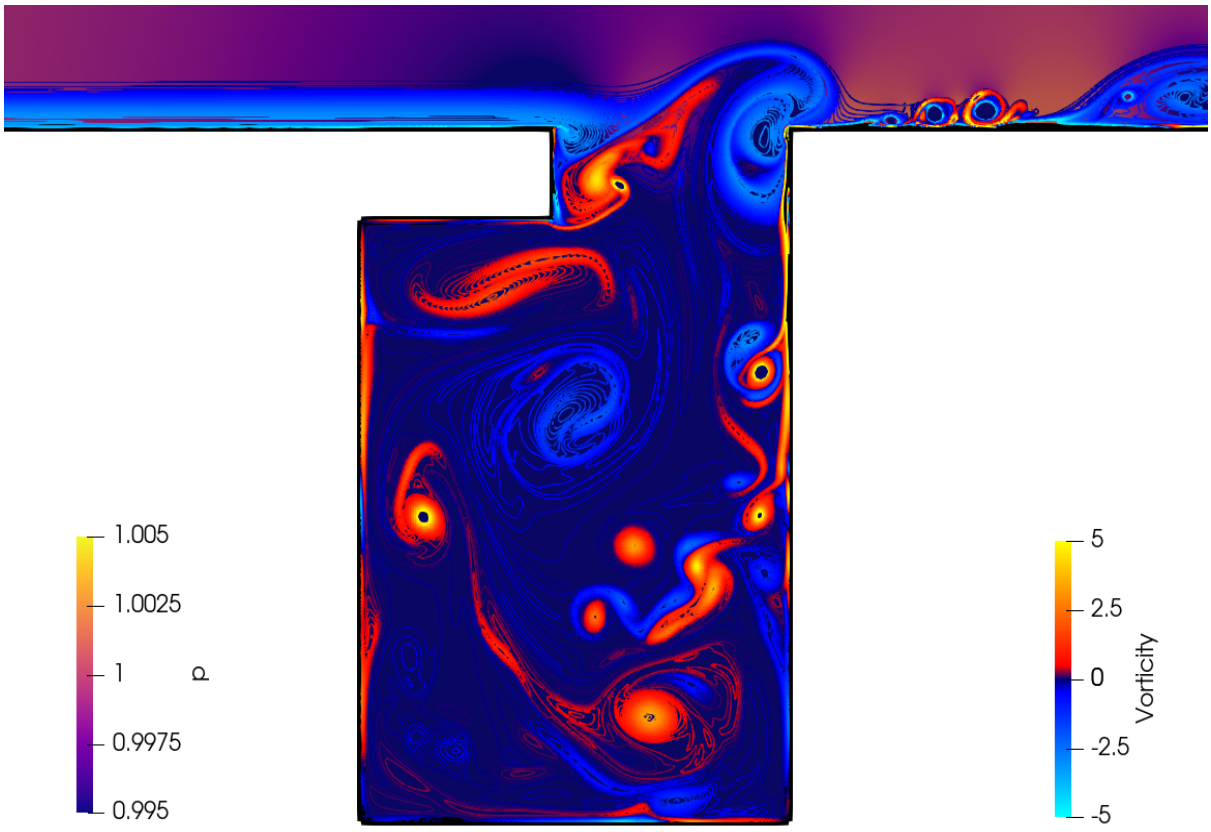

(a) Cavity expansion mode with vorticity contours in range [-5,5], t = 125.15

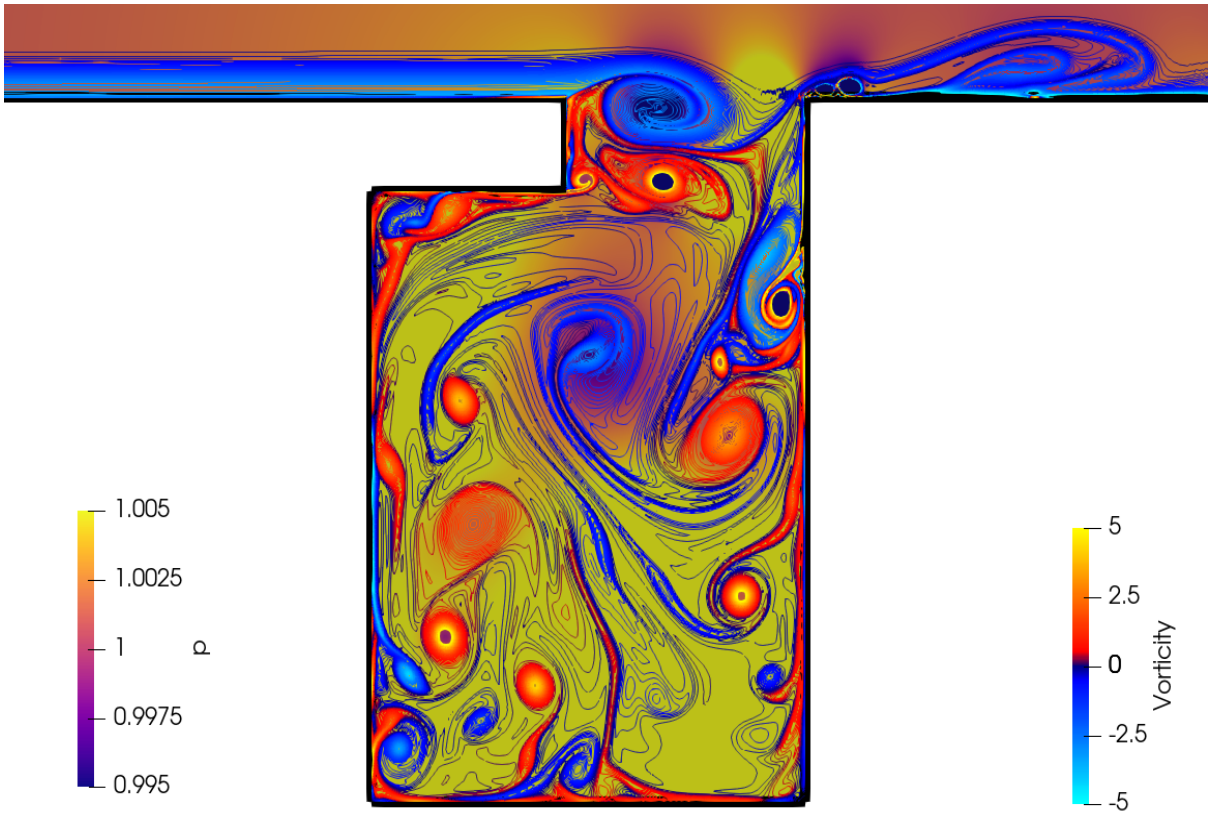

(b) Cavity compression mode with vorticity contours in range [-5,5], t = 126.50

Figure 7.17. Cavity expansion and compression modes

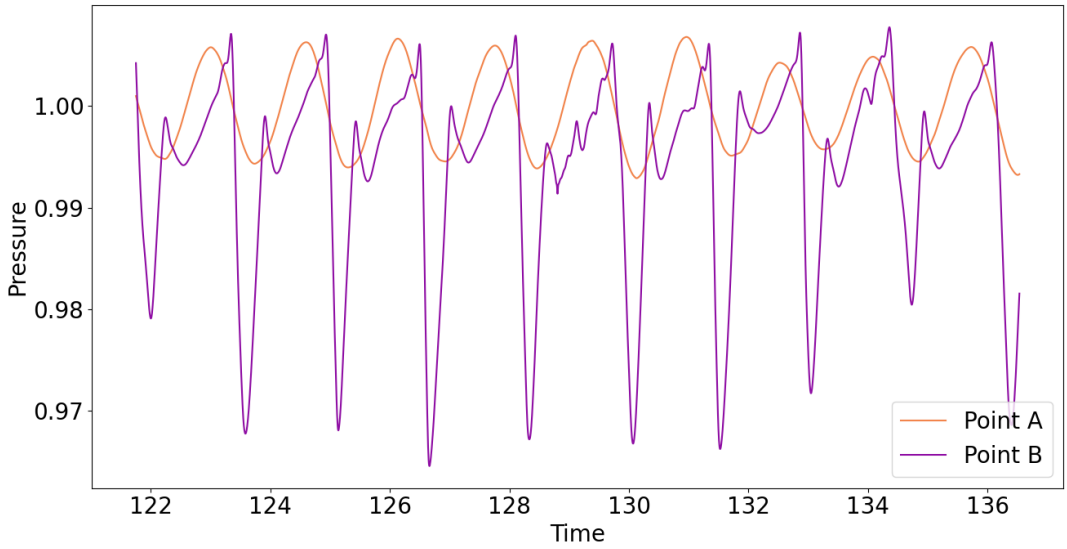

Figure 7.18. Time history of pressure fluctuations inside cavity

fluctuations inside the cavity at points A and B. The rapid increases and decreases, particularly those recorded at point B, exemplify the distinct expansion and compression phases of the shear layer oscillation cycle. The pressure fluctuations at point B clearly indicate that the flow is fully developed and the shear layer has reached a steady-state of oscillation, as the compression and expansion modes occur at regularly spaced intervals; however, the free stream fluid that impinges on point B introduces irregular fluctuations in the compression cycle. Point A, which is not subjected to the unsteady loading of the free stream fluid, displays a nearly perfect sinusoidal pressure oscillation. From point A, the shear layer oscillation frequency is obtained, and the corresponding Strouhal number is calculated as $S_t = 0.6533$, which is in excellent quantitative agreement with that reported by the participants of 0.65, yielding a percent error of approximately 0.51. The CFD results provided above verify the findings of Tam *et al.* and qualitatively validate the results of the simulation, thus enabling the validation of the CAA results to proceed.

The CAA validation process is begun by analyzing the acoustic waves generated by the oscillating shear layer, as shown in Figure 7.19. Figure 7.19*a* shows the acoustic pressure field generated by the expansion mode of Figure 7.17*a*. Acoustic waves can be seen emanating from the downstream cavity edge, with the vortices caused by the shear layer oscillation propagating downstream. As characterized by the expansion mode, a low pressure system is contained within the cavity. Conversely, a high pressure system is seen in Figure 7.19*b*, which shows the acoustic field produced by the compression mode in Figure 7.17*b*. From Figure 7.19, the effectiveness of the proposed boundary treatments is evaluated. As previously mentioned, polynomial adaptation was applied in the outflow direction, primarily in the

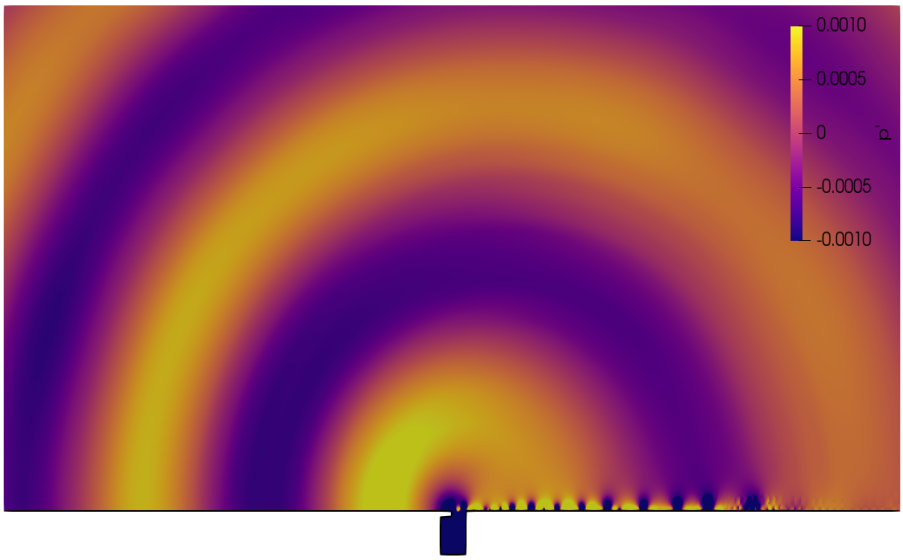

(a) Acoustic pressure, cavity expansion mode, t = 125.15

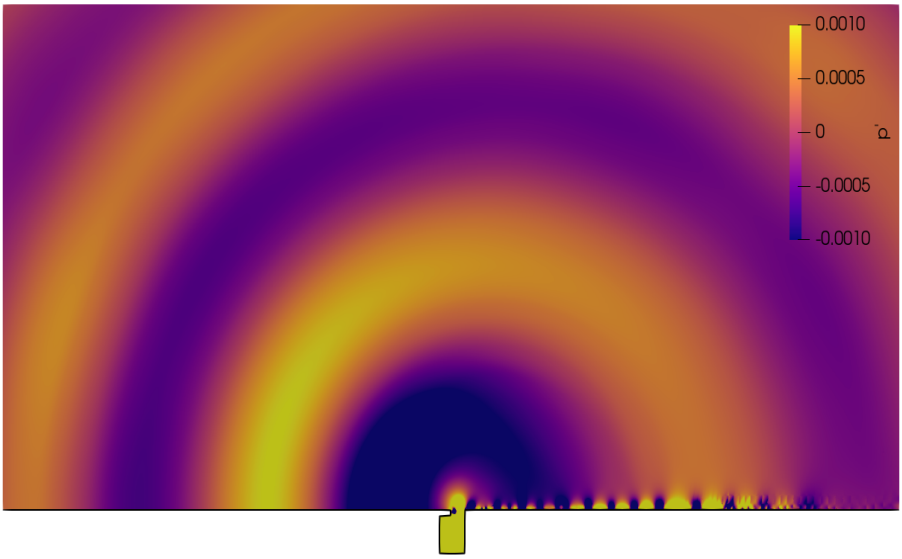

(b) Acoustic pressure, cavity compression mode, t = 126.50

Figure 7.19. Acoustic pressure contours for flow over a deep cavity

vicinity of the wall, as seen in Figure 7.14. Additionally, a large stretching ratio was applied exclusively in the $\mathcal{P}_1$ region to further reduce the outgoing vortices. The highly dissipative nature of the $\mathcal{P}_1$ elements, coupled with the reduced resolution provided by the polynomial adaptation and the increased friction resulting from the no-slip BC at the wall, quickly and effectively eliminate the outgoing vortices before encountering the outflow boundary. The absence of reflections produced at the outflow boundary validates the suitability of the applied boundary treatments for application in direct CAA methods.

As found by the Workshop's participants and visualized by Figures 7.19*a* and 7.19*b*, the directivity of the maximum acoustic pressure is angled upstream, indicating that the cavity noise will affect passengers in the front more than those in the rear seats. The noise generated by the oscillating shear layer is highly tonal in nature, evidenced by the considerable spike in the SPL shown in Figure 7.20, which plots the SPL and corresponding frequencies recorded at point A. The amplitude and frequency of the dominant tone seen in Figure 7.20 are recorded alongside the experimental values in Table 7.1. The simulation results are in good agreement with the experimental results, as both the frequency and amplitude of the dominant tone are within 6% of the experimental values; however, an important distinction must be made regarding the discrepancies. In addition to being conducted in 3D, the experiment also included a turbulent inflow boundary layer. The three-dimensional nature of the experiment enables the formation of stronger, more coherent vortices, resulting in a larger variation in pressure between the expansion and compression modes, thus increasing the acoustic intensity. Additionally, the presence of turbulence has been demonstrated to drastically reduce the frequency of tonal noise [30], and in cases of extreme turbulence intensity, eliminate the tonal noise completely. The disparate nature of the experimental configuration and that of the simulation elucidates the differences in the reported amplitudes and frequencies, thus establishing the validity of the FR method to be applied towards challenging, industrial-scale direct CAA applications.

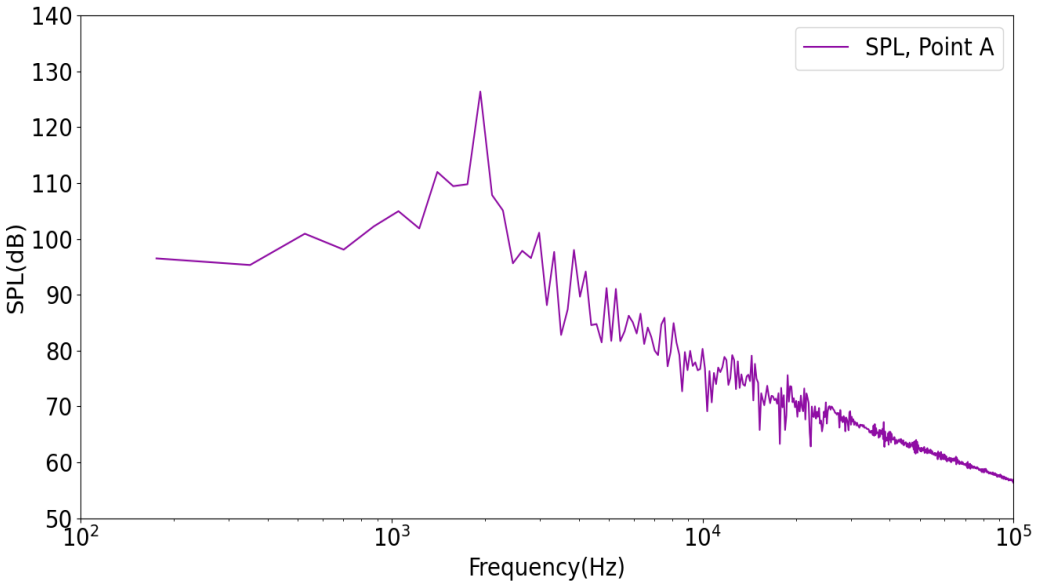

Figure 7.20. SPL of flow over a deep cavity

	Frequency (Hz)	Amplitude (dB)
Experimental results [59]	1824	134
Simulation results	1929.82	126.35

Table 7.1. Tonal frequency and amplitude of flow over a deep cavity

7.3 Discussion

The validation cases presented in the current Chapter were selected based on their possible merit firstly, to validate the ability of the FR method to accurately and efficiently capture the generation and propagation of acoustic waves, and secondly, to further substantiate that the FR method sufficiently resolves each of the computational challenges inherent to CAA.

The simple geometry and rudimentary flow conditions seen in the cylinder validation case establish a computationally inexpensive platform to visually and analytically validate the acoustic generation and propagation processes. The modest nature of the simulation permitted the extension of the domain well beyond the near-field limits. As seen in Figure 7.12, the acoustic waves are well resolved throughout the domain and propagate all the way to the extended boundaries. Additionally, the remarkable agreement between the slopes of the simulation data and the inverse-square law of decay, as shown in Figure 7.11, emphasize the non-dissipative and non-dispersive nature of the FR method, particularly at higher polynomial degrees, and provide further verification towards the second computational challenge of CAA, namely the accurate propagation of acoustic waves over large distances. Furthermore, the increased domain size authorized the implementation of each boundary treatment proposed in Chapter 6. The larger domain, combined with grid stretching, polynomial adaptation, and artificial viscosity, proved remarkably proficient at eliminating vortices before crossing the outflow boundary, without creating any spurious reflections. The exceptional performance of the applied boundary treatments facilitates the usage of Riemann invariant BCs, therefore maintaining generality as an applicable BC for both CFD and CAA simulations and providing additional verification to the fourth computational challenge of CAA.

The complex geometry and computationally demanding nature of the flow over the deep cavity simulation provide a convenient means to validate the application of the FR method towards challenging, industrial direct CAA applications while simultaneously exemplifying several of the computational challenges associated with CAA. Although not explicitly addressed in the previous section, the flow over a deep cavity produces acoustic waves spanning a wide range of frequencies, as visualized by examining the x-axis of Figure 7.20, which contains frequencies varying by several orders of magnitude. The frequencies at the higher ranges, which comprise the broadband noise produced by the cavity, are the

quintessential embodiment of the third numerical obstacle of CAA, specifically the resolution of compact, high-frequency waves.

The excellent agreement between the experimental and simulation data in the overall frequency content illustrates that the high-order $\mathcal{P}_5$ elements inside the cavity adequately resolve the high-frequency waves, providing additional verification towards the third numerical challenge of CAA. Furthermore, the turbulent nature of the flow produces vortices of varying lengths, as seen in Figure 7.17. The disparity in length scales is largely magnified by comparing the small length scales of the vortices in Figure 7.17 to the large acoustic wavelengths seen in Figure 7.19. This considerable disparity in length scales epitomizes the seconds conceptual challenge of CAA. Lastly, the inherent time dependence of CAA must be addressed. As previously stated, acoustic features are fundamentally time-dependent, which negates the application of turbulence models, such as RANS, which utilize time-averaging. For low-order numerical methods, this poses a formidable challenge as the number of elements required for sufficient resolution of the flow becomes impractically large; however, the large element sizes afforded by the high-order polynomial, coupled with the FR method's efficient operation on modern hardware permit the application of DNS while keeping the simulation run time moderately low.

With the validation of the FR method as a direct CAA approach thoroughly and comprehensively demonstrated, in addition to the supplemental verification of each of the computational challenges of CAA, the application of the FR method as a direct near-field CAA method is commenced in the following Chapter by conducting numerical simulations of two and three-dimensional NACA0012 airfoils at varying angles of attack.

Chapter 8

Application

Historically, noise generated from isolated airfoils was assumed to originate primarily from the turbulent wake behind the airfoil and therefore was considered broadband in nature [63]. In a thorough series of wind tunnel experiments of NACA0012 airfoils subject to varying flow speeds and angles of attack, Paterson *et al.* [64] identified the existence of distinct tonal noises. The presence of the tones was strongly correlated to the flow speed and the angle of attack, α, as only specific flow configurations produced tonal noises. Paterson *et al.* define the region where tones were detected as the tonal envelope and determined that within the tonal envelope, the frequencies increase proportionally to the free stream velocity [64]

$$\omega = \frac{0.011\vec{V}_{\infty}^{1.5}}{\sqrt{C_0 \nu}}, \tag{8.1}$$

where ν is the kinematic viscosity of the fluid. Paterson *et al.* were unable to isolate the source of the tonal noises but postulated that a vortex shedding phenomenon located downstream of the trailing edge was responsible [1, 64]. Since Paterson *et al.* discovered the existence of tonal noises, many theories have been presented regarding their origin. For the sake of brevity, only theories which differ significantly are presented below.

Tam [63] was the first to dispute the findings of Peterson *et al.* and argued that tonal noises were due to a self-excited feedback loop of aerodynamic origin [63]. Tam's theory suggests that acoustic disturbances, generated by the flow over the airfoil's sharp trailing edge, propagate downstream within the wake. The chaotic nature of the wake amplifies the acoustic disturbances until they are sufficiently large so as to introduce lateral oscillations, resulting in the emission of acoustic waves [1, 63]. The acoustic waves propagate upstream and cause instabilities in the airfoil's boundary layer on the pressure surface, thus completing the feedback loop.

Arbey *et al.* [65] provided a similar theory to Tam's in that a self-excited feedback loop is responsible for the generation of the tonal noises; however, Arbey *et al.* suggest that hydrodynamic instabilities in the boundary layer propagate over the trailing edge, thus generating acoustic waves. These acoustic waves propagate upstream along the airfoils suction surface to the initial location where the hydrodynamic instabilities are created, therefore closing the feedback loop [1, 65]. Arbey *et al.* 's theory disagrees with Tam's both in the closure location of the feedback loop as well as the location and mechanism of acoustic generation.

Nash *et al.* [66] disagreed with both Arbey *et al.* and Tam and suggested that a vortex shedding process was responsible for generating the tones [1, 66]. Nash *et al.* proposed that boundary layer instabilities in the form of Tollmien-Schlichting (T-S) waves propagate along the airfoil towards the trailing edge. Before reaching the trailing edge, the T-S waves roll up into vortices, which then convect over the trailing edge and create acoustic waves [66]. The acoustic waves, oscillating at the same frequency as the T-S waves, propagate upstream to the point on the suction surface of the airfoil where the boundary layer becomes unstable and completes the feedback loop [1, 66]. Nash *et al.* 's theory agrees with Arbey and establishes the trailing edge as the location where the acoustic waves are generated. However, Nash's theory contradicts both Arbey's and Tam's theories regarding the acoustic generation mechanism.

The experimental results of Paterson [64], Tam [63], Arcondoulis [1], and Arbey [65] are presented in Figure 8.1, where the filled markers denote the presence of a distinct tone, and the un-filled markers indicate the absence of a distinct tone. The majority of tonal noises were recorded within the tonal envelope, as predicted by Paterson [64].

The objective of the current Chapter is not to refute any of the aforementioned theories regarding tonal noise generation, but rather, to provide supplemental evidence on the presence of tonal noises by performing direct CAA simulations with the FR method of a NACA0012 airfoil, subject to multiple angles of attack, corresponding to locations both inside and outside the predicted tonal envelope. Additionally, the boundary treatments discussed in the previous Chapters are implemented, and their viability toward real-world CAA applications are assessed.

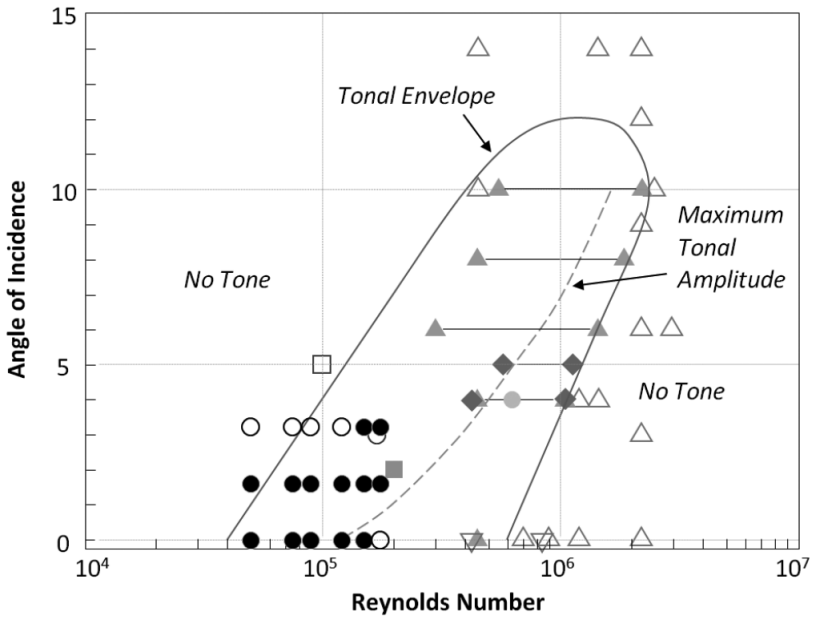

Figure 8.1. Predicted tonal envelope of NACA0012 [1]

8.1 2D NACA0012 Airfoil

8.1.1 Computational Details

As seen in Figure 8.1, the tonal envelope spans a wide range of Reynolds numbers, with distinct tones detected up to $R_e \approx 2 \times 10^6$. To minimize computational costs, all simulations presented in this Chapter were performed at a R_e of 5×10^4, corresponding to the lower limit of the tonal envelope. To verify the dependence of the angle of attack on the tonal noise generation, the simulations were performed at $\alpha = 0°,\ 2.5°,\ 5°$, and 7.5°, with a M_a, P_r, and γ of 0.4, 0.71, and 1.4, respectively.

The leading edge of the NACA0012 airfoil, with chord length, c_h, of unity, is centered at the origin and used to non-dimensionalize all lengths. The computational domain extends $5c_h$ from the airfoil in all directions, with the outflow boundary extended to $20c_h$ to provide sufficient space for the application of the boundary treatments. The computational domain was discretized using an unstructured mesh containing 42,291 quadrangular and triangular elements, as seen in Figure 8.2*a*, which displays the acoustic region of the computational domain. To ensure sufficient resolution of all potential acoustic sources, the wake and boundary layer regions of the mesh contain structured, quadrangular elements, as shown in Figure 8.2*b*. The same mesh shown in Figure 8.2 was used for all simulations; however, the structured wake region was inclined according to the applied angle of attack.

Although the exact location of the feedback loop responsible for the generation of tonal noises is unknown, all theories presented in the previous section agree that it begins in the vicinity of the trailing

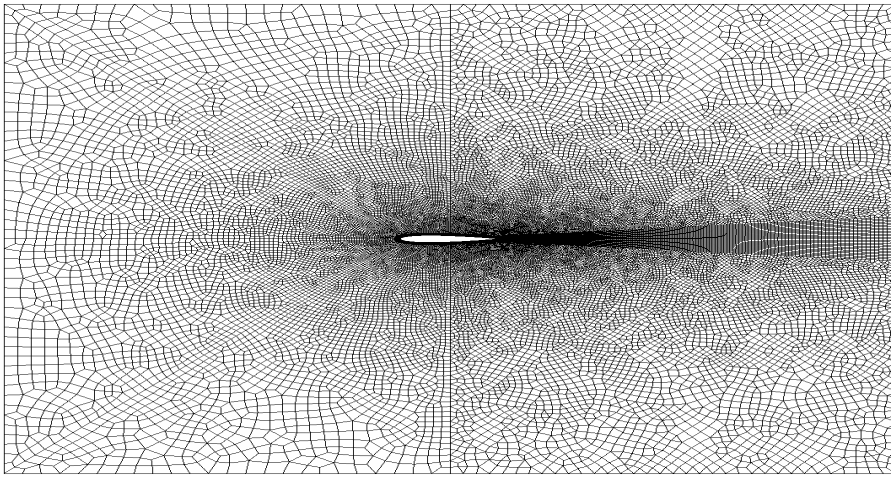

(a) Acoustic region

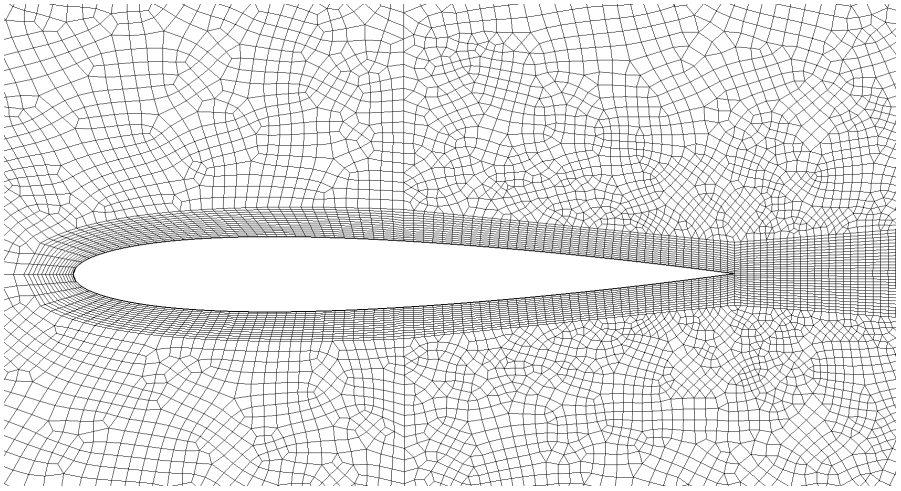

(b) Boundary layer region

Figure 8.2. NACA0012 computational mesh

edge; therefore, the P-ERK time-stepping scheme was applied, with increased RK stages in the immediate vicinity of the trailing edge and boundary layer regions, as seen in Figure 8.3. To avoid capturing any transient solutions, the simulations were progressed for 75 convective time steps before taking any data measurements, after which the simulations were progressed for another 75 convective time steps in which data was recorded.

The unsteady nature of flow over an airfoil, particularly at high angles of attack, necessitates high levels of accuracy to properly resolve all flow features, and as such, the acoustic region is comprised exclusively of $\mathcal{P}_5$ elements. In addition to reducing computational costs, polynomial adaptation was applied along the boundaries to attenuate outgoing acoustic waves, as seen in Figure 8.4. To prevent vortices from crossing the outflow domain and potentially corrupting the solution by introducing spurious reflections, artificial viscosity was applied in the outflow direction. Additionally, a moderate stretching ratio of 1.03 was applied near the outflow boundary to dissipate any remaining vortices further.

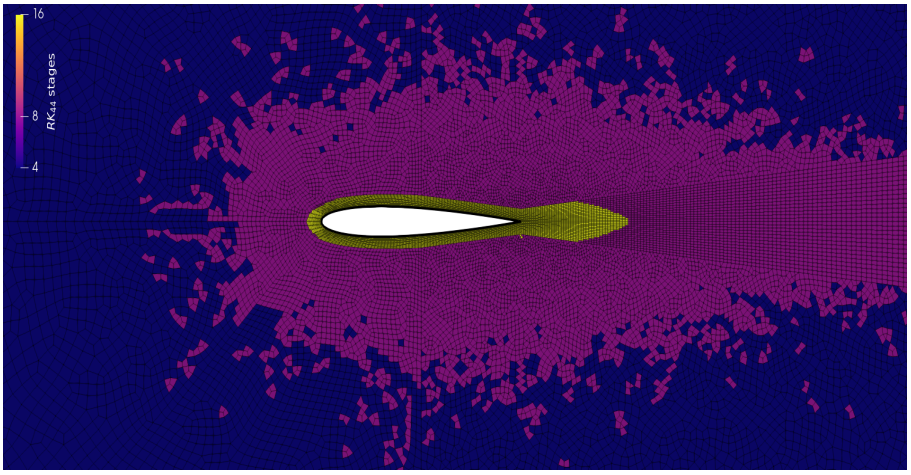

Figure 8.3. NACA0012 P-ERK timelevels

Figure 8.4. NACA0012 boundary treatments

Lastly, the location of the data sampling points is presented in Figure 8.5, with 359 equally spaced points on the dashed circle of radius two centered around the trailing edge of the airfoil.

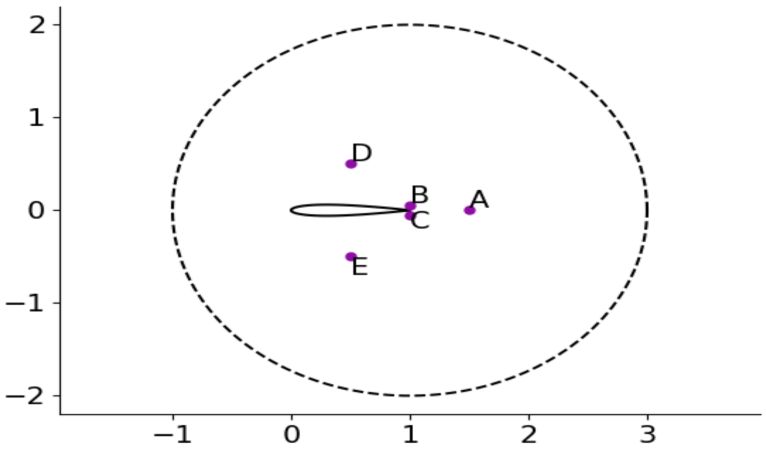

Figure 8.5. NACA0012 data sampling points

8.1.2 Results, $\alpha = 0°$

In addition to the validation cases presented in the previous Chapter, Vermeire *et al.* [34, 39, 47, 67], Witherden *et al.* [27, 43, 68] and Pereira [54, 55] have demonstrated that the FR method, particularly when applied with high order polynomials, produces highly accurate CFD results. Therefore only the CAA results are assessed in the current Chapter.

After a sufficiently long time, such that all initial and transient solutions are removed from the flow, extremely small-scale instability waves begin to develop in the boundary layer of the airfoil. The streamlined profile of the NACA0012 airfoil enables the gradual amplification of these disturbance waves, which become sufficiently strong so as to cause large scale oscillations in the wake, as illustrated by the vorticity contours in Figure 8.6. At zero degrees angle of attack, vortices are periodically shed from both the pressure and suction sides of the airfoil, creating a perfectly symmetrical wake, as shown in Figure 8.7. The airfoil's sharp trailing edge provides an efficient diffraction mechanism [1], which generates an acoustic wave as each vortex convects over the trailing edge. The acoustic waves, also pictured in Figure 8.7, emanate from the trailing edge of the airfoil and propagate radially in all directions.

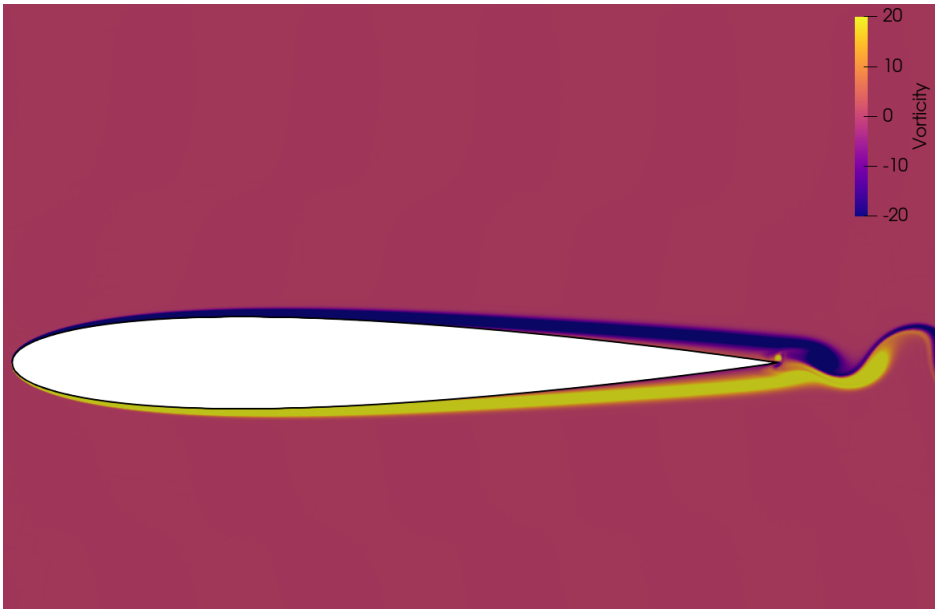

Figure 8.6. Vorticity contours of NACA0012 airfoil, $\alpha = 0°$

The instantaneous, time-averaged, and acoustic pressure fields generated by the NACA0012 airfoil at 150 convective time steps are shown in Figure 8.8. Recalling that the acoustic pressure is obtained by removing the time-averaged pressure field from the instantaneous pressure field, the acoustic field's derivation is easily recognized. Additionally, the influence of the Doppler effect is readily visualized by Figure 8.8*c*, which distinctly illustrates the compression of acoustic waves traveling upstream and the

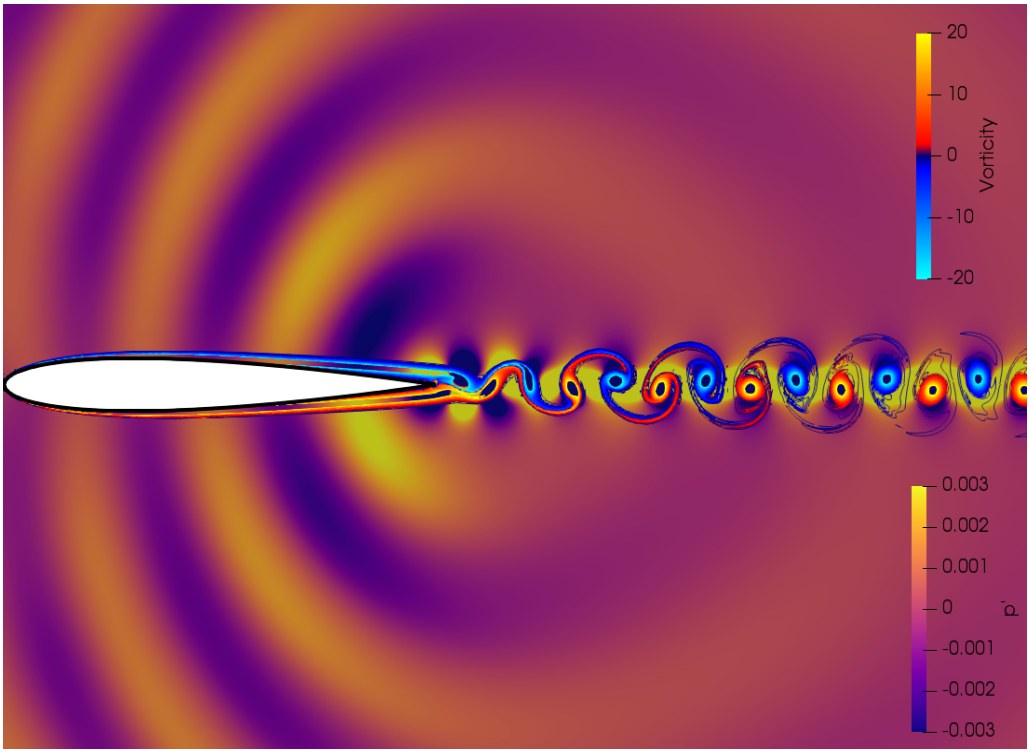

Figure 8.7. NACA0012 acoustic pressure and vorticity contours, $\alpha = 0°$

expansion of those traveling downstream.

The directivity of the acoustic pressure, recorded along a circle of radius two centered at the trailing edge of the airfoil, is presented in Figure 8.9. The directivity and magnitude are in good agreement with those reported by Sandberg *et al.* in their investigation on airfoil self-noise at identical flow conditions as presented in this section, with the maximum amplitude varying by less than 2dB.

Lastly, the power spectral density (PSD) of the acoustic pressure, recorded at points D and E, is plotted in Figure 8.10. From the enlarged section of Figure 8.10, a distinct peak in the PSD of the acoustic pressure at both points D and E is clearly visible. This peak is tightly centered around a small range of frequencies, indicating the presence of tonal noise. The current combination of R_e and α lies within Paterson's predicted tonal envelope [64], and the existence of tonal noises is experimentally confirmed by Acrondoulis [69]. Additionally, both Sandberg *et al.* [50] and Jones *et al.* [70] report the presence of tonal noise in their numerical simulations. From Figure 8.10, it appears a multitude of tonal frequencies are present; however, these spikes in the PSD occur exclusively at integer multiples of the first frequency, clearly indicating that the first spike in Figure 8.10 is the fundamental frequency while every other spike is simply a harmonic of the fundamental frequency. Lastly, the symmetry of the acoustic field can be further recognized from Figure 8.10, as the PSD of the acoustic pressure above and below the airfoil are identical in both frequency and magnitude.

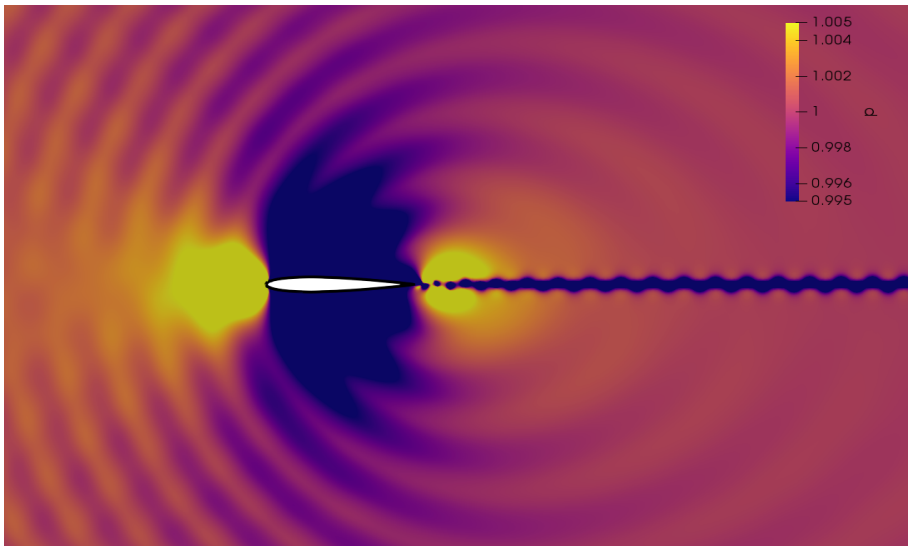

(a) Instantaneous pressure field

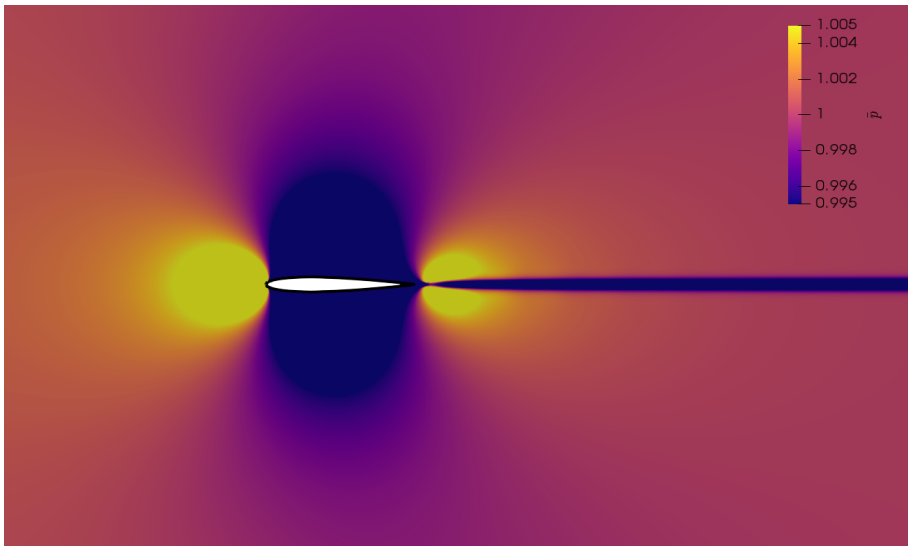

(b) time-averaged pressure field

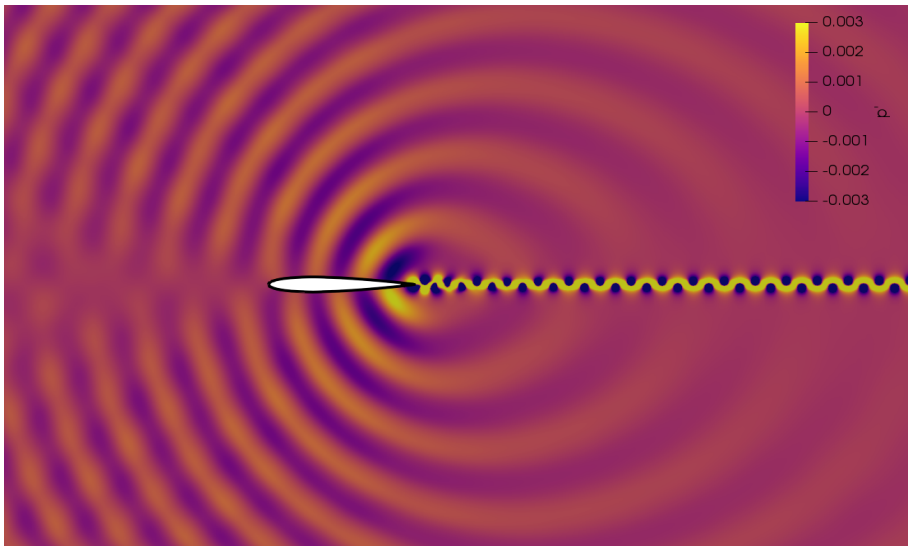

(c) Acoustic pressure field

Figure 8.8. NACA0012 instantaneous, time-averaged, and acoustic pressure fields, $\alpha = 0°$

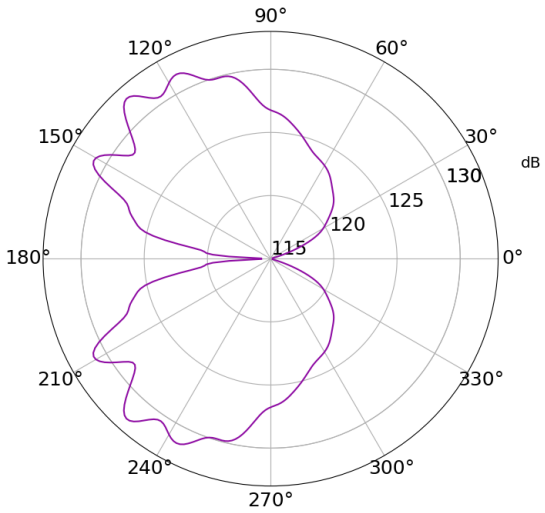

Figure 8.9. NACA0012 RMS acoustic pressure directivity at R = 2, $\alpha = 0°$

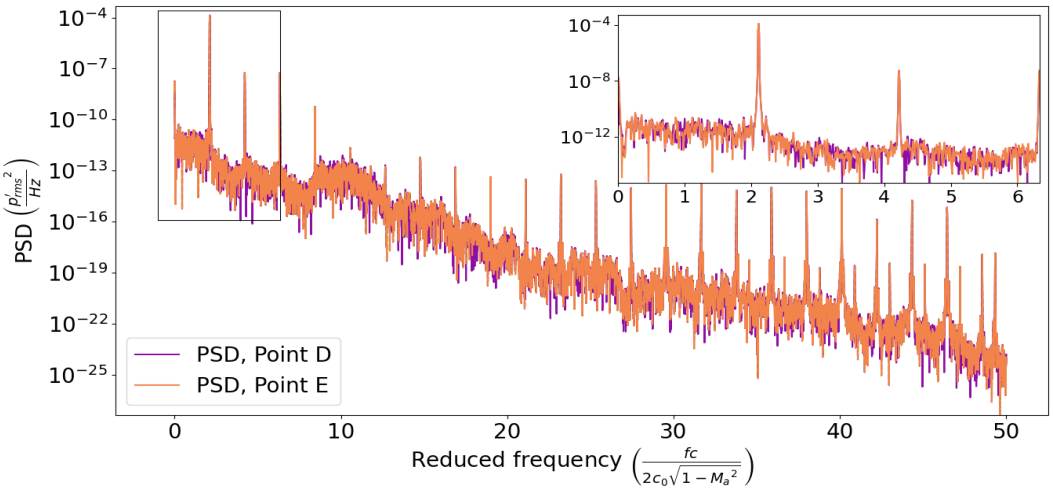

Figure 8.10. NACA0012 PSD of acoustic pressure in free stream, Points D and E, $\alpha = 0°$

At zero degrees angle of attack, the presence of a distinct tonal noise is readily identified. The following section investigates the generation of tonal noises at an angle of attack of 2.5°.

8.1.3 Results, α = 2.5°

Increasing the angle of attack from 0° to 2.5° alters the development of the hydrodynamic flow field, and consequently, the generation of acoustic waves. The disparities in the hydrodynamic flow field are visualized by Figure 8.11, which illustrates the vorticity contours in the vicinity of the trailing edge of the airfoil. The slight inclination of $\alpha = 2.5°$ facilitates the development of a laminar boundary layer along the entire pressure surface of the airfoil. The boundary layer on the suction surface of the airfoil, however,

is subjected to an adverse pressure gradient, causing the boundary layer to temporarily separate from the airfoil and reattach shortly after, as illustrated in Figure 8.11. The separation and reattachment of the boundary layer generate compact vortices, which then propagate over the trailing edge and generate acoustic waves, as shown in Figure 8.12, which contains vorticity contours surrounding the airfoil and the corresponding acoustic pressure field.

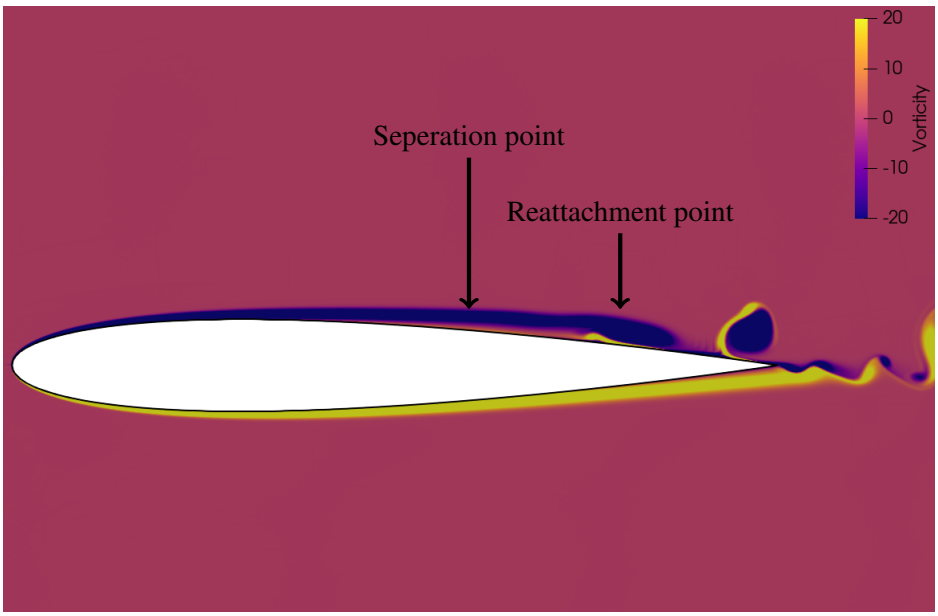

Figure 8.11. Vorticity contours of NACA0012 airfoil, $\alpha = 2.5°$

The disparate development of the boundary layers on the pressure and suction surfaces of the airfoil results in the generation of an asymmetrical wake, as evidenced by Figure 8.12. The pressure gradient along the suction surface of the airfoil generates the large-scale, periodically shed vortices; however, the pressure gradient is insufficiently large to generate complete boundary layer separation, thus resulting in a quasi-laminar boundary layer on the suction surface of the airfoil. The laminar boundary layer on the pressure surface of the airfoil convects over the trailing edge and combines with the fluctuating boundary layer of the suction surface to generate the small scale vortices seen in Figure 8.12. Although applying an angle of attack significantly alters the vortex generation procedure, the acoustic generation procedure remains the same. The propagation of the large-scale vortices over the suction surface trailing edge generates an acoustic wave, which propagates radially from the trailing edge, as shown in Figure 8.12. The vortices generated by the separation of the boundary layer are far more compact than those produced at an α of 0°, and therefore are more efficient radiators of sound. This is best visualized by comparing the amplitudes of the acoustic waves in Figure 8.7 to those in Figure 8.12.

Figure 8.13 displays the instantaneous, time-averaged, and acoustic pressure fields of the NACA0012 airfoil, recorded at 150 convective time steps. The effects of the applied angle of attack are clearly

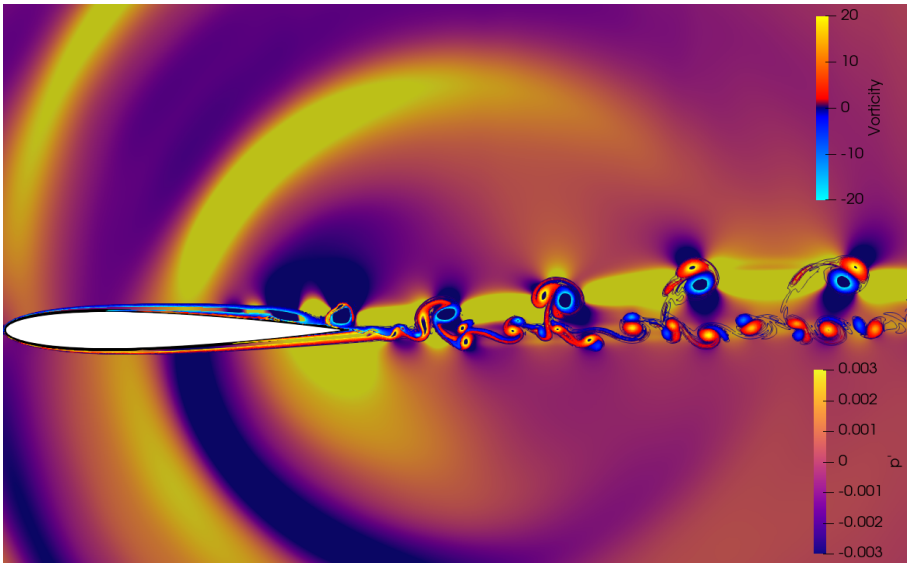

Figure 8.12. NACA0012 acoustic pressure and vorticity, $\alpha = 2.5°$

visible in Figure 8.13*b*, as the time-averaged pressure along the airfoil is not symmetric about the x-axis. Additionally, the acoustic waves, which are again calculated by subtracting the time-averaged pressure from the instantaneous pressure, are generated at a considerably lower frequency than at an α of 0°, as shown in Figure 8.13*c*. Contrary to $\alpha = 0°$, where vortices are periodically shed from both the suction and pressure surfaces of the airfoil, at $\alpha = 2.5°$, only the large scale vortices on the suction surface of the airfoil generate acoustic waves, thus reducing the frequency at which acoustic waves are generated.

As stated above, the compact vortices on the suction surface of the airfoil efficiently radiate sound as they propagate over the trailing edge of the airfoil. This is epitomized by the directivity plot of the acoustic field, as shown in Figure 8.14, which clearly illustrates that increasing the angle of attack by 2.5° yields roughly a 6 dB increase in the maximum acoustic pressure. In addition to a larger acoustic magnitude, the directivity plot in Figure 8.14 is considerably smoother than at $\alpha = 0°$.

Finally, the PSD of the acoustic pressure, recorded at points D and E, is presented in Figure 8.15. The plots in Figure 8.15 are similar to those at $\alpha = 0°$, as shown in Figure 8.10, in that there exists a definitive spike in the PSD, clustered around a narrow band of frequencies, indicating the presence of tonal noise. Dissimilar to $\alpha = 0°$, however, is the inclusion of a multitude of tones with diminished amplitudes, as compared to the maximum tonal value. The amplitude of the primary tone is sufficiently larger than those of the auxiliary tones, suggesting the generation of a distinct tonal noise coupled with indistinct broadband noise. Lastly, further emphasis is placed on the efficiency of the suction surface vortices as acoustic generation mechanisms by noting the maximum amplitude in Figure 8.15 is roughly an order of magnitude larger than the maximum amplitude of Figure 8.10.

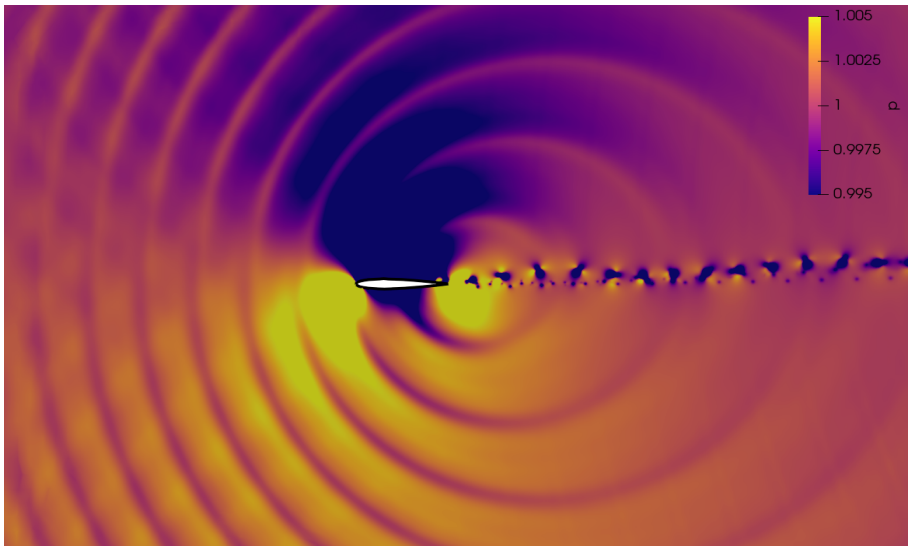

(a) Instantaneous pressure field

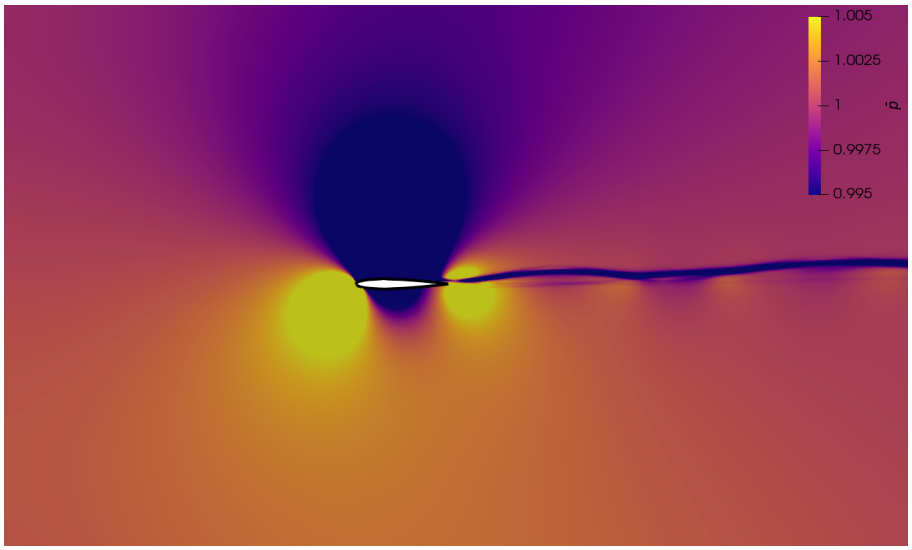

(b) time-averaged pressure field

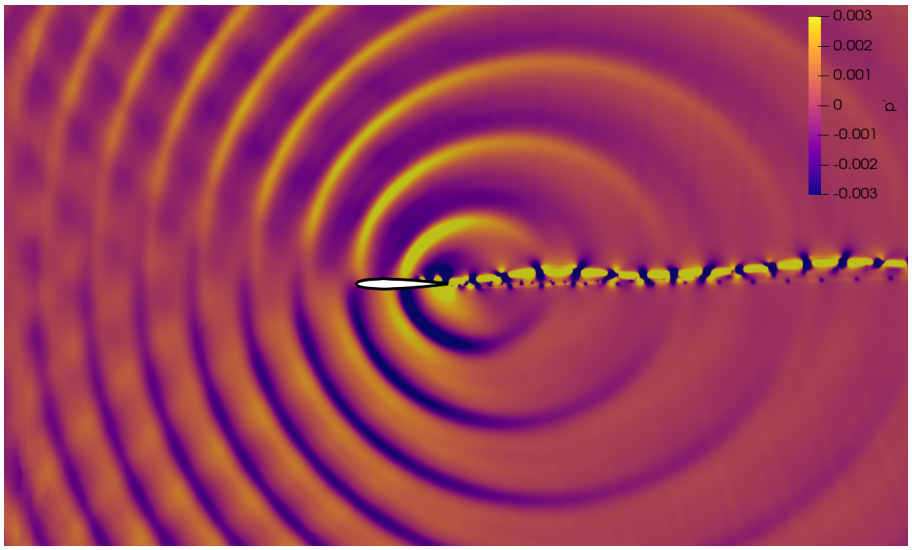

(c) Acoustic pressure field

Figure 8.13. NACA0012 instantaneous, time-averaged, and acoustic pressure fields, $\alpha = 2.5°$

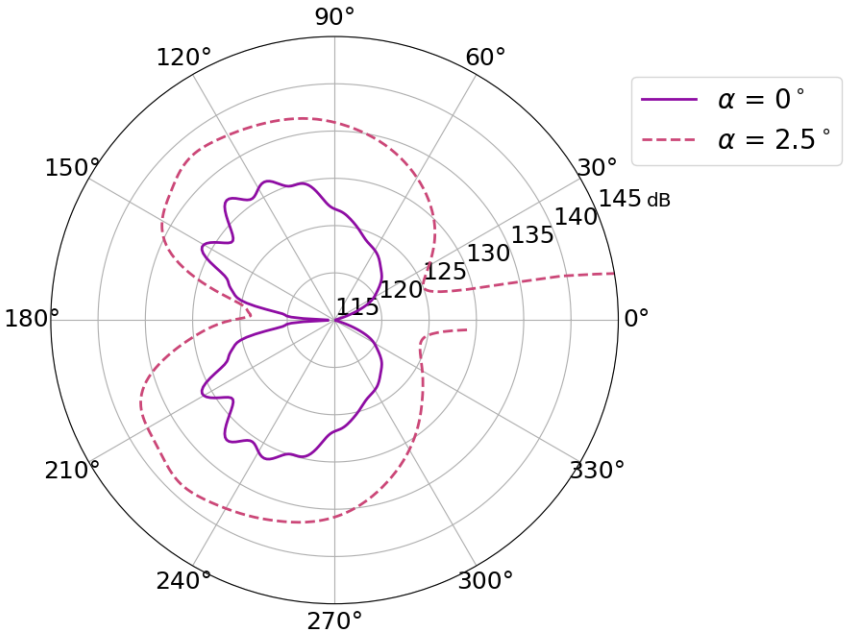

Figure 8.14. NACA0012 RMS acoustic pressure directivity recorded at R = 2, α = 2.5°

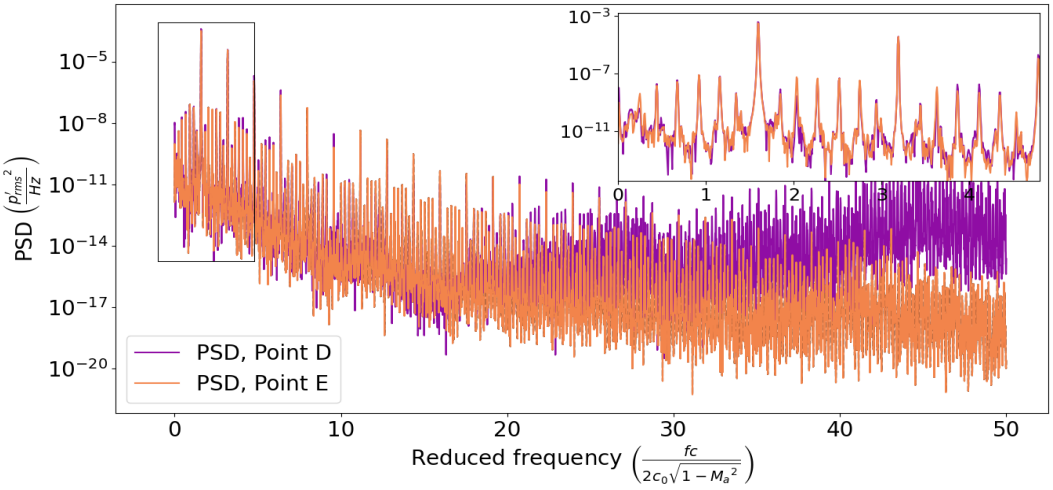

Figure 8.15. NACA0012 PSD of acoustic pressure in free stream, Points D and E, α = 2.5°

8.1.4 Results, α = 5°

The development of the hydrodynamic flow features responsible for the generation of acoustic waves is exacerbated as the angle of attack of the NACA0012 airfoil is increased from 2.5° to 5°, as seen in Figure 8.16, which contains the vorticity contours in the immediate vicinity of the airfoil. The boundary layer on the pressure surface of the airfoil is unaffected by the angle of attack and develops in a laminar fashion along the entirety of the airfoil. The heightened angle of attack significantly increases the pressure

gradient on the suction surface of the airfoil and shifts the location of the boundary layer separation and reattachment points upstream. The increased pressure gradient at $\alpha = 5°$ enables greater separation of the boundary layer from the airfoil surface, generating stronger, more coherent vortices as the boundary layer re-attaches to the airfoil surface.

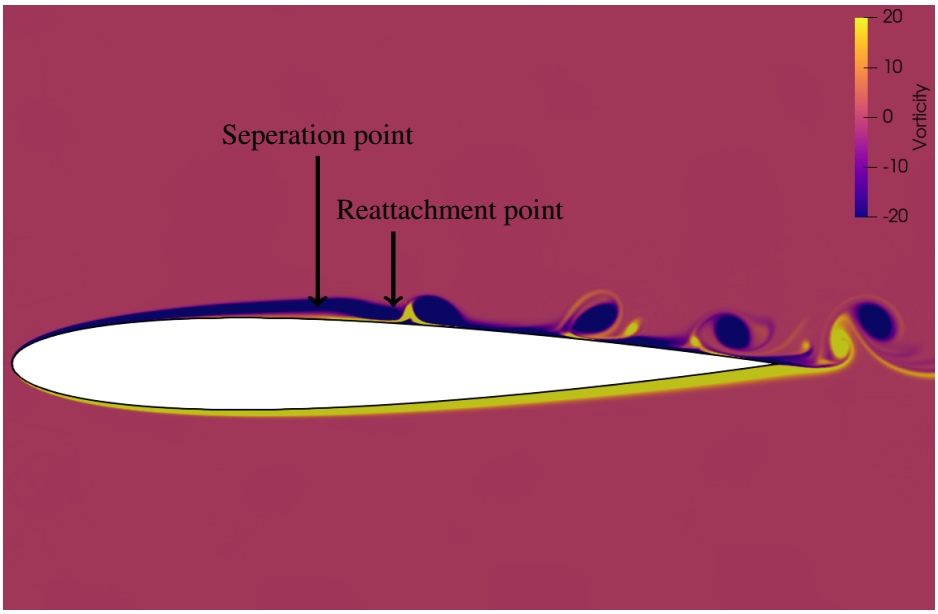

Figure 8.16. Vorticity contours of NACA0012 airfoil, $\alpha = 5°$

As previously detailed, the vortices resulting from the separation and reattachment of the boundary layer propagate over the trailing edge of the airfoil and generate acoustic waves, as shown in Figure 8.17, which contains both the vorticity and corresponding acoustic pressure contours. This process is confirmed as the primary source of acoustic generation, as acoustic waves exclusively radiate from the trailing edge.

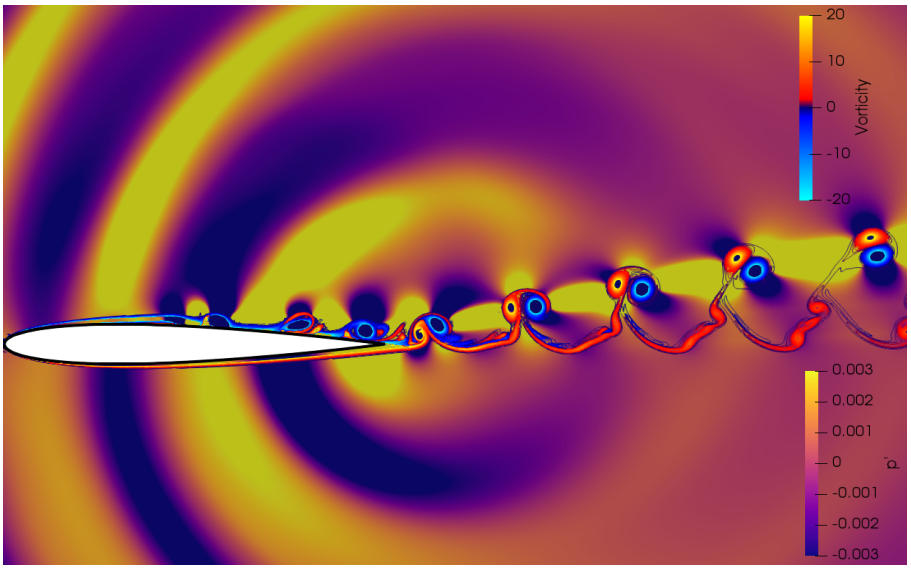

Figure 8.17. NACA0012 acoustic pressure and vorticity, $\alpha = 5°$

The instantaneous, time-averaged, and acoustic pressure fields of the NACA0012 airfoil at $\alpha = 5°$ are presented in Figure 8.18, providing insight into the derivation of the acoustic field. In addition to the induced asymmetry of the flow, the high-lift condition characteristic of large angles of attack is epitomized by Figure 8.18*b*. As seen by comparing Figures 8.11 and 8.16, increasing the angle of attack forces the boundary layer separation and reattachment points closer together and subsequently increases the vortex shedding frequency, as visualized in Figure 8.18*c*.

The directivity of the acoustic pressure is presented in Figure 8.19. The magnitude of the acoustic pressure at $\alpha = 5°$ is quite similar to that at $\alpha = 2.5°$, with the maximum amplitude varying by a few decibels. The directivity of the acoustic waves, however, is quite different. The top half of the directivity plot contains a large lobe, almost 140 dB in magnitude, inclined upstream at a steep angle. The bottom half of the directivity plot does not contain this singular lobe but rather several smaller lobes occurring at various angles and slightly lesser amplitudes. Contrary to the $\alpha = 0°$ and $2.5°$ simulations, which yield almost perfectly symmetrical directivity plots, the asymmetry of the $\alpha = 5°$ directivity plot implies that the airfoil noise will be heard differently depending on which side of the airfoil the observer is located. The asymmetry of the acoustic directivity is confirmed by Sanberg *et al.* [50].

Lastly, the PSD of the acoustic pressure, recorded at points D and E, is shown in Figure 8.20. As seen in the enlarged view in the top right corner, the maximum amplitude occurs a single spike, centered around a single frequency. Although similar in nature to the results of the previous simulations, the maximum amplitude is insufficiently predominant to classify as tonal noise, indicating that the airfoil noise of a NACA0012 airfoil at $\alpha = 5°$ is broadband in nature. This agrees well with Paterson's predicted tonal envelope [69], as the combination of $R_e = 50{,}000$ and $\alpha = 5°$ lies well beyond the limits of the envelope.

The following section investigates the acoustic characteristics of a NACA0012 airfoil as it approaches stall by increasing the angle of attack to 7.5°.

8.1.5 Results, $\alpha =$ 7.5°

As previously stated, increasing the angle of attack shifts the boundary layer separation and reattachment points towards the leading edge of the airfoil. At $\alpha = 7.5°$, both the separation and reattachment points are located upstream of the maximum airfoil thickness, as seen in Figure 8.21, which contains vorticity contours over the airfoil. The adverse pressure gradient, induced by the high angle of attack, prohibits the boundary layer from returning to a quasi-laminar state after the reattachment point, resulting in a wholly turbulent boundary layer on the suction surface of the airfoil.

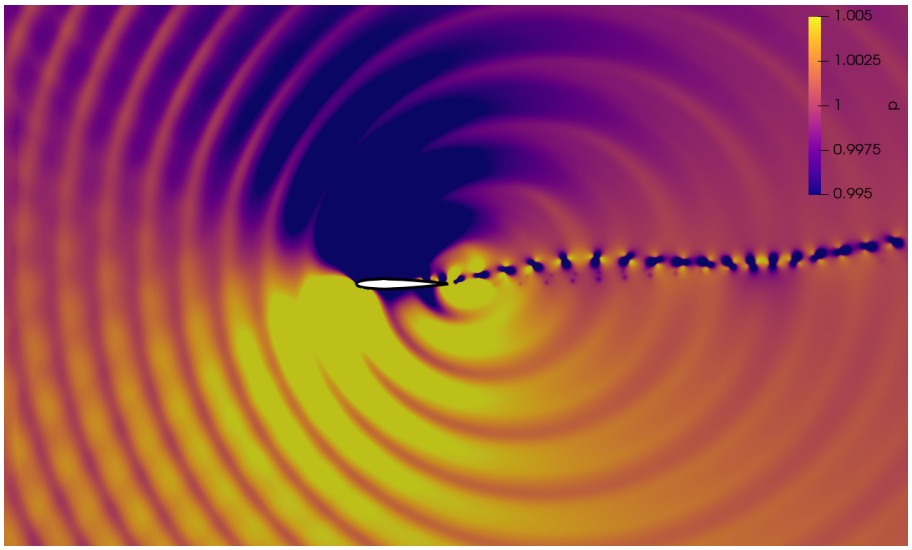

(a) Instantaneous pressure field

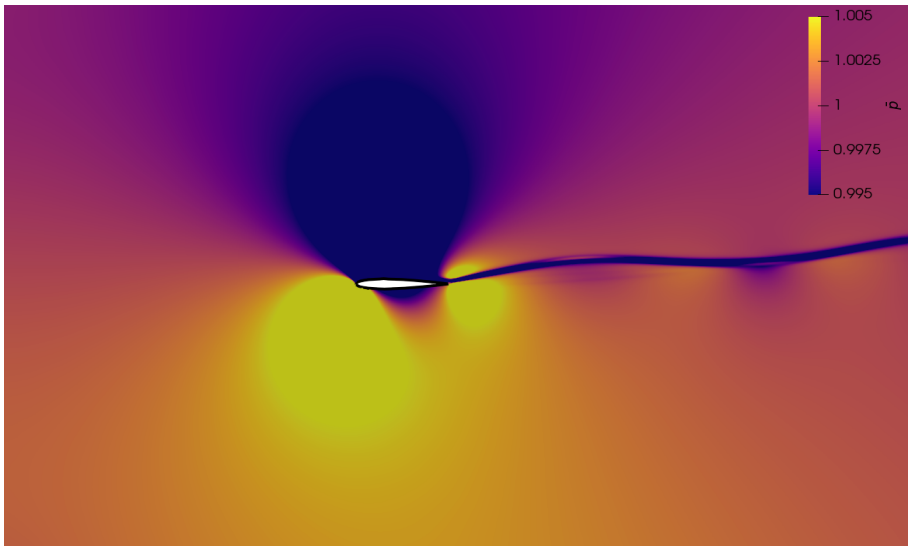

(b) time-averaged pressure field

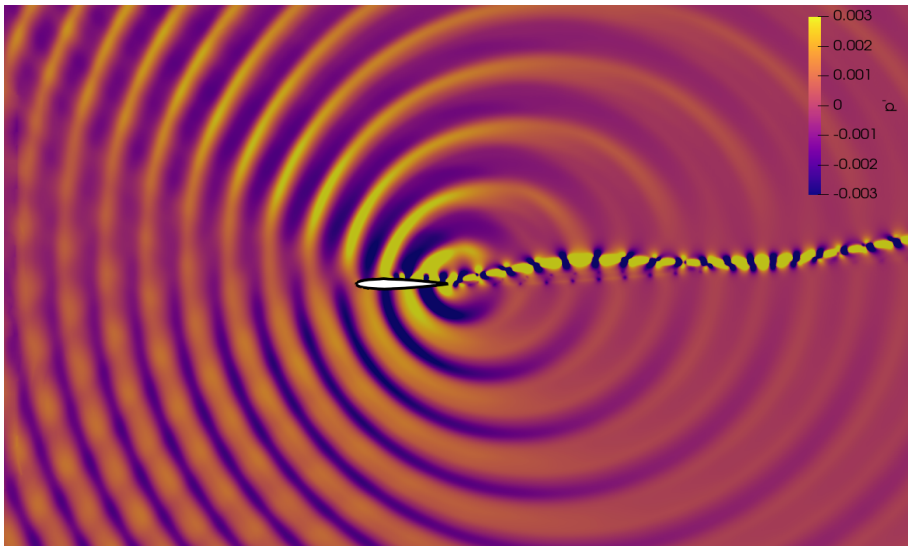

(c) Acoustic pressure field

Figure 8.18. NACA0012 instantaneous, time-averaged, and acoustic pressure fields, $\alpha = 5°$

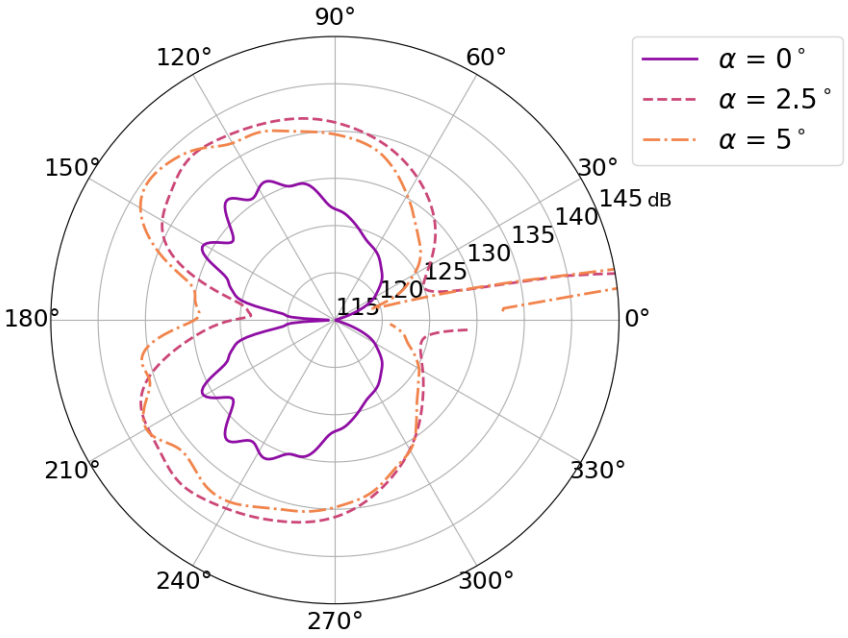

Figure 8.19. NACA0012 RMS acoustic pressure directivity recorded at R = 2, $\alpha = 5°$

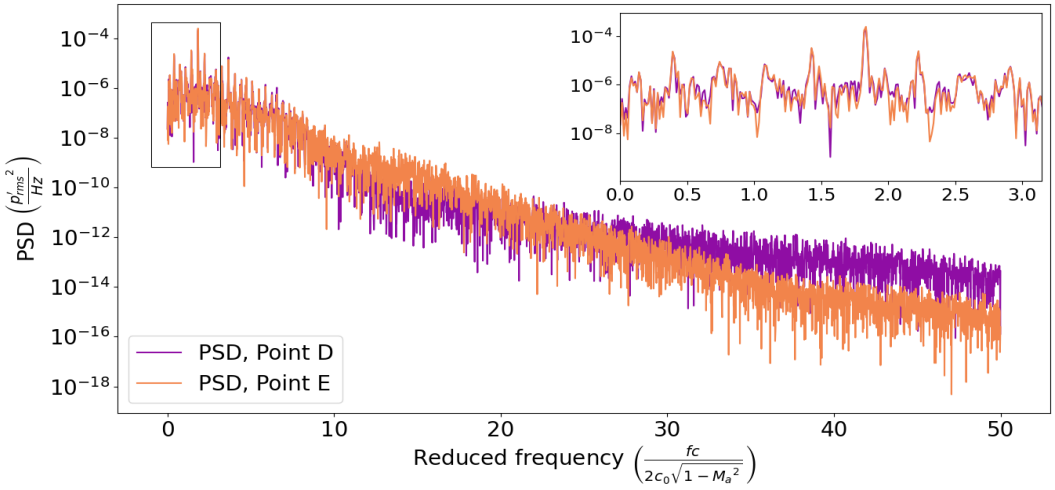

Figure 8.20. PSD of acoustic pressure in free stream, Points D and E, $\alpha = 5°$

From Figure 8.22, which contains vorticity and acoustic pressure contours, the effect of the turbulent boundary layer on the acoustic generation process is visualized. First, the vortices propagating over the trailing edge are completely devoid of any periodicity, resulting in irregularly produced acoustic waves. Additionally, the vortices tend to combine into large groups, generating acoustic waves of exceedingly large wavelengths as they propagate over the trailing edge. This behavior is captured in Figure 8.22, as the acoustic waves on the pressure side of the airfoil span almost half the chord length of the airfoil.

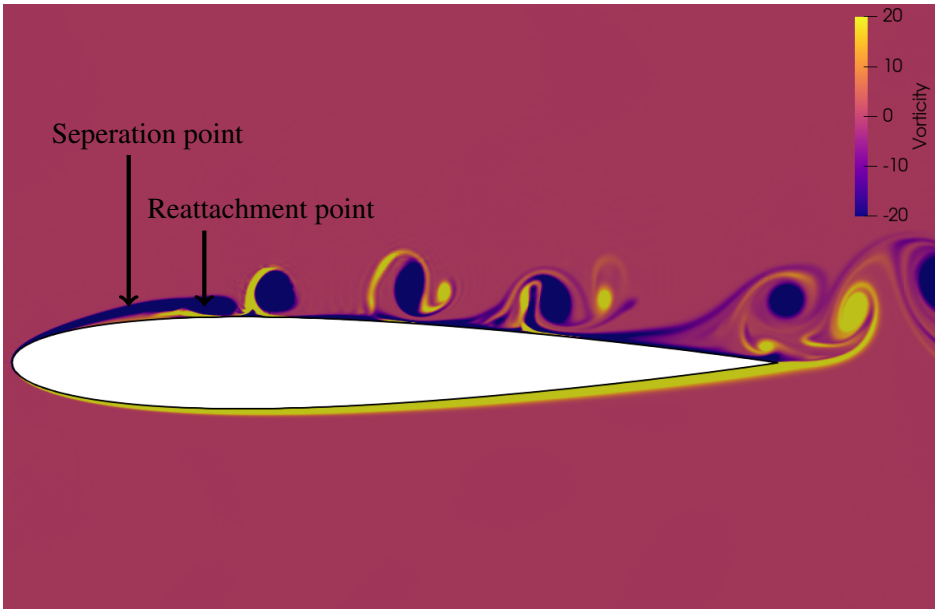

Figure 8.21. Vorticity contours of NACA0012 airfoil, $\alpha = 7.5°$

Lastly, the highly energetic turbulent eddies in the boundary layer collide with the suction surface of the airfoil, introducing a secondary method of acoustic generation, evident by the lack of clarity and cohesion of the acoustic field above the airfoil in Figure 8.22.

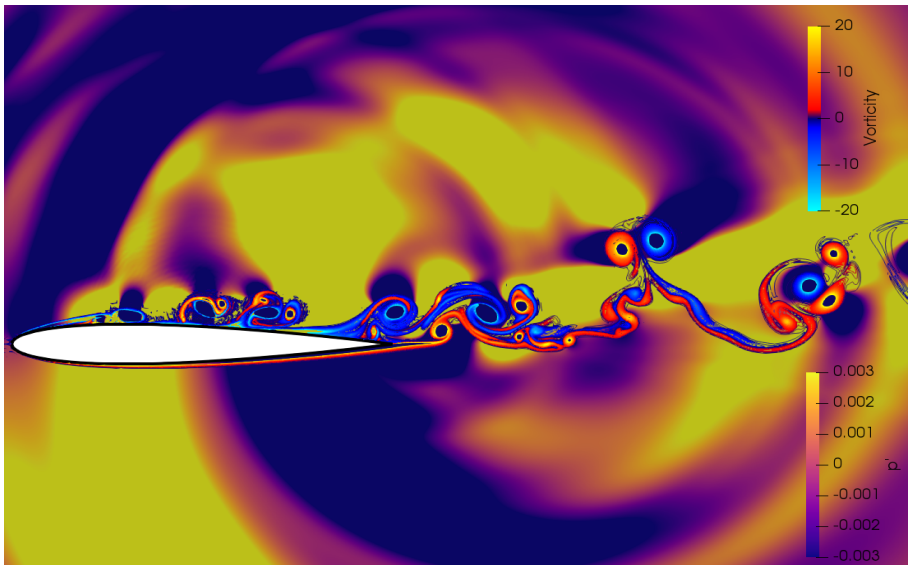

Figure 8.22. NACA0012 acoustic pressure and vorticity, $\alpha = 7.5°$

The instantaneous, time-averaged, and acoustic pressure fields are shown in Figure 8.23. The turbulent nature of the boundary layer, coupled with the additional acoustic waves generated along the suction surface of the airfoil, create a complex acoustic pressure field, as seen in Figure 8.23*c*, where acoustic waves can be seen emanating from both the trailing edge and the suction surface of the airfoil.

The acoustic waves produced via the collision of the turbulent boundary layer with the airfoil surface

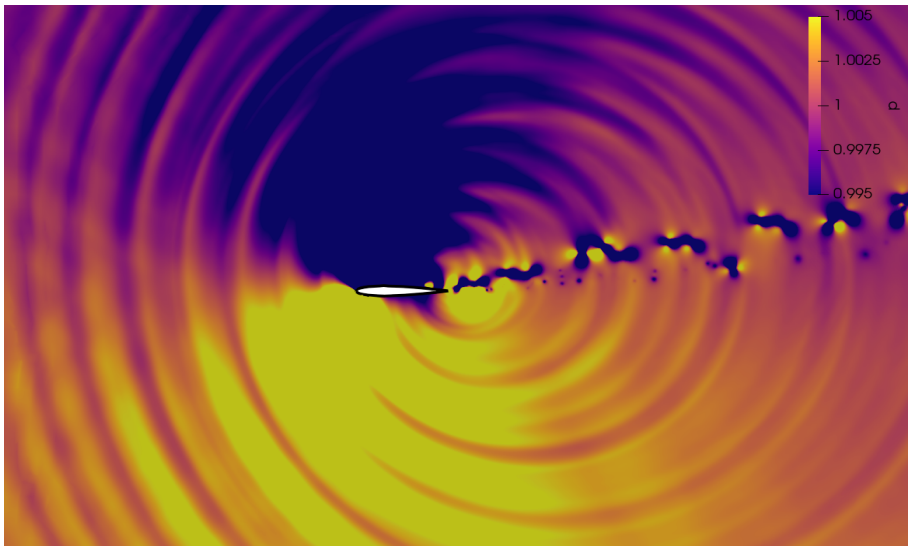

(a) Instantaneous pressure field

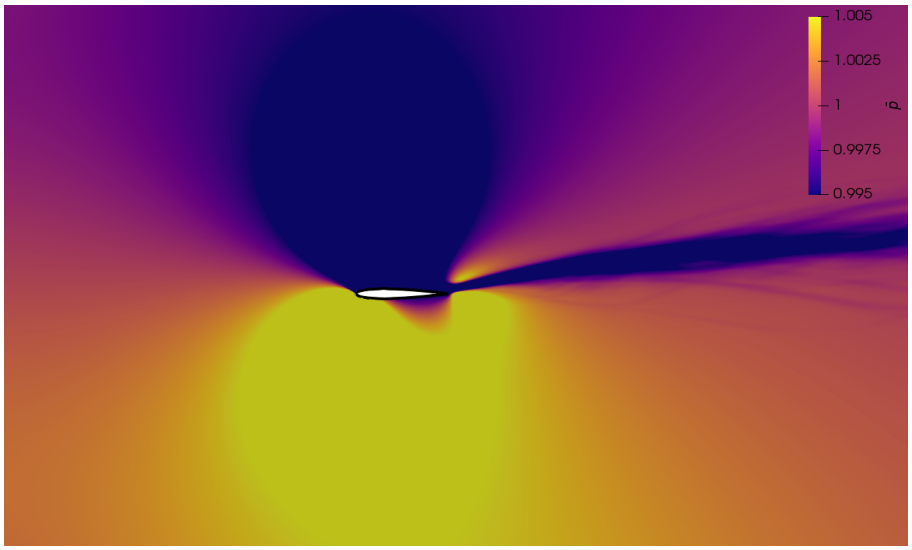

(b) time-averaged pressure field

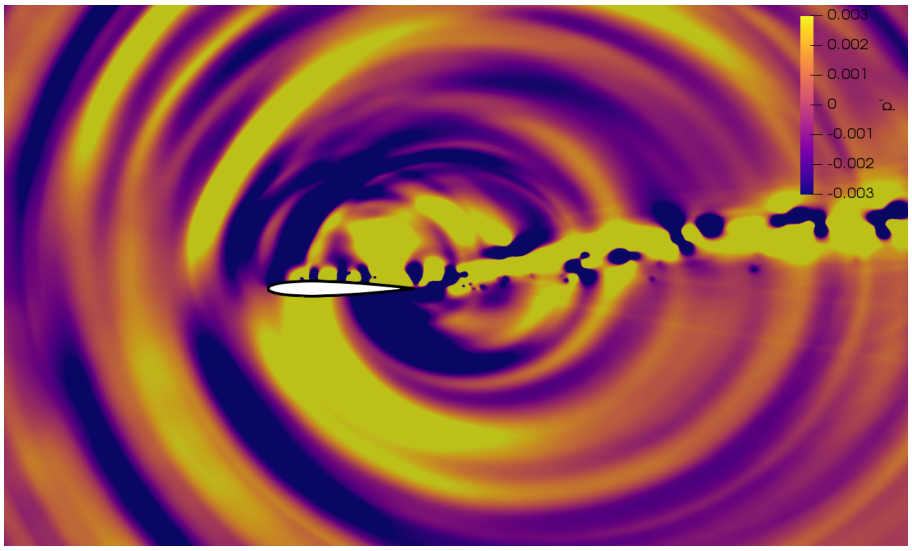

(c) Acoustic pressure field

Figure 8.23. NACA0012 instantaneous, time-averaged, and acoustic pressure fields, $\alpha = 7.5°$

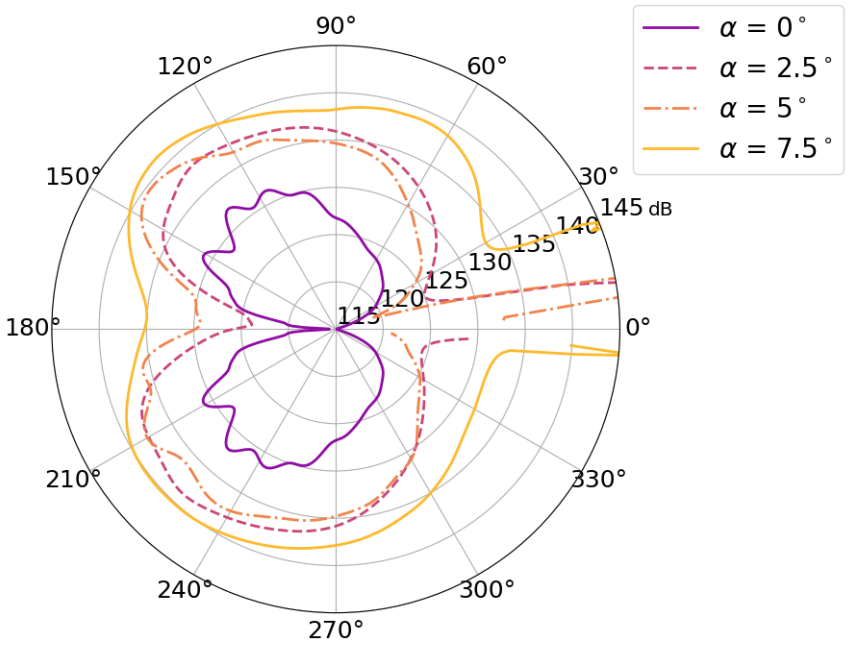

Figure 8.24. NACA0012 RMS acoustic pressure directivity recorded at R = 2, $\alpha = 7.5°$

drastically alter the directivity of the acoustic field, as seen in Figure 8.24, which contains the directivity and magnitude of the RMS acoustic pressure. The propagation of the turbulent boundary layer over the trailing edge produces significantly more noise than the previous simulations reported in this Chapter, with a maximum acoustic amplitude exceeding 140 dB. Similar to the $\alpha = 5°$ simulation, the directivity of the acoustic waves above the airfoil contains an upstream pointing lobe, albiet less pronounced. Dissimilar to the $\alpha = 5°$ simulation, however, is the presence of the large, downstream pointing lobe on the upper half of the directivity plot in Figure 8.24. The formation of this secondary lobe has been experimentally confirmed as a direct result of the turbulent boundary layer producing acoustic waves on the suction surface of the airfoil, with the magnitude and directivity of the lobe directly proportional to the turbulent intensity [70, 71]

The previous configuration of the NACA0012 airfoil at $\alpha = 5°$ did not produce any distinct tones; therefore, from the tonal envelope in Figure 8.1, increasing the angle of attack to 7.5° is expected to generate exclusively broadband noise. This is confirmed by Figure 8.25, which contains the PSD of the acoustic pressure, recorded at points D and E. From the enlarged portion of Figure 8.25, no distinct spikes occur in the PSD plot, verifying that the noise generated from a NACA0012 airfoil at $\alpha = 7.5°$ is exclusively broadband in nature.

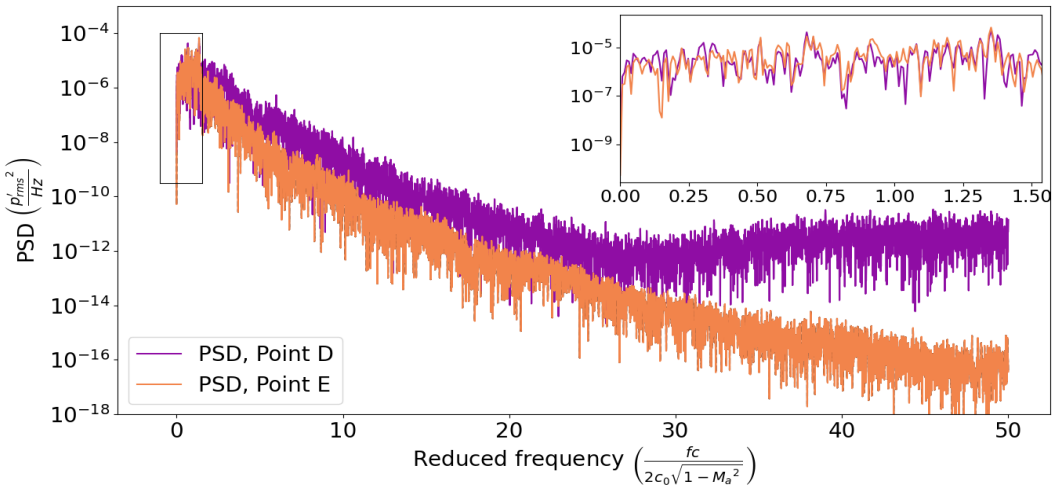

Figure 8.25. PSD of acoustic pressure in the free stream, Points D and E, $\alpha = 7.5°$

8.2 3D NACA0012 Airfoil

The NACA0012 airfoil at a zero degree angle of attack produced the most prominent tonal noise. Therefore, to evaluate the effects of turbulence on the generation of tonal noises, in addition to further substantiating the efficacy of the FR method as a direct CAA method, the simulation of the NACA0012 airfoil at $\alpha = 0°$ was extended to 3D.

8.2.1 Computational Details

To enable comparison of the results presented in the previous section with those presented in the current section, the 3D simulation of the NACA0012 airfoil was conducted with the same flow parameters as the 2D simulations, namely, α, R_e, M_a and P_r values of 0°, 5×10^4, 0.4 and 0.71, respectively.

Similar to the 2D simulations, the 3D computational domain was radially extended $5c_h$ and the outflow boundary was extended to $20c_h$, to allow sufficient damping of the turbulent wake before exiting the domain. To minimize the total number of elements, a structured mesh consisting exclusively of hexahedral elements was used to discretize the domain, as seen in Figure 8.26. The domain, consisting of 257,020 elements, applied a periodic span of $0.2c_h$, with 10 elements in the span-wise direction, to achieve span-wise decorrelation [72]. To ensure adequate resolution of the small-scale disturbances in the boundary layer, a y^+ value of 0.8 was applied along the entire airfoil surface, evidenced by the enhanced grid resolution surrounding the airfoil in Figure 8.26.

To minimize computational costs while maintaining a highly accurate solution, in the immediate vicinity of the airfoil $\mathcal{P}_4$ elements were applied in lieu of $\mathcal{P}_5$ elements. Additionally, enhanced temporal

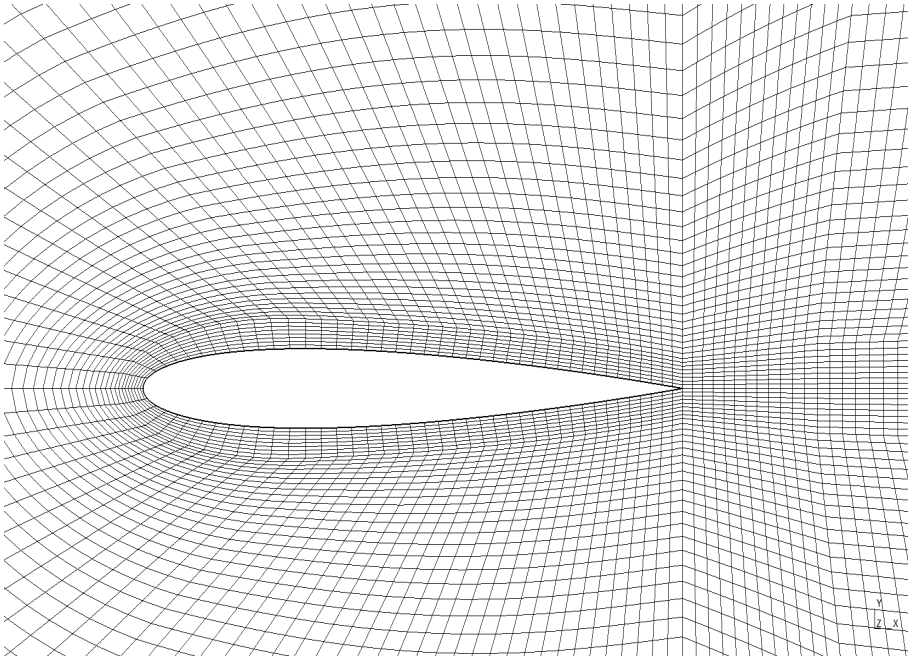

Figure 8.26. 3D NACA0012 computational mesh

resolution was achieved by applying the P-ERK time stepping scheme, with increased resolution in the boundary layer and near wake regions of the airfoil, as seen in Figure 8.27. The simulation was progressed for 75 convective time steps before recording data to ensure complete transition to turbulence. The simulation was then progressed for another 75 convective time steps in which the data was recorded.

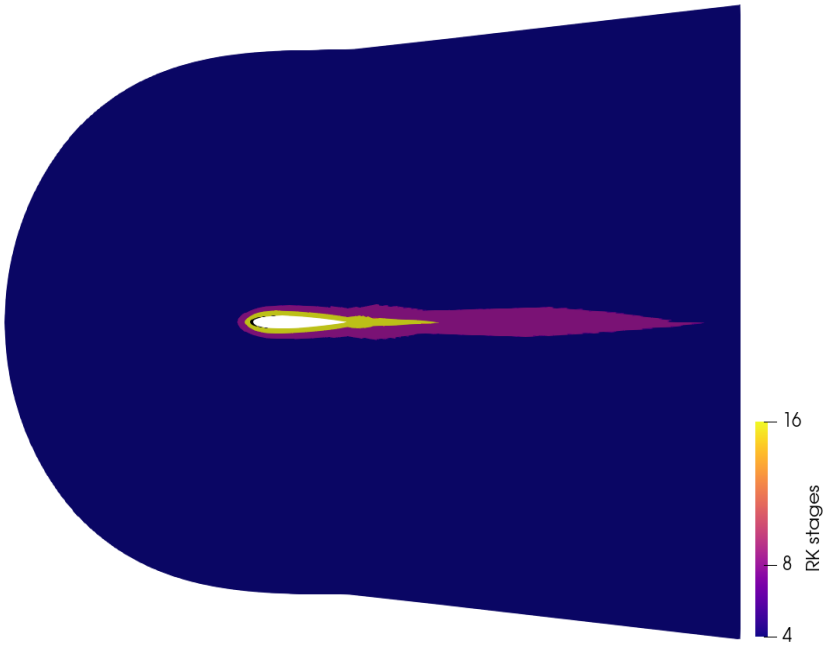

Figure 8.27. 3D NACA0012 P-ERK timelevels

As seen in Figure 8.28, the boundary treatments applied in the 3D simulation were similar to those applied in the 2D simulation. Artificial viscosity was applied in the downstream wake region of the

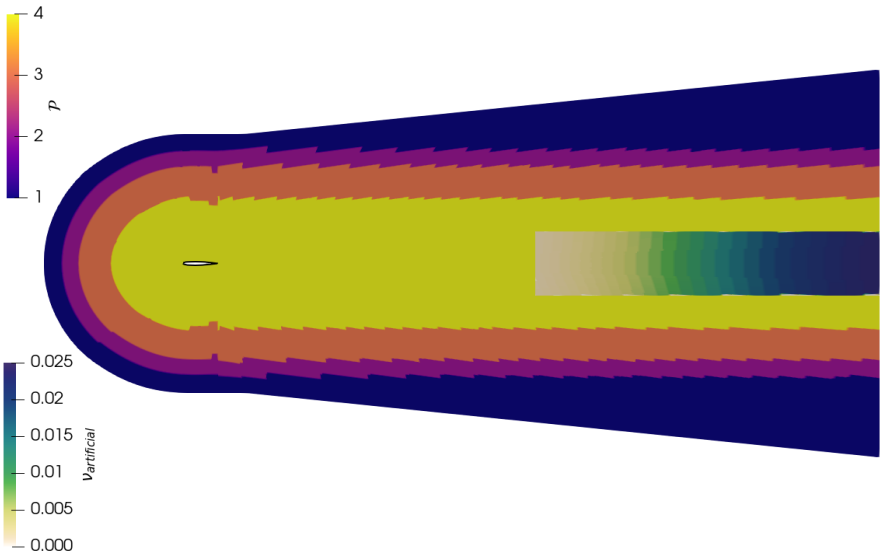

Figure 8.28. 3D NACA0012 boundary treatments

airfoil to prevent the turbulent vortices from encountering the outflow boundary. Additionally, polynomial adaptation was applied near the edges of the computational domain to dampen any outgoing acoustic waves while also reducing computational costs. As the outgoing turbulent vortices are more energetic than their 2D counterparts, a less aggressive stretching ratio of 1.0275 was applied near the computational outflow boundary to mitigate the generation of spurious reflections.

Lastly, the data sampling points are located at the same x and y coordinates as in the 2D simulation and lie at $0.1c_h$ in the spanwise direction.

8.2.2 Results

As witnessed in the 2D simulations, a zero degree angle of attack facilitates the laminar development of the boundary layer along the entire airfoil chord, on both the pressure and suction surfaces. As visualized by Figure 8.29, the laminar boundary layers periodically oscillate in the vicinity of the trailing edge, producing highly structured and coherent vortex streets. These vortex streets are rapidly dissipated and breakdown into a wholly turbulent wake.

Behaving similarly in 3D, the alternatingly shed vortex streets produce acoustic waves as they pass over the trailing edge, as seen in Figure 8.30, which contains both vorticity and acoustic pressure contours. As seen in the 2D simulations, the acoustic waves emanate from the trailing edge and propagate radially in all directions. As previously stated, free flowing turbulence is a highly inefficient acoustic source, with the acoustic intensity scaling proportional to $M_a{}^8$. The ineptitude of turbulence as an acoustic source is perfectly captured by Figure 8.30, as the micro fluctuations behind the airfoil depict the acoustic waves

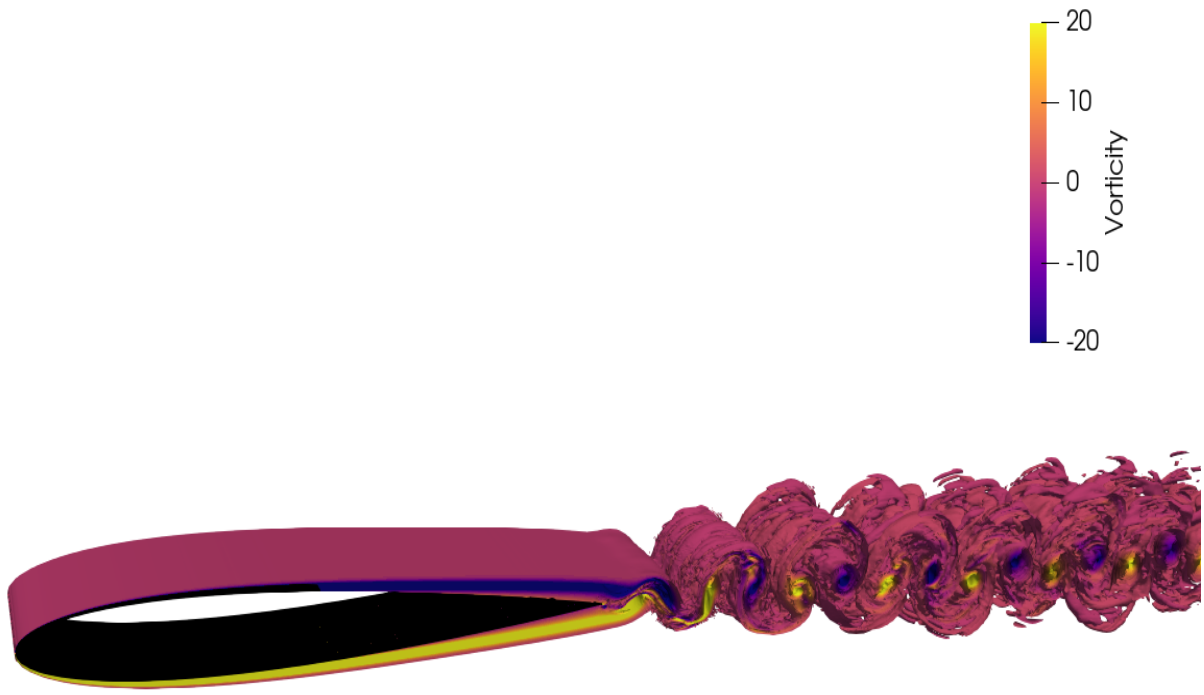

Figure 8.29. Vorticity contours of 3D NACA0012 airfoil, $\alpha = 0°$

generated by the chaotic fluctuations of the turbulent structures. Clearly, the acoustic waves produced by the turbulent wake are orders of magnitude smaller than those produced at the trailing edge, both in magnitude and wavelength.

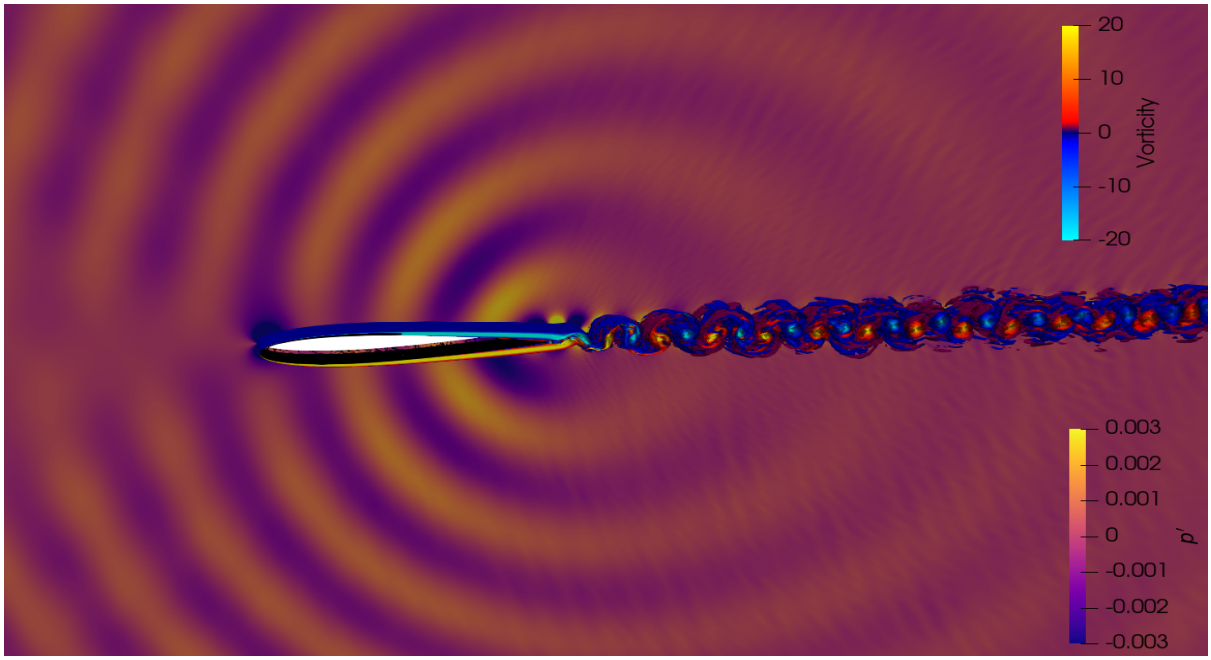

Figure 8.30. 3D NACA0012 airfoil acoustic pressure and vorticity contours, $\alpha = \deg 0$

The decomposition of the instantaneous pressure field into its subsequent time-averaged and acoustic components is presented in Figure 8.31. The pressure fields obtained from the 3D simulations are remarkably similar to those obtained from the 2D simulation, with the derivation of the acoustic pressure field easily visualized. The influence of the turbulent wake on the acoustic pressure field is again identified in Figure 8.31*c* by the presence of the extremely small scale fluctuations downstream of the airfoil.

The directivity of the acoustic pressure, recorded along a circle of radius 2 centered at the trailing edge, is presented in Figure 8.32, with the directivity of the equivalent 2D simulation included for reference. The directivity pattern obtained from the 3D simulation is exceedingly similar in shape to that obtained from the 2D simulation, suggesting the acoustic field is well resolved. The distinct lobes seen in the 2D directivity contour are also present, at the exact same angles, in the 3D directivity contour, albeit greatly exaggerated. Furthermore, the amplitude of the 3D directivity contour is significantly larger than the 2D directivity amplitude. The increased SPL of the 3D simulation is directly attributable to the uniform vortex streets convecting over the trailing edge, which contain considerably more energy than vortices contained in a 2D plane, thus resulting in increased acoustic amplitudes.

The PSD of the acoustic pressure, recorded at points D and E, is displayed in Figure 8.33. The existence of the individual spike in PSD, clustered around a narrow band of frequencies, reiterates the findings of the 2D simulation and confirms that the NACA0012 airfoil, at $\alpha = 0°$, produces tonal noises. The impact of the energetic vortex streets is again noticed, as the maximum amplitude of the fundamental harmonic is slightly larger than reported in 2D. Contrary to the flow over a deep cavity validation case, where the tonal frequency was lowered by the inclusion of a turbulent boundary layer, the tone in Figure 8.33 occurs at the exact same frequency as the fundamental harmonic in the 2D simulation, as the boundary layer remains laminar along the entirety of the airfoil. The influence of the turbulent wake on the acoustic field is additionally visualized in Figure 8.33, where the exclusively broadband nature of turbulence eliminates the presence of higher harmonics and widens the tonal spike.

8.3 Discussion

The 2D simulation results are first discussed, followed by a comparison and discussion of the 3D simulation results. An analysis of the tonal frequency selection mechanisms is then presented. The Chapter is then concluded by an assessment of the applied boundary treatments.

The elevated accuracy of the high-order FR method provided tremendous insight towards a multitude of physical phenomena associated with the acoustic generation and propagation processes. First, the

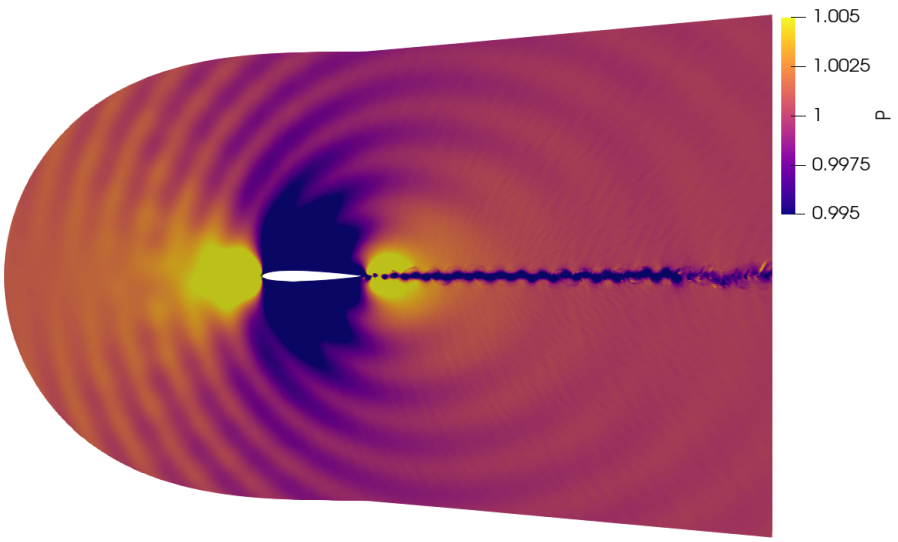

(a) Instantaneous pressure field

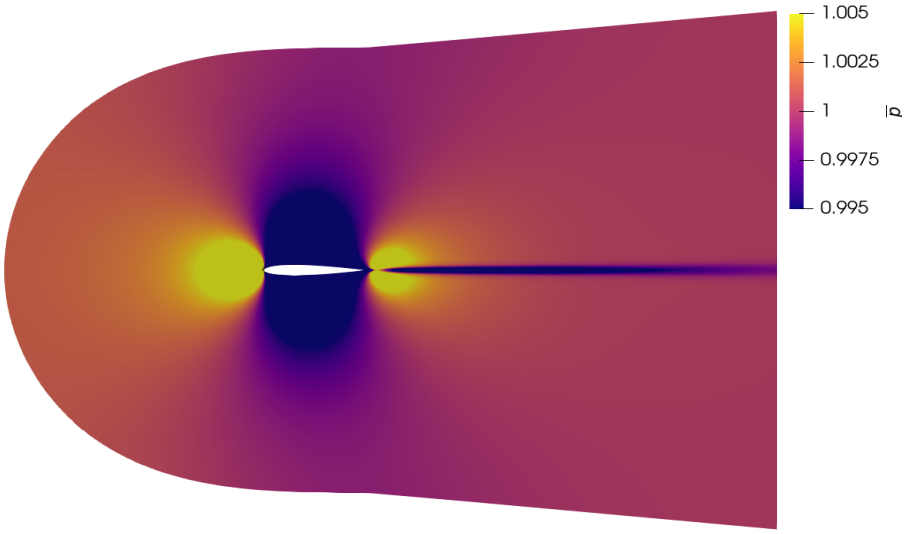

(b) time-averaged pressure field

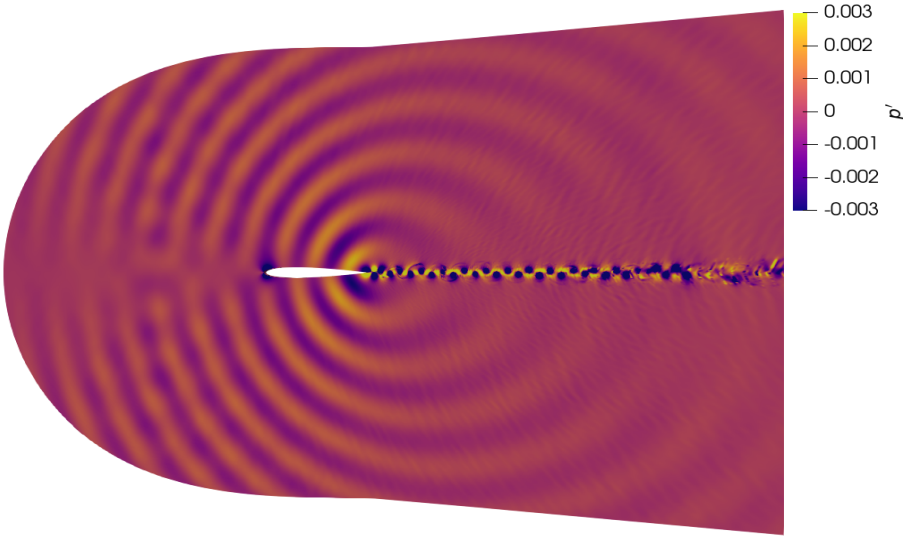

(c) Acoustic pressure field

Figure 8.31. 3D NACA0012 instantaneous, time-averaged, and acoustic pressure fields, $\alpha = 0°$

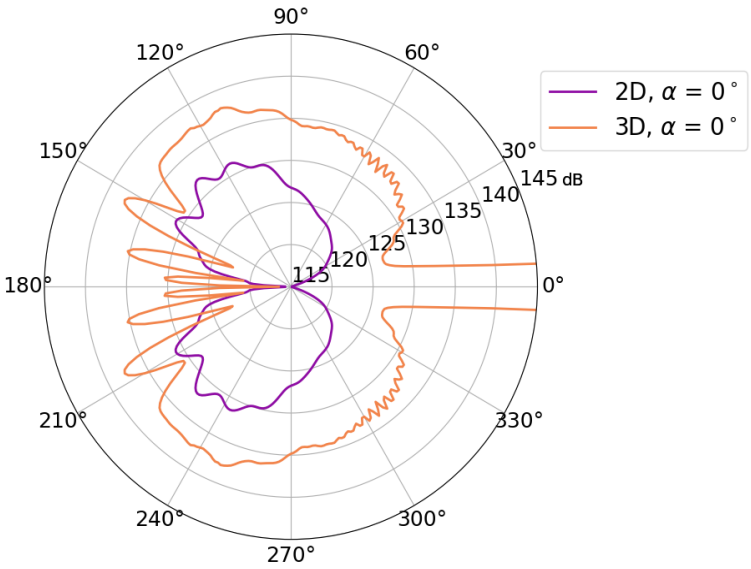

Figure 8.32. 3D NACA0012 RMS acoustic pressure directivity recorded at R = 2, $\alpha = 0°$

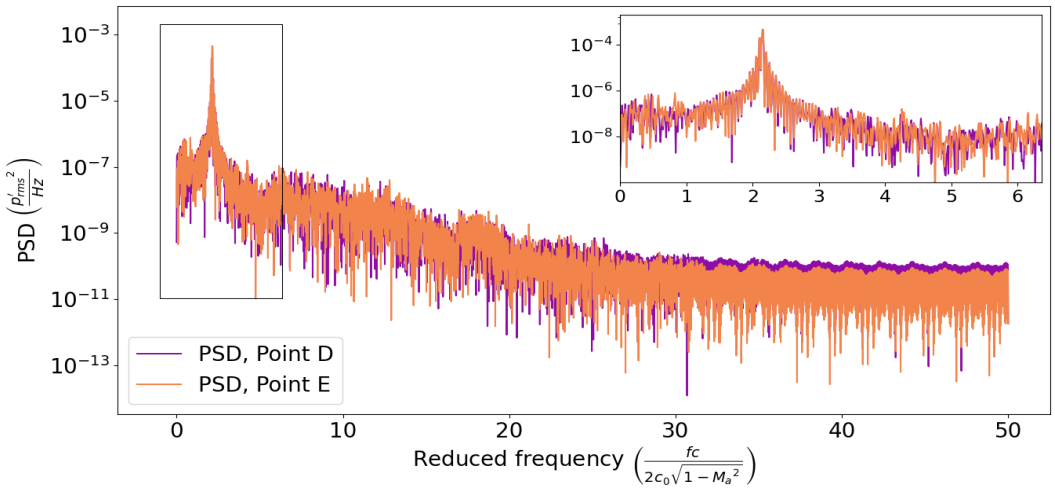

Figure 8.33. 3D PSD of acoustic pressure in free stream, Points D and E, $\alpha = 0°$

influence of the angle of attack on the resulting acoustic field is well captured. High lift configurations, experienced primarily during take-offs and landings, are known to produce higher SPLs than low lift configurations [3, 4, 5]. This correlation is perfectly documented in Figure 8.24, where the radiated SPL increases with increasing angles of attack. Although significantly louder, the acoustic field produced by high lift configurations is entirely broadband in nature [3, 4, 5], as evidenced by comparing the PSD plots of the $\alpha = 0°$ and $\alpha = 7.5°$ simulations, shown in Figures 8.10 and 8.25, respectively. Figure 8.10 contains distinct spikes in the PSD, indicating the presence of tonal noises, whereas Figure 8.25 does not consist of any definitive peaks, thus confirming the broadband nature of high lift configurations.

Secondly, as detailed in the previous sections, sharp trailing edges are efficient acoustic generators; however, they are not the exclusive means of acoustic generation. As the angle of attack increases, the pressure gradient on the suction surface of the airfoil intensifies, resulting in boundary layer separation and reattachment. The agitated reattachment of the boundary layer with the airfoil surface produces compact, highly fluctuating, small-scale acoustic waves [50, 71]. The presence of these diminutive acoustic waves is visualized by Figures 8.15, 8.20, and 8.25, where the PSD recorded above the airfoil (point D) becomes increasingly disparate from the PSD recorded below the airfoil (point E), especially at higher frequencies. At sufficiently large angles of attack, the reattachment of the boundary layer with the airfoil surface produces large-scale acoustic waves [50], as evidenced by the acoustic pressure field shown in Figure 8.23*c*. Additionally, as discussed in Chapter 1, sharp trailing edges produce a dipolar directivity field. Although inclined upstream and containing multiple distinct lobes, the directivity contour of the $\alpha = 0°$ simulation, shown in Figure 8.9, displays the 'figure-8' profile, characteristic of acoustic dipoles. The upstream inclination and inclusion of lobes in the directivity plot of Figure 8.9 is not a deficit of the FR method, but rather, a direct result of the diffraction of acoustic waves about the trailing edge [73]. Ikeda *et al.* demonstrate the angle of inclination of the directivity contour, as well as the magnitude and orientation of the lobes, are governed by a plethora of factors, most predominately the Reynolds number, angle of attack, and airfoil thickness. The results of the 2D NACA0012 airfoil simulations demonstrate the ability of the high order FR method to accurately capture many physical mechanisms responsible for the generation and propagation of acoustic waves from airfoils.

The simulation of an airfoil in 2D provides a relatively inexpensive means of approximating the acoustic propagation characteristics; however, the acoustic generation via flow over an airfoil is inherently a 3D process, and therefore must be simulated in 3D to obtain the exact acoustic generation and propagation characteristics. For instance, in 2D, the scattering effects of the leading edge are substantially mitigated and often neglected [50, 72, 74]. In 3D, the leading edge acts as a secondary scattering plane and severely alters the upstream acoustic directivity [73]. The impact of leading edge scattering effects on the acoustic directivity is evidenced in Figure 8.32, which contains several distinctive lobes, clustered around 180°, which are not present in the directivity contour of the 2D simulation. Additionally, the diffraction effects induced by the trailing edge are intensified in 3D [73], resulting in the amplified lobes in Figure 8.32. Furthermore, the influence of turbulence on the acoustic field can not properly be captured in 2D, as turbulence is fundamentally a 3D phenomenon. Despite the physical deficiencies of simulating an airfoil in 2D, the overall results of the 2D and 3D simulations are in excellent agreement. The 2D and 3D acoustic pressure fields, seen in Figures 8.8*c* and 8.31*c*, respectively, are in excellent agreement.

Moreover, the 2D and 3D simulations both recorded the generation of tonal noise, occurring at the exact same frequency. The exceptional similarity between the results of the 2D and 3D simulations of the NACA0012 airfoil emphasize the proficiency of high order numerical methods.

At a R_e of 50,000, the existence of tonal noises in the 2D and 3D $\alpha = 0°$ simulations is corroborated by the predicted tonal envelope, seen in Figure 8.1. Additionally, the predicted tonal envelope confirms the absence of tonal noises for the $\alpha = 5°$ and $\alpha = 7.5°$ simulations. The presence of a tonal noise at $\alpha = 2.5°$, however, is refuted by the predicted tonal envelope. Although the exact mechanisms responsible for the generation of distinct tonal noises from flow over isolated airfoils are still unknown [1, 63, 65, 66, 75], the existence of a laminar re-circulation bubble, in the vicinity of the trailing edge, on the pressure surface of the airfoil has been experimentally determined as a necessary condition for the production of tonal noises [1, 69, 74]. To substantiate the existence or absence of tonal noises, the velocity streamlines, contoured by the x-velocity magnitude, for each of the 2D simulations are presented in Figure 8.34, and the velocity streamlines for the 3D simulation, again contoured by the x-velocity magnitude, are presented in Figure 8.35. From Figure 8.34*a*, which shows the streamlines for the 2D $\alpha = 0°$ simulation, a laminar re-circulation bubble is readily identified on the pressure surface by the presence of the upstream pointing arrows. The streamlines of the $\alpha = 2.5°$ simulation, shown in Figure 8.34*b*, again illustrate the presence of a re-circulation bubble, albeit greatly reduced in size. The streamlines for the $\alpha = 5°$ and $\alpha = 7.5°$ simulations, shown in Figure 8.34*c* and 8.34*d*, respectively, do not include a re-circulation bubble. Similar to the 2D simulation, the 3D simulation at $\alpha = 0°$, shown in Figure 8.35, includes a laminar re-circulation bubble. The absence of a re-circulation bubble verifies the findings of the $\alpha = 5°$ and $\alpha = 7.5°$ simulations, in that no tonal noises are produced. The presence of the re-circulation bubble in the 2D and 3D $\alpha = 0°$ simulations confirm the presence of tonal noises. The presence of the small re-circulation bubble in the $\alpha = 2.5°$ simulation verifies that tonal noises could be produced. From Figure 8.15, it appears evident that tonal noises are in fact produced; however, additional physical verification is needed to determine if the tones are of sufficient strength to be audibly discernible.

Lastly, the performance of the applied boundary treatment methods must be addressed. Each individual boundary treatment method introduced in Chapter 6 is implemented in both the 2D and 3D simulations. As artificial viscosity is applied as a boundary treatment method, the solutions in the far-field are non-physical, and therefore are not pictured. However, the competence of the applied boundary treatments is assessed by the lack of spurious oscillations, particularly in the Figures depicting the acoustic pressure fields, such as Figure 8.8*c*. Again, the optimal values for the artificial viscosity and stretching ratios were determined iteratively in 2D, and then applied in 3D. To definitively resolve the

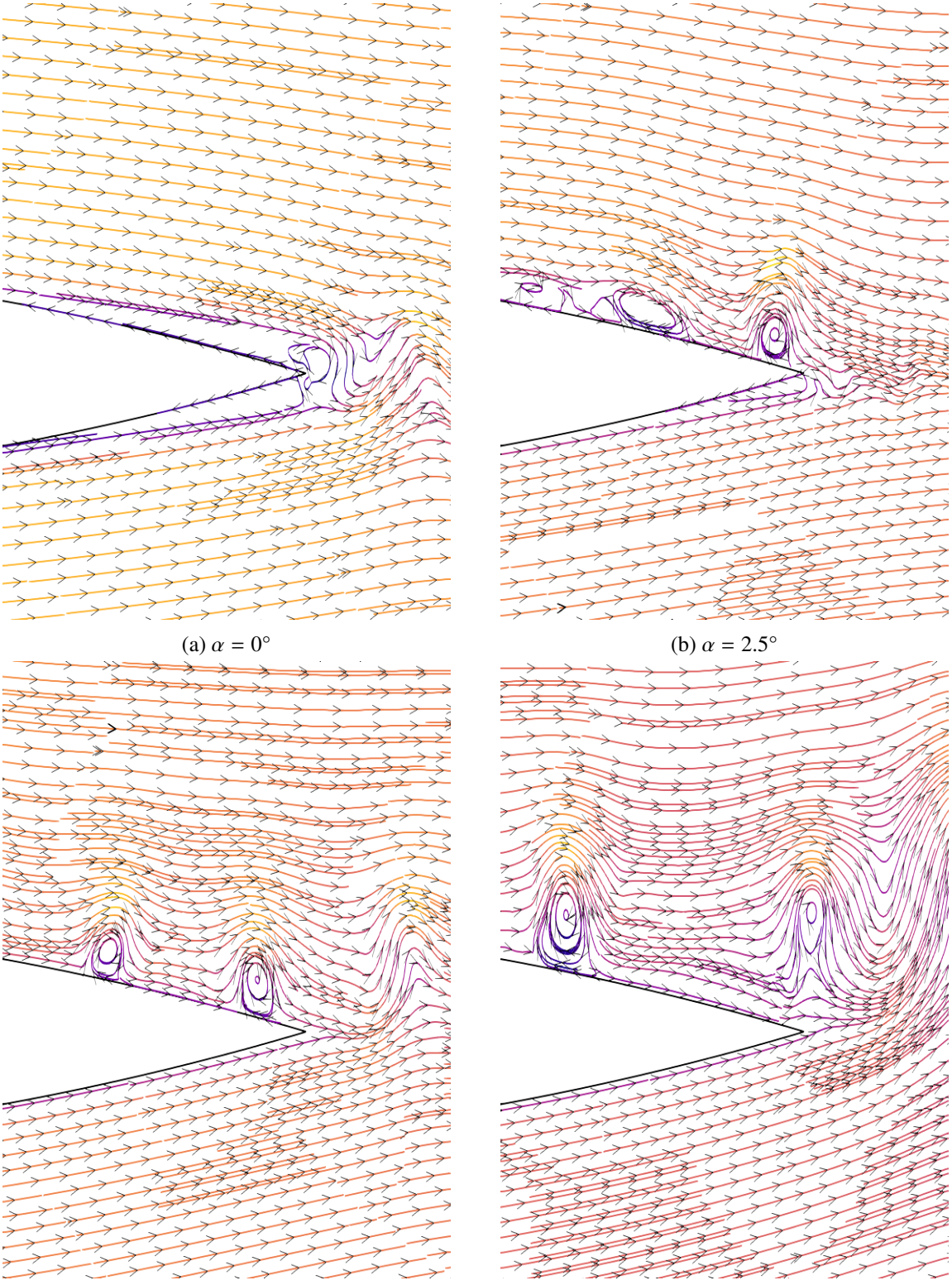

(a) $\alpha = 0°$ (b) $\alpha = 2.5°$

(c) $\alpha = 5°$ (d) $\alpha = 7.5°$

Figure 8.34. 2D NACA0012 velocity streamlines, colored by x-velocity magnitude

first conceptual challenge of CAA and demonstrate the ability of the FR method to efficiently operate on unstructured domains, the 2D grids were constructed with both structured, quadrilateral only regions and un-structured, mixed element regions, as seen in Figure 8.2. To reduce the computational costs, the 3D

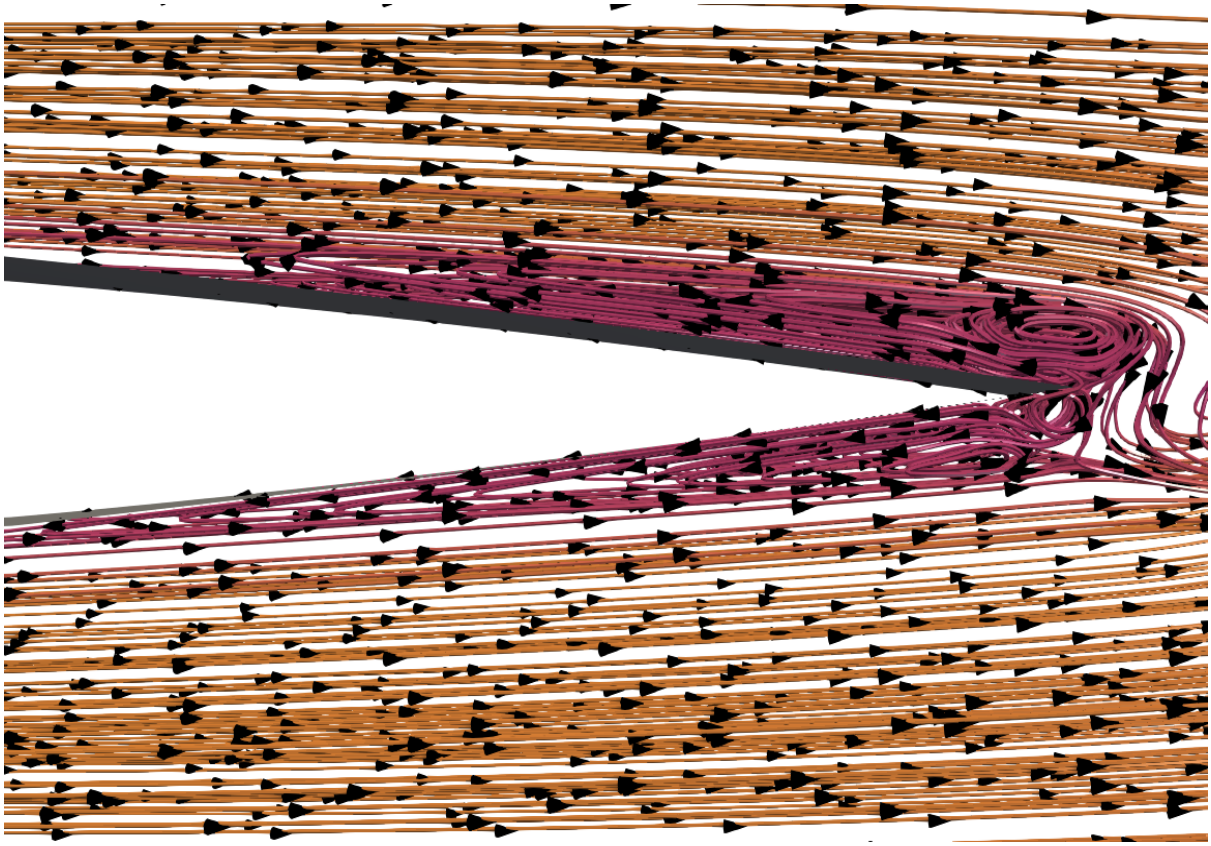

Figure 8.35. 3D NACA0012 velocity streamlines, colored by x-velocity magnitude

domain was constructed solely with hexahedral elements.

The results presented in this Chapter demonstrate the competence and proficiency of the high order FR method when applied to industrial-scale direct CAA applications. The elevated levels of accuracy afforded by the high order FR method provide invaluable insight into the physics governing the generation of tonal noises. Additionally, the highly efficient operation on modern hardware makes the FR method well suited for the necessary design optimization required to meet the noise reduction goals set forth by the ICAO.

The following Chapter summarizes the findings and conclusions of this thesis and includes recommendations for future work.

Chapter 9

Conclusions and Future Work

In this thesis, the proficiency and necessity of high order numerical methods in CAA are illustrated. Furthermore, the high order FR method's ability to be applied as a direct CAA approach is established.

The results presented in Chapter 6, particularly the grid convergence studies of the compact, high-frequency wave, demonstrate the unsuitability of low order polynomials for CAA, as the highly dissipative nature necessitates an impractically large number of DOF for accurate results. As the required number of DOF exponentially escalates with increasing simulation complexity and extensions to higher dimensions, the inability of low order polynomials to resolve the acoustic field, and their subsequent reliance on hybrid CAA methods, is recognized. Conversely, the high order polynomials provided enhanced accuracy on a per DOF basis and significantly reduced computational costs, thus establishing the aptitude of high order numerical methods for CAA. The results shown in Chapter 7 confirm the high order FR method is capable and well suited for direct CAA, as the near-field acoustics are in excellent agreement with the reference data. Furthermore, the boundary treatment methods proposed in Chapter 6, in conjunction with the Riemann invariant BCs, were validated for use in direct CAA. Lastly, the FR method's competence and proficiency to directly compute the near-field acoustics of challenging, real-world applications is demonstrated in Chapter 8. Although the exact mechanisms responsible for the generation of tonal noises from isolated airfoils are unknown [1, 63, 65, 66, 75], the presence of a laminar re-circulation bubble on the pressure surface of the airfoil has been proven as a necessary condition for the generation of tonal noises. At an angle of attack of zero degrees, the presence of a laminar re-circulation bubble was readily visualized in both 2D and 3D, with both the respective PSD plots indicating the presence of tonal noise. These findings are in agreement with Paterson's predicted tonal envelope for the NACA0012 airfoil [64]. At an angle of attack of 2.5 degrees, a laminar re-circulation bubble was again identified, and the presence of tonal noise was verified by the corresponding PSD plot. At angles of attack of 5 and 7.5 degrees, both

of which are outside of the predicted tonal envelope, a laminar re-circulation bubble was not captured, and accordingly, no tonal noises were produced.

The computational burden required to accurately resolve the small-scale acoustic waves, coupled with inefficient operation on modern hardware, has invalidated the use of direct CAA with traditional, low order numerical methods [16, 21, 22, 23, 25, 26, 51, 59]. However, as demonstrated throughout this thesis, the high order FR method sufficiently resolves these obstacles and facilitates the application of direct CAA.

As a concluding remark, several recommendations regarding obstacles encountered throughout this thesis, as well as potential future research topics, are provided. First, the applied boundary treatments are highly sensitive to the flow configuration and were iteratively tuned for each simulation. The development of a universal boundary treatment method or a perfectly NRBC, applicable towards both CFD and CAA applications, would reduce the time required to complete each simulation. Second, to further reduce computational intensity, the suitability of LES for direct CAA should be assessed by investigating the effects of the unresolved flow features on the acoustic generation process. Third, as the true objective of CAA is to evaluate the far-field acoustics, the performance and administration of a far-field reduced order model, such as the LEE or APE, which utilize the results of the applied direct CAA method, needs to be assessed. Fourth, to better approximate typical flight conditions, direct CAA simulations need to be conducted at higher Reynolds numbers. Fifth, the results of the CFD and CAA simulations should be corroborated by performing wind-tunnel simulations with identical flow configurations. Lastly, the high-order FR method, and the underlying CAA solver, have been thoroughly verified and validated as an accurate and efficient means of capturing near field acoustics, particularly in 2D; therefore, to best replicate the physical generation and propagation of sound, future work should focus primarily on 3D simulations, which capture the effects of turbulence on the generation and propagation mechanisms as well as the overall broadband noise spectrum.

References

[1] E.J.G. Arcondoulis, C.J. Doolan, A.C. Zander, and L.A. Brooks. A review of trailing edge noise generated by airfoils at low to moderate Reynolds number. *Acoustics Australia / Australian Acoustical Society*, 36:135–139, 03 2011.

[2] Centers for Disease Control and Prevention. What noises cause hearing loss? www.cdc.gov/nceh/hearing_loss/what_noises_cause_hearing_loss.html, 2019.

[3] International Civil Aviation Organization. *Independent Expert Integrated Technology Goal Assessment and Review for Engines and Aircraft*. ICAO, 2019. Doc No. 10127. Printed Montreal, QC.

[4] International Civil Aviation Organization. ICAO/Environmental Protection. https://www.icao.int/environmental-protection/pages/noise.aspx, 2019.

[5] Federal Aviation Administration. Fundamentals of Noise and Sound. https://www.faa.gov/regulations_policies/policy_guidance/noise/, 2020.

[6] International Air Transit Authority. Air passenger market analysis-December 2019. https://www.iata.org/en/iata-repository/publications/economic-reports/air-passenger-monthly---dec-2019/, 2019.

[7] A.L. Hansell, M. Blangiardo, L. Fortunato, S. Floud, K. de Hoogh, D. Fecht, R. E. Ghosh, H. E. Laszlo, C. Pearson, L. Beale, S. Beevers, J. Gulliver, N. Best, S. Richardson, and P. Elliot. Aircraft noise and cardiovascular disease near Heathrow airport in London: small area study. *British Medical Journal*, 347, 2013.

[8] D.A. Black, J.A. Black, T. Issarayangyun, and S.E. Samuels. Aircraft noise exposure and resident's stress and hypertension: A public health perspective for airport environmental management. *Journal of Air Transport Management*, 13(5):264–276, 2007.

[9] S. Bartels and U. Müller. The impact of acoustic and non-acoustic factors on short-term aircraft noise annoyance ratings –results of the COSMA field study at a major German airport. 01 2014.

[10] L. Jarup, W. Babisch, D. Houthuijs, G. Pershagen, K. Katsouyanni, E. Cadum, M. Dudley, P. Savigny, I. Seiffert, W. Swart, O. Breugelmans, G. Bluhm, J. Selander, A. Haralabidis, K. Dimakopoulou, P. Sourtzi, M. Velonakis, and F. Vigna-Taglianti. Hypertension and exposure to noise near airports: the HYENA study. *Journal of Environmental Health Perspectives*, 116(3), 2008.

[11] W. Babisch, G. Pershagen, J. Selander, D. Houthuijs, O. Breugelmans, E. Cadum, F. Vigna-Taglianti, K. Katsouyanni, A.S. Haralabidis, K. Dimakopoulou, P. Sourtzi, S. Floud, and A. L. Hansell. Noise annoyance — a modifier of the association between noise level and cardiovascular health? *Science of The Total Environment*, 452-453:50–57, 2013.

[12] T. Elliff, M. Cremaschi, and V.Huck. Impact of aircraft noise pollution on residents of large cities. Technical Report PE 650.787, European Parliament's Committee on Petitions, 2021.

[13] C.H. Hansen. Fundamentals of acoustics. https://www.who.int/occupational_health/publications/noise1.pdf, 2014.

[14] J. Slotnick, A. Khodadoust, J. Alonso, D. Darmofal, W. Gropp, E. Lurie, and D.Mavriplis. CFD Vision 2030 study: A path to revolutionary computational aerosciences. Technical Report NF1676L-18332, NASA and Boeing Research and Technology and Stanford University and Massachusetts Institute of Technology and National Center for Supercomputing Applications and Pratt and Whitney and University of Wyoming, 2014.

[15] Acoustics First. Acoustics first glossary of acoustic terms. http://www.acousticsfirst.com/glossary-of-sound-terms.html, 2021.

[16] T.K. Sengupta and Y.G. Bhumkar. *Computational Aerodynamics and Aeroacoustics*. Springer Nature Singapore Pte Ltd, 152 Beach Road, 21-01/04 Gateway East, Singapore 189721, Singapore, 2020.

[17] M.J. Lighthill. On sound genereated aerodynamically. 1. General theory. *The Royal Society of Mathematical, Physical, and Engineering Sciences*, 211:564–587, 1952.

[18] M.J. Lighthill. On sound genereated aerodynamically. 2. Turbulence as a sound source. *The Royal Society of Mathematical, Physical, and Engineering Sciences*, 222:1–32, 1954.

[19] N. Curle. The influence of solid boundaries upon aerodynamic sound. *The Royal Society of Mathematical, Physical, and Engineering Sciences*, 231:505–514, 1955.

[20] J.E. Ffowcs-Williams and L.H. Hall. Aerodynamic sound generation by turbulent flow in the vicinity of a scattering half plane. *Journal of Fluid Mechanics*, 40:657–670, 1970.

[21] C.K.W. Tam. Recent advances in computational aeroacoustics. *Journal of Fluid Dynamics Research*, pages 591–615, 2006.

[22] T. Colonius and S.K. Lele. Computational aeroacoustics: progress on non-linear problems of sound generation. *Journal of Progress in Aerospace Sciences*, 40:345–416, 2004.

[23] X.D. Li, M. Jiang, J. Gao, D. Lin, L. Liu, and X.Y. Li. Recent advances of computational aeroacoustics. *Journal of Applied Mathematics and Mechanics*, 36:131–140, 2015.

[24] J.C. Hardin and S.L. Lamkin. Aeroacoustic computation of cylinder wake flow. *AIAA Journal*, 22:51–57, 1984.

[25] E. Manoha, S. Redonnet, and S. Caro. *Computational Aeroacoustics*, chapter Environmental Impact, Manufacturing and Operations. John Wiley and Sons, 12 2010.

[26] J.C. Hardin and S.L. Lamkin. Computational aeroacoustics – present status and future promise. In *Aero- and Hydro- Acoustics*, pages 253–259, Berlin, Heidelberg, 1986. Springer Berlin Heidelberg.

[27] F.D. Witherden, A.M. Farrington, and P.E. Vincent. PyFR: An open source framework for solving advection-diffusion type problems on streaming architectures using the flux reconstruction approach. *Computer Physics Communications*, pages 3028–3040, 2014.

[28] S.B. Pope. *Turbulent Flows*. Cambridge University Press, 2000.

[29] C.D. Argyropoulos and N.C. Markatos. Recent advances on the numerical modelling of turbulence. *Journal of Applied Mathematical Modelling*, 39(2):693–732, 2015.

[30] A. Iida, K. Morita, and H. Tanida. Effects of turbulence on aerodynamic noise generation. *Forum Acusticum 2005 Budapest*, pages 953–958, 01 2006.

[31] P. Davidson. *Turbulence: An introduction for scientists and engineers*. Oxford University Press, 2015.

[32] M. Kamruzzaman, T. Lutz, W. Würz, and E. Krämer. On the length scales of turbulence for aeroacoustic applications. In *Proceedings of the 32nd AIAA Aeroacoustics Conference*, pages 1–25. AIAA, 2011.

[33] J.A. Ekaterinaris. High-order accurate, low numerical diffusion methods for aerodynamics. *Journal of Progress in Aerospace Sciences*, 41(3):192 – 300, 2005.

[34] B.C. Vermeire, F.D. Witherden, and P.E. Vincent. On the utility of GPU accelerated high-order methods for unsteady flow simulations: A comparison with industry-standard tools. *Journal of Computational Physics*, pages 497–521, 2017.

[35] P. Persson and J. Peraire. Sub-cell shock capturing for discontinuous galerkin methods. In *Proc. of the 44th AIAA Aerospace Sciences Meeting and Exhibit*, pages 1–13. AIAA, 2006.

[36] H.T. Huynh. A flux reconstruction approach to high-order schemes including discontinuous galerkin methods. *In 18th AIAA Computational Fluid Dynamics Conference*, page 4079, 2007.

[37] Z.J. Wang, Y. Liu, C. Lacor, and J.L.F. Azevedo. *Spectral Volume and Spectral Difference Methods*, volume 17, chapter 9, pages 199–226. Elsevier, 2016.

[38] K. Van den Abeele, K. Ghorbaniasl, G. Parsani, and M. Lacor. A stability analysis for the spectral volume method on tetrahedral grids. *Journal of Scientific Computing*, 227:257–265, 2009.

[39] B.C. Vermeire and P.E. Vincent. On the behaviour of fully-discrete flux reconstruction schemes. *Computer Methods in Applied Mechanics and Engineering*, pages 1053–1079, 2017.

[40] J.S. Hesthaven and T. Warburton. *Nodal Discontinuous Galerkin methods algorithms, analysis, and applications*. Springer, New York, NY, 2008.

[41] P.L. Roe. Characteristic-based schemes for the Euler equations. *Annual Review of Fluid Mechanics*, pages 337–365, 1986.

[42] F. Bassi, S. Rebay, G. Mariotti, S. Pedinotti, and M. Savini. A high order accurate discontinuous finite element method for inviscid and viscous turbomachinery flows. In *Turbomachinery, fluid dynamics, and thermo dynamics*, Lecture Notes in Computational Science and engineering (LNCSE), Volume 11, pages 99–108. Springer, 1997.

[43] F.D. Witherden and P.E. Vincent. An analysis of solution point coordinates for flux reconstruction schemes on triangular elements. *Journal of Scientific Computing*, pages 398–423, 2014.

[44] Z.J. Wang and H. Gao. A unifying lifting collocation penalty formulation including the discontinuous galerkin, spectral volume/difference methods for conservation laws on mixed grids. *Journal of Computational Physics*, pages 8161–8186, 2009.

[45] T. Haga, H. Gao, and Z.J.Wang. A high-order unifying discontinuous formulation for the Navier-Stokes equations on 3D mixed grids. *Journal of Mathematical Modelling of Natural Phenomena*, pages 28–56, 2011.

[46] J.C. Butcher. Coefficients for the study of Runge-Kutta integration processes. *Journal of the Australian Mathematical Society*, pages 185–201, 1963.

[47] B.C. Vermeire. Paired explicit runge-kutta schemes for stiff systems of equations. *Journal of Computational Physics*, pages 465–483, 2019.

[48] M.S. Howe. The generation of sound by aerodynamic sources in an inhomogeneous steady flow. *Journal of Fluid Mechanics*, 67(3):597–610, 1975.

[49] R.K. Amiet. Noise due to turbulent flow past a trailing edge. *Journal of Sound and Vibration*, 47:387–393, 1975.

[50] R.D. Sandberg, L.E. Jones, N.D. Sandham, and P.F. Joseph. Direct numerical simulations of tonal noise generated by laminar flows past airfoils. *Journal of Sound and Vibration*, 320:838–858, 2009.

[51] C.K.W. Tam. Computational aeroacoustic examples showing the failure of the acoustic analogy theory to identify the correct noise sources. *Journal of Computational Acoustics*, pages 387–405, 2002.

[52] M. Billson, L. Eriksson, and L. Davidson. Acoustic source terms for the linearized Euler equations in conservative form. *AIAA Journal*, 43:752–759, 2005.

[53] R.Ewert and W.Schröder. Acoustic perturbation equations based on flow decomposition via source filtering. *Journal of Computational Physics*, 188:365–398, 2003.

[54] C.A. Pereira. Analysis of high-order element types for implicit large eddy simulation. Master's thesis, Concordia University, Montreal, Quebec, Canada, July 2019.

[55] C.A. Pereira and B.C. Vermeire. Spectral properties of high-order element types for implicit large eddy simulation. *Journal of Scientific Computing*, 85:1–38, 2020.

[56] J. Gill, R. Fattah, and X. Zhang. Towards an effective non-reflective boundary condition for computational aeroacoustics. *Journal of Sound and Vibration*, 392:217–231, 2016.

[57] J. Carlson. Inflow/outflow boundary conditions with application to FUN3D. Technical Report NASA/TM–2011-217181, NASA, Langley Research Center, Hampton, Virginia, October 2011.

[58] A. Jameson. Numerical solution of the Euler equation for compressible inviscid flow. Technical report, Princeton University, Princeton, New Jersey, USA, 1983.

[59] M.D. Dahl. Third Computational Aeroacoustics(CAA) Workshop on Benchmark Problems. In *Proc. of the Third computational aeroacoustics conference*, NASA/CP=2000-209790, 2000.

[60] M.A. Ol'shanskii and V.M. Staroverov. On simulation of outflow boundary conditions in finite difference calculations for incompressible fluid. *International Journal for Numerical Methods in Fluids*, 33:499–534, 2000.

[61] O.Inoue and N.Hatakeyama. Sound generation by a two-dimensional circular cylinder in uniform flow. *Journal of Fluid Science*, 471:285–314, 2002.

[62] C.K.W Tam and P.J.W. Block. On the tones and pressure oscillations induced by flow over rectangular cavities. *Journal of Fluid Mechanics*, 89:373–399, 1978.

[63] C.K.W. Tam. Discrete tones of isolated airfoils. *Acoustical Society of America*, 55:1173–1177, 6 1974.

[64] R.W. Paterson, P.G. Vogt, and M.R. Fink. Vortex noise of isolated airfoils. *Journal of Aircraft*, 10:296–302, 05 1973.

[65] H. Arbey and J.Bataille. Noise generated by airfoil profiles places in uniform laminar flow. *Journal of Fluid Mechanics*, 134:33–47, 01 1983.

[66] E.C. Nash, M.V. Lowson, and A. McAlpine. Boundary-layer instability noise on aerofoils. *Journal of Fluid Mechanics*, 382:27–61, 03 1999.

[67] P.E. Vincent, F.D. Witherden, B.C Vermeire, J. Park, and A. Iyer. Towards green aviation with Python at petascale. In *Proc. of the International Conference for High Performance Computing, Networking, Storage and Analysis*, SC16, pages 1–11, 2016.

[68] F.D. Witherden and P.E. Vincent. On the identification of symmetric quadrature rules for finite element methods. *Journal of Computers and Mathematics with Applications*, pages 1232–1241, 2015.

[69] E.J. Arcondoulis, C.J. Doolan, and A.C. Zander. Airfoil noise measurements at various angles of attack and low Reynolds number. *Proceedings of ACOUSTICS 2009, 23–25 November 2009, Adelaide, Australia*, pages 1–8, 08 2009.

[70] L.E. Jones and R.D. Sandberg. Numerical analysis of tonal airfoil self-noise and acoustic feedback-loops. *Journal of Sound and Vibration*, 330:6137–6152, 2011.

[71] M. Jiang, X.D. Li, and D.K. Lin. Numerical simulation on the airfoil self-noise at low mach number flows. In *50th AIAA Aerospace Science Meeting including the New Horizons Forum and Aerospace Exposition*, AIAA 2012-0834, pages 1–19, 2012.

[72] M.E. Rosti, M Omidyeganeh, and A. Pinelli. Direct numerical simulation of the flow around an aerofoil in ramp-up motion. *Journal of Fluid Physics*, 28(2), 2016.

[73] T. Ikeda, T. Atobe, and S. Takagi. Direct simulations of trailing-edge noise generation from two-dimensional airfoils at low Reynolds numbers. *Journal of Sound and Vibration*, 331:556–574, 09 2012.

[74] G. Yakhina, M. Roger, S. Moreau, L. Nguyen, and V. Golubev. Experimental and analytical investigation of the tonal-edge noise radiated by low Reynolds number aerofoils. *Journal of Acoustics*, 2:293–329, 2020.

[75] B. Plogmann, A. Herrig, and W. Würz. Experimental investigations of a trailing edge noise feedback mechanism on a NACA 0012 airfoil. *Jounral of Experiments in Fluids*, 54, 05 2013.